Analysis of crack geometry and location by means of a multi-probe Potential Drop technique

University of Padua

Department of Industrial Engineering

Master Course in Mechanical Engineering

Academic year 2022/2023

26th October 2023

Supervisor:

Prof. Alberto Campagnolo

Co-Supervisor:

PD Dr. rer. nat. habil. Jürgen Bär

Prof. Giovanni Meneghetti

Ing. Luca Vecchiato

Author:

Alessandro Codemo

Acknowledgment

I would like to express my deep appreciation to Professor Alberto Campagnolo, my supervisor at University of Padua, for his unwavering guidance and support throughout my academic journey. Thanks to him, I was able to explore and expand my knowledge in the field of mechanical engineering and develop a solid foundation in fracture mechanics. This thesis would not have been possible without his help.

Furthermore, I would like to extend my gratitude to Professor Jürgen Bär from the Universität der Bundeswehr München, who kindly agreed to collaborate on the project and generously allowed me to utilize his machine laboratory. His invaluable guidance throughout the implementation of my thesis was greatly appreciated.

Finally, I would like to thank Prof. Giovanni Meneghetti and Ing. Luca Vecchiato, from University of Padua, for their support and commitment in the implementation of this project. Their contributions in providing creative and innovative solutions were crucial in the process of making this thesis.

Last but not least, my family, without whom none of this would be possible and to whom I owe everything.

Contents

List of Figures

List of Tables

Chapter 1

Introduction

In the field of fracture mechanics, the accurate assessment of the cracks size in mechanical and structural components is of primary importance. Achieving optimal design and ensuring superior and safer mechanical performance depends on this precise evaluation.

Consequently, engineers and academic researchers are increasingly turning their attention to this critical domain. Their collective aim is to develop innovative, real-time methods for monitoring crack growth and for on-site, non-destructive determination of crack geometry and location.
Yet, despite enormous efforts has been done, this remains a hard challenge. The limitations in our current capabilities significantly affect the accuracy of measurements and predictions, often necessitating a substantial safety factor to account for uncertainties, as emphasized by Hyde [30].

The field of non-destructive testing (NDT) offers several techniques, each with unique applications, advantages, and disadvantages. The present research regards the potential drop (PD) approach, renowned for its reliability in estimating crack initiation and propagation.

The PD method entails two primary variants: Direct Current Potential Drop (DCPD) and Alternating Current Potential Drop (ACPD). Both methodologies consist in the transmission of electrical current through a conductive material which generates an electric field. Notably, this electric field is perturbed when the material presents discontinuities, such

as propagating cracks. The PD methods facilitate the detection of voltage drops across the sections of the conductor. These drops are used to extract valuable information about these features, often through the employement of calibration curves or mathematical formulations.
The main objective of this thesis is to employ the DCPD method for accurately estimating the size and geometry of propagating cracks within structural components. This endeavor will draw upon both theoretical approaches and finite element analysis (FEA).

Figure 1.1: Example of Fatigue Failure on roller coaster. North Carolina, 30/06/23, Corriere.it

This work firmly resides within the broader domain of Structural Health Monitoring (SHM) [16]. The core ambition of SHM is to provide continuous, real-time insight into the health of constituent materials within structures. This is crucially important to manufacturers, end-users, and maintenance teams, as it allows a comprehensive understanding of the integrity of in-service structures.
Furthermore, SHM plays a pivotal role in averting catastrophic failures and enhancing structural safety. Remarkably, the DCPD method emerges as a promising avenue for achieving the objectives of SHM. Its affordability and simplicity of operation make it an ideal candidate for this purpose.
In other words, this thesis aims to employ the DCPD method to precisely assess crack dynamics within structural components.

1.1 NDT methods applied to crack initiation and crack propagation

In this section, a brief review of several NDT methods are presented as alternatives of PD methods. These methods includes optical observation, ultrasonic methods (involving ultrasonic and acoustic emission), magnetic or current methods [30].

1.1.1 Visual Inspection

Figure 1.2: Visual Inspection. Image taken from : [5]

Visual testing (VT) is one of the foundational and earliest non-destructive testing (NDT) methods. It primarily relies on the mere capability of the human eye to discern surface flaws. In its simplest form, visual testing is performed without the need for any additional equipment, although the use of aids (e.g. a magnifying glass) can enhance its effectiveness, (e.g. [9]).

This method offers several notable advantages, including its straightforwardness, versatility across various stages of construction and industry, cost-effectiveness, and absence of requirement for specialized apparatus. These attributes make it an accessible and valuable tool in many inspection scenarios.

However, it's essential to acknowledge the inherent limitations of visual testing. It primarily addresses macro-level surface discontinuities, which means that it may not detect flaws that are beneath the surface or on a micro-scale. Therefore, while it excels at identifying readily apparent surface defects, it is less effective at uncovering deeper or more subtle issues. Understanding these constraints is vital for making informed decisions about the application of visual testing within quality control and inspection procedures.

1.1.2 Dye penetrant inspection

Dye penetrant testing is a non-destructive testing (NDT) method that leverages the detection of a fluid's accumulation around surface discontinuities to reveal visible indications of surface flaws, [24]. While seemingly straightforward, this method conceals certain inherent complexities, such as the prerequisite for meticulous surface preparation prior to inspection and its limited applicability to porous materials. This complexity is critical to understand and address in order to ensure the effectiveness and reliability of the testing process.

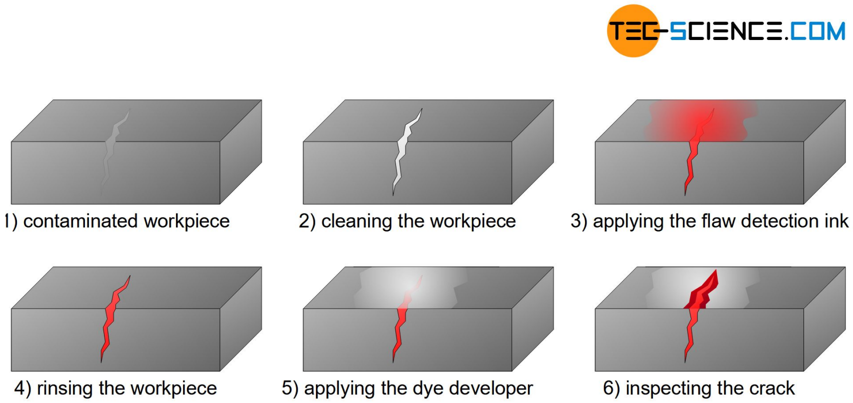

Figure 1.3: Dye Penetrant Inspection. Image retrieved from [1]

1.1.3 Ultrasonic testing

In the ultrasonic testing, a transducer is strategically placed on the test piece with the goal of emitting an ultrasonic wave. During this operation, some of the signal encounters obstructions within the material and subsequently bounces back. A specialized receiver captures this reflected portion of the wave, subjecting it to intricate analysis for the identification of defects, [30].

The merits of this method are several such ad the capability for volumetric inspection, the adeptness to discern surface and subsurface anomalies, and the inherent suitability for automation. These attributes render ultrasonic testing a valuable technique for various industrial applications.

However, it is imperative to acknowledge the limitations of this testing methodology. Firstly, it necessitates a highly skilled operator, primarily due to the difficulty involved in interpreting the obtained data. Moreover, for contact-based testing, the utilization of a couplant substance is mandatory, and the test object's surface must exhibit a relatively smooth texture, [9]. These challenges underline the importance of meticulous execution and thorough consideration of operational conditions when employing ultrasonic testing.

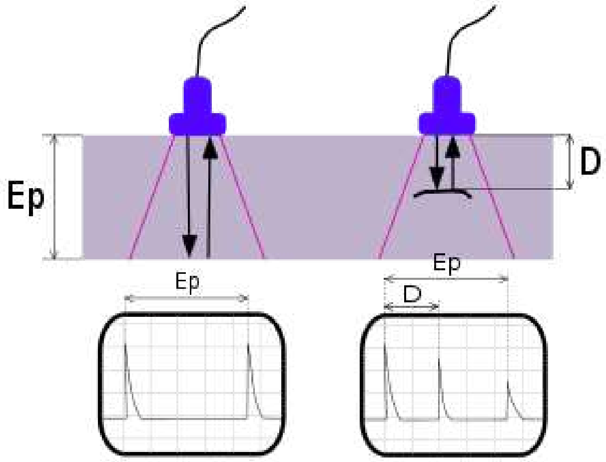

Figure 1.4: Ultrasonic Testing: Image taken from [4]

1.1.4 Eddy Current

In Eddy current testing (ET), the core principle involves the strategic placement of a coil through which an alternating current flow, positioned in proximity to or surrounding the test specimen. This electrically charged coil gives rise to circulating eddy currents within the material, engendering mutual induction in the specimen's vicinity, particularly near the surface, [9]. These circulating eddy currents play a fundamental role as they interact with and influence the electrical properties of the specimen. Any deviations in these electrical characteristics, induced by the presence of flaws or defects, serve as key indicator for detection.

Since the Eddy current testing is a widely employed and effective method, it excels at surface defect detection. Nonetheless, it exhibits certain limitations that warrant consideration. Firstly, its applicability is confined to conductive materials, making it unsuitable for non-conductive substances. Additionally, it is not well-suited for the detection of long crack lengths. Furthermore, Eddy current techniques are notably ineffective when applied to ferrous metals due to their dependence on magnetic permeability, [30]. These constraints emphasize the need for a comprehensive understanding of the material's properties and the specific inspection requirements when employing this method.

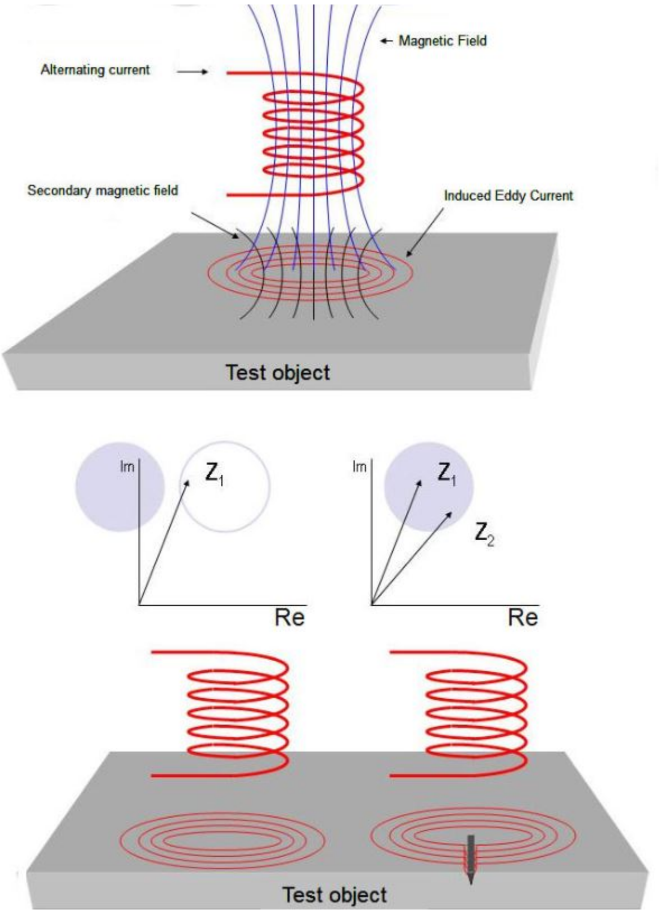

Figure 1.5: Eddy Current Testing. Image taken from [3]

1.1.5 Magnetic particle testing

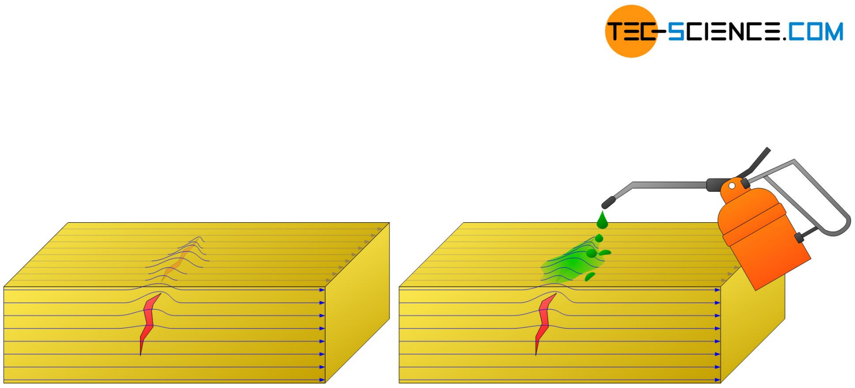

Figure 1.6: Image taken from [2]

The detection of surface and shallow subsurface discontinuities or defects in ferromagnetic materials is achieved through the utilization of a magnetic field, a technique known as magnetic particle testing (MT). This method relies on the principles of magnetism to identify imperfections in materials, especially in steel bars. When a discontinuity or flaw is present within the steel bar positioned across the ends of a magnet, a flux leakage field emerges at the surface of the flaw. This occurs because the magnetic field departs from the ferromagnetic material and travels through the surrounding air.

To render this magnetic flux leakage visible and easily detectable, iron particles are applied to the steel bar. These iron particles are naturally drawn towards and held in place by the flux leakage emanating from the flaw. This phenomenon provides a clear visual indication, allowing inspectors to readily identify the presence and location of the flaw, as described in the reference [9]. Magnetic particle testing is an effective and widely used non-destructive testing method for detecting surface and near-surface defects in ferromagnetic materials, playing a crucial role in quality assurance and safety inspection processes.

Chapter 2

PDM: Literature Review

In this chapter, the research background supporting the thesis is introduced. Firstly, the definition and application of DCPD are reported, focusing on all the different configurations e.g. single probe and multi probe and how the calibration curve can be obtained. Secondly both theoretical and numerical methods employed to treat the data are explained.

2.1 PDM: Potential Drop Method

The Potential Drop Method, in particular the Direct Current PDM was first applied to detect surface cracks by Trost in 1944 [7] but the concept had been originally introduced several years earlier by B. M. Thornton and W. M. Thornton in 1938 [28, 30].

It is now a well-established practice in fatigue crack growth testing where DCPD is used to monitor crack initiation and crack growth as a function of time in conductive materials. [27].
The physical principle of this technique is based on Ohm's law and the corresponding evolution of the specimen resistance. During these tests, a constant input current is applied to the test specimen through a steady current source. Simultaneously, a voltmeter is connected to the monitored region to continuously measure the potential value during the fatigue test. In the case of a cracked specimen, the reduction in cross-sectional area due to crack propagation affects the electric field generated by the current, leading to a

change in the potential value recorded by the voltmeter.

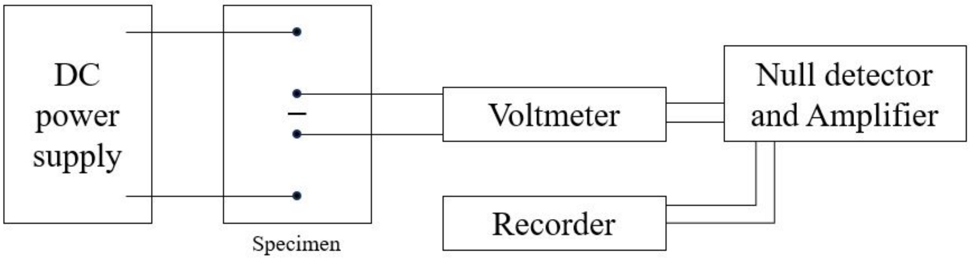

Figure 2.1: DCPD setup

An example of the application of DCPD in notched specimens was carried out by Campagnolo et al. in 2019 [10]. In these experiments, notched steel specimens are subjected to fatigue tests while a constant current flows through them. A voltmeter is then connected via two copper cables welded to the surface of the test specimen at an imposed distance, to measure the potential drop during the fatigue test. A sketch of the set-up of the experiment is shown in the figure 2.2.

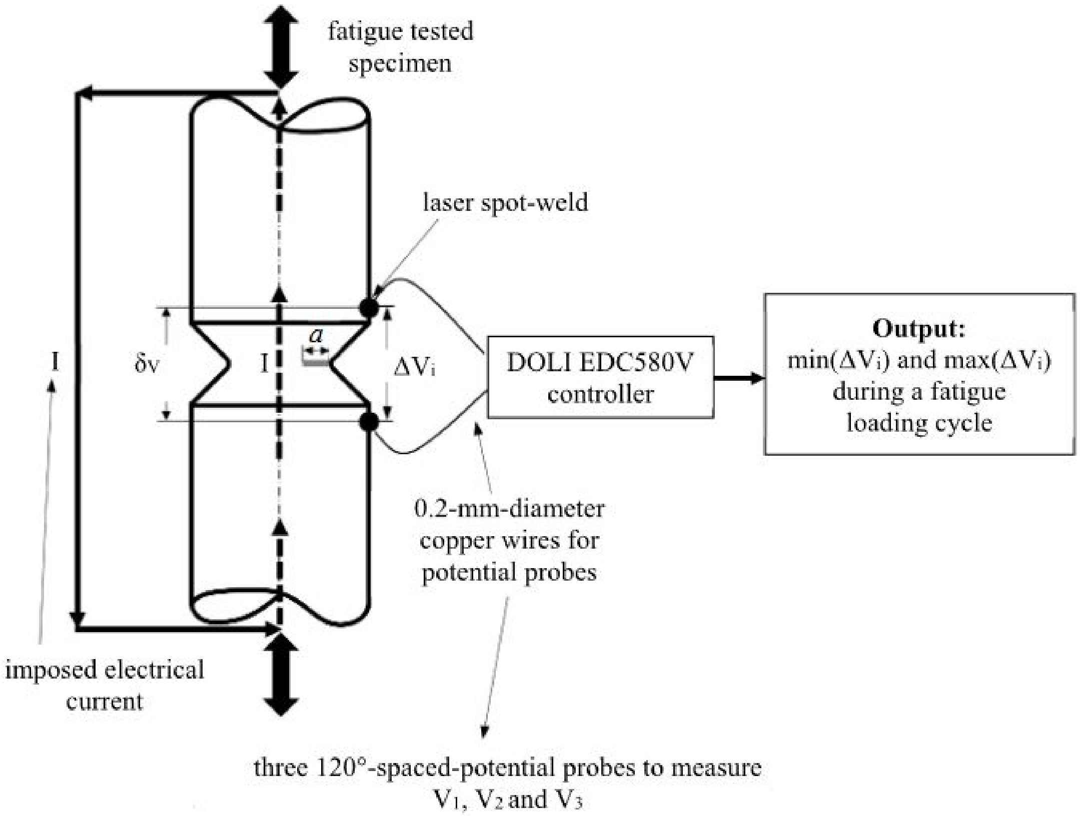

Figure 2.2: Campagnolo et al. experimental set-up [10]

2.1.1 Advantages and Disadvantages of PDM

As emphasized in several research papers, (see [30]), Potential Drop Methods (PD) offer numerous advantages that have led to their widespread application. Notably, the cost-effectiveness of the required instrumentation and the simplicity of operation make PD methods highly appealing. Moreover, the capability to make accurate predictions further enhances their desirability.

One of the main advantages of PD methods is their independence from visual access. This characteristic enables them to monitor conditions concealed from optical methods, expanding their utility. PD methods exhibit versatility and adaptability for testing under diverse and challenging conditions, including corrosive environments, high-pressure settings, regions with elevated radiation levels, and those subject to fluctuating and high temperatures, as noted in the reference by Hyde [30].

However, it is important to acknowledge certain limitations inherent to PD methods, as reported in the literature. Proper electrode placement is of extremely important to achieve accurate measurements. To ensure high resolution, the electrodes must be positioned in close proximity to the crack, a principle underscored in [12]. The study in this reference illustrates the significant impact of probe positioning distance on method sensitivity. Ideally, the distance between the potential grips should be minimized to maximize resolution. However, this reduction in distance can result in decreased potential readings, with the instrument's noise becoming a dominant factor, thus limiting measurement accuracy. Consequently, determining the optimal distance for potential grips represents a delicate balance between these two opposing effects.

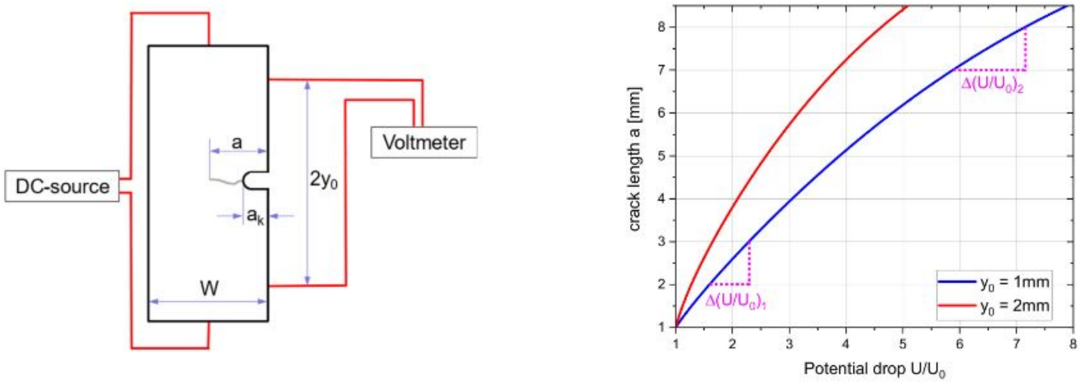

Figure 2.3: Jürgen Bär experimental set-up [12]

Additionally, the PDM method is strongly influenced by temperature variations. It is known that the resistivity of the material increases with temperature according to the law 2.1, where ρ is the resistivity, T is the temperature, ρ_0 is the resistivity of the metal at the reference temperature T_0 (usually $T_0 = 20C$) and α is the material-dependent temperature coefficient.

$$\rho = \rho_0 \left[1 + \alpha \left(T - T_0\right)\right] \tag{2.1}$$

Consequently, PD methods necessitate calibration for each unique test piece, and their applicability is confined to conductive materials. Understanding both the advantages and limitations of PD methods is crucial for their effective and accurate implementation in various testing scenarios.

2.2 Calibration of the PDM

Several experimental, analytical, and numerical methods have been adopted in the literature to derive the calibration curves of the potential drop method (PDM), i.e. the potential drop change versus the crack depth a [8].

2.2.1 Experimental calibration

Simple calibration curves for complicated specimen geometries under any combination of conditions, such as thermo-mechanical fatigue (TMF), are available through the use of experimental data. Small crack lengths are almost always difficult to accurately measure using empirical solutions, and measurements are susceptible to errors that are probably brought on by variations in the positions of the current leads and potential probes [30]. As exemplified in the paper of Jürgen Bär [12], calibration can be accomplished by simulating crack propagation through precise saw cuts, followed by establishing a correlation between the measured potential data and the "artificial" crack lengths generated in this manner.

An alternative approach involves marking the crack extension on the fracture surface using overloads (Fig. 2.4) or load cycle blocks with varying stress ratios, often referred to as "marker loads." The introduction of overload causes a change in the micro-structure of the fracture surface, altering its appearance and making the shape of the crack visible with each application of load. Thanks to this 'zebra-stripe' pattern, it is then possible to link the potential value with the actual crack size in post-processing.

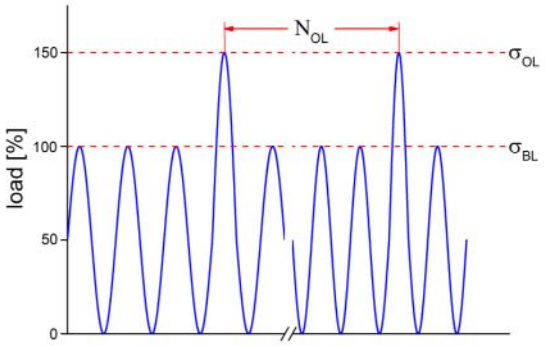

Figure 2.4: Fatigue test with overload

Employing saw cuts offers the advantage of having the "crack front" align almost perpendicular to the direction of crack propagation. In this case, measuring the "crack length" on the specimen's surface suffices. In contrast, when dealing with fatigue cracks, the crack length tends to be underestimated due to the curvature of the crack front.

For calibrating the Direct Current Potential Drop Method (DCPDM), both the marking of crack length through overloads and marker loads have proven effective. To address the curvature of the crack front, a suitable technique involves measuring the crack area. The mean crack length is subsequently determined by dividing the measured crack area by the width of the specimen [12].

2.2.2 Analytical calibration

For a specific specimen geometry and PDM operating conditions, the calibration curves can also be derived analytically by solving the Laplace equation [8].

One of the commonly employed analytical calibration techniques for center-cracked specimens is Johnson's formula, as referenced in [19]. In this approach, the potential is measured both along the center line and across the crack, with the assumption of a uniform current distribution, as discussed in [30]. Johnson introduced a calibration equation tailored for slit-type center cracks within finite-width plates. This equation is defined as the ratio of the Potential Drop (PD) corresponding to half of the slit length, a, V; and half of the initial length a_0, V_0. This relationship can be expressed as follows:

$$\frac{V}{V_0} = \frac{\cosh^{-1}\left(\frac{\cosh\frac{\pi y}{W}}{\cos\frac{\pi a}{W}}\right)}{\cosh^{-1}\left(\frac{\cosh\frac{\pi y}{W}}{\cos\frac{\pi a_0}{W}}\right)} \tag{2.2}$$

Where W is the specimen width.

For SEN specimen, it is possible to evaluate the crack length from eq. 2.2:

$$a = \frac{2W}{\pi} \cdot \arccos\left\{\frac{\cosh\left(\frac{\pi \cdot y_0}{2 \cdot W}\right)}{\cosh\left[\frac{U}{U_0} \cdot \text{arcosh}\left(\frac{\cos\left(\frac{\pi y_0}{2W}\right)}{\cos\left(\frac{\pi a_0}{2W}\right)}\right)\right]}\right\} \tag{2.3}$$

In order to have a best fitting, this equation 2.3 can be adapted with a least square fit by using the distance of the potential grips y_0 as a free parameter [12].

2.2.3 Numerical calibration

Numerical techniques play a pivotal role in achieving precise control over various critical parameters within Potential Drop Methods (PDM). These parameters include not only the dimensions of cracks and specimens but also the positioning of probes for current injection and the acquisition of potential measurements. Numerical approaches offer the advantage of meticulously fine-tuning these parameters, enabling a deep understanding of their interplay.

One notable application of numerical techniques is the optimization of probe configurations, a process that can be carried out independently to fine-tune the performance of PDM. Moreover, numerical approaches provide the means to estimate the influence of specimen and crack geometry, as well as plastic deformation, on the calibration process. This computational prowess allows for the construction of multiple calibration curves tailored to specimens with varying aspect ratios, as highlighted in the reference by Hyde [30].

The calibration curves, as elucidated in [18], were meticulously developed through the application of advanced 3D electrical Finite Element (FE) analyses. These numerical analyses were conducted using specialized 10 node tetrahedral electric solid elements, specifically the SOLID232 elements sourced from the Ansys element library.

During these numerical investigations, a global element size of 1.5 mm was employed to represent the structural model. However, in regions close to the surface, where numerical results were extracted for accurate potential drop readings, a finer element size of approximately 0.7 mm was utilized. Furthermore, a mesh refinement strategy was implemented, leading to a localized element size of about 0.3 mm in proximity to the crack plane. This finer mesh facilitated the precise capturing of variations in potential and enabled a deeper understanding of PDM sensitivity in relation to crack size.

Subsequent to the resolution of all FE models, the numerical results underwent comprehensive post-processing. This post-processing stage was instrumental in computing the derivative of the potential drop, often referred to as DCPD sensitivity, concerning variations in crack size, as reported in [18]. These sensitivities serve as invaluable insights for calibration and, ultimately, the accurate detection of crack dimensions within structural components using PDM.

2.3 Multi-probe PDM setup

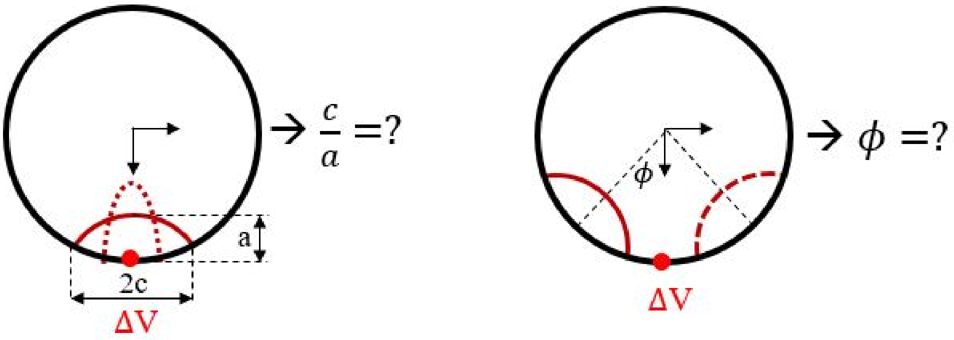

Figure 2.5: PDM single Probe set-up. Evaluation of ϕ and $\frac{c}{a}$

Single probe PDM is an effective method for fatigue crack size estimation. However, it cannot provide any information regarding the shape or position of a crack. A valuable solution to this problem has been proposed in various literature researches; indeed, the use of multiple probes appears to be a significant improvement to simple PDM.

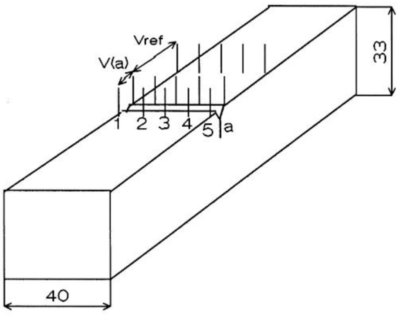

Figure 2.6: Triples of electrodes in five rows to monitor crack profile. Image taken from [13]

When dealing with CT-specimens, it's possible to employ a the multi probe set-up like the one shown in Fig. 2.6. Then, through the Johnson's formula, calculate the crack lengths for each probes using the corresponding potentials value.

As shown in Fig. 2.7, there is a strong retardation of crack growth in the central area, which could not be found out by optical measurement or standard DCPD measurement using one pair of electrodes (or a single row of electrodes) [13]. Indeed, it has been experimentally proven that the shape and position of a crack have a great influence on the measured potential [20]. Thanks to this knowledge, the development of a multi-probe PDM measurement system for the detection and localization of cracks in fatigue experiments has become possible for various specimen geometries. [23]. In these studies, it is shown how the use of multiple probes in round bar specimens, which exhibit fatigue cracks with semi-elliptical shape, can provide indications of both the crack initiation point and crack shape.

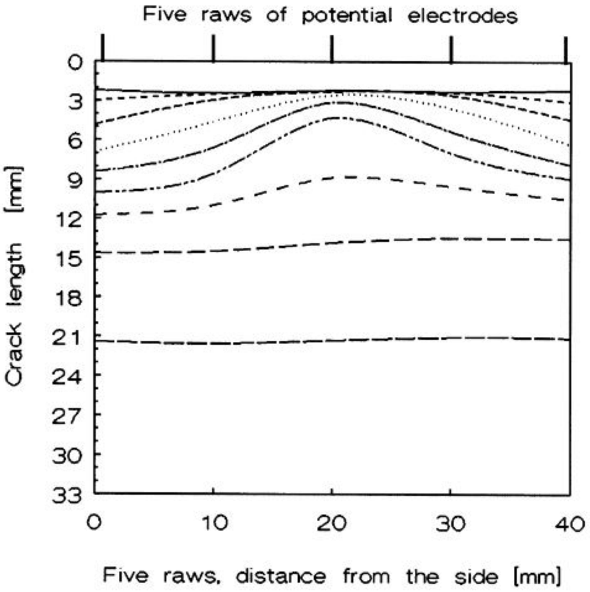

Figure 2.7: Lengths computed from DCPD measurement at five surface points. Image taken from [13]

The techniques employed in this research for assessing the relationship between potential values, crack depth, and location are presented below.

2.3.1 Determination of fatigue cracks shape and position

This method was introduced by Jürgen Bär in 2019 [23] and it was specifically tailored for notched round specimens. The investigations are focused on the determination of the crack location and the early detection of small fatigue cracks employing a specific multi probe Direct Current PDM. When subjected to fatigue tests, these specimens typically display a crack with a semi-elliptical shape. The crack can initiate at any point in the net cross-section of the specimen and gradually grows in size until it eventually leads to failure.

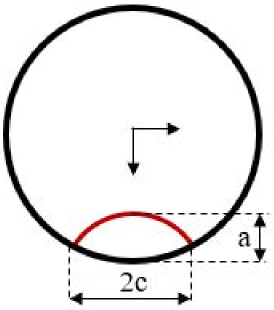

Figure 2.8: Semi-elliptical crack shape

Instead of positioning a single potential probe at the point of crack initiation, the method proposes using three potential probes spaced 120° apart around the circumference (Fig. 2.9).

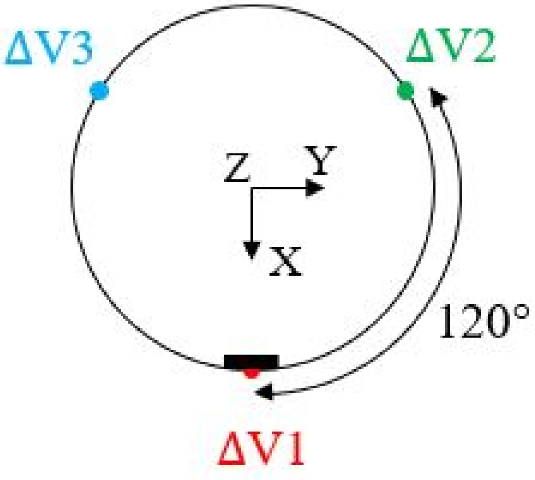

Figure 2.9: Multi Probe PDM set-up

With this specific arrangement of potential probes, acquiring data about the crack depth and initiation point becomes more accessible. A simple vectors method, developed by Jürgen Bär and Moritz Hartweg [23], is presented here as a means to achieve this.

Before proceeding with the presentation of the vectors method, it is essential to discuss the procedure for connecting the different potential probes to the surface of the specimen. Each individual probe consists of a pair of copper wires, each with a diameter measuring 0.2 mm. These wires are carefully and precisely welded onto the surface of the specimen at predetermined locations. Following this, the cables are connected to the potential drop reading system, allowing for continuous recording of variations throughout the duration of a fatigue test.

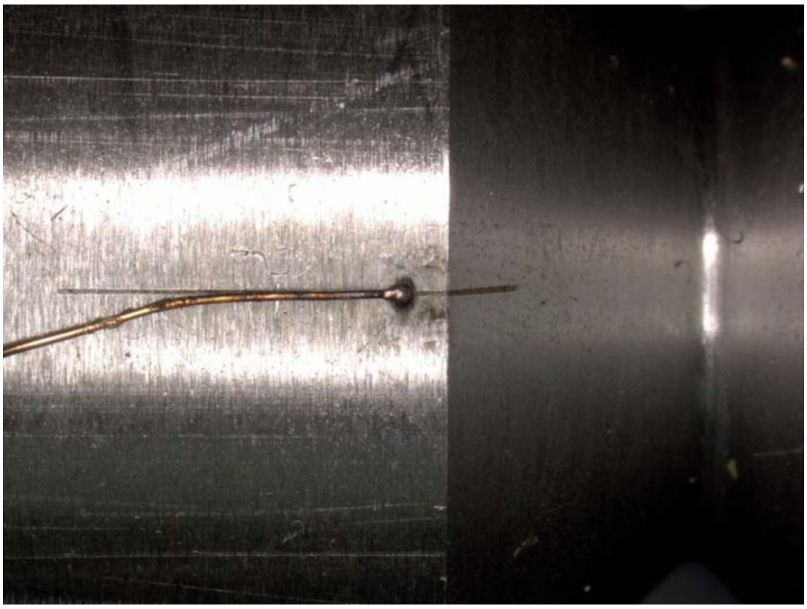

Figure 2.10: Connection of the copper wire to the specimen surface

The advantages of directly welding the wires onto the specimen surface, as opposed to using press-fitted pins, are elucidated in [21]. This approach effectively eliminates all the ”starting effects” triggered by deformations in the holes and subsequent alterations in the conductivity of press-fitted pins. Consequently, the noise in the potential signal is significantly reduced. As a result, the potential drop exhibits a steady increase, allowing for the reliable calculation of crack length right from the outset of the fatigue experiment. This capability facilitates the detection of early crack propagation, even when the potential drop undergoes a change of less than 1%.

Vectors model

The first step is to evaluate the Relative Potential P_i' from the actual potential value ΔV_i and the potential of the specimen without cracks, denoted as $\Delta V_{i,0}$:

$$P_i' = \frac{\Delta V_i}{\Delta V_{i,0}} \tag{2.4}$$

The relative potentials P_1', P_2' and P_3' are treated as vectors in cylindrical coordinate.

$$\vec{P}_1 = \begin{pmatrix} r \\ 0^\circ \\ P_1' \end{pmatrix} \vec{P}_2 = \begin{pmatrix} r \\ 120^\circ \\ P_2' \end{pmatrix} \vec{P}_3 = \begin{pmatrix} r \\ 240^\circ \\ P_3' \end{pmatrix} \tag{2.5}$$

Without any started crack, at the beginning of the experiment, all the three relative potentials have the same value $P_i = 1$ resulting in the same length for their vectors. As a consequence, the vectors span a horizontal plane, with the plane's normal vector $\vec{N}$ parallel to the loading direction (Fig. 2.11).

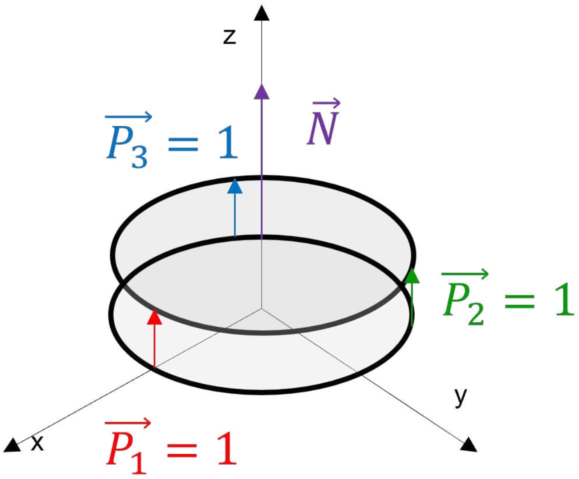

Figure 2.11: Vector's lengths without cracks.

When a crack starts to propagate, the plane and the normal vector $\vec{N}$ tilt because the relative potentials do not exhibit uniform increments (Fig. 2.12).

The location of the crack initiation site is determined by the opposite angle of the normal vector projected onto the x-y plane [23].

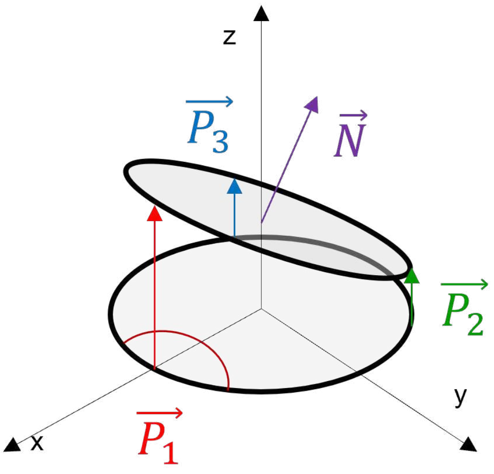

Figure 2.12: Vector's lengths with cracks.

In this specific figure, as an example, the assumption is made that the crack initiates and propagates at probe P_1. This assumption is based on the observation that, at the given generic instant being considered, the length of vector P_1 is greater than the lengths of vectors P_2 and P_3. In addition, due to the symmetry, it can be inferred that the lugs P2 and P3 must be equal.

Through a series of calculations and conversions involving cylindrical coordinates within a Cartesian coordinate system, followed by reverse transformations, it becomes possible to deduce the normal vector $\vec{N}$ and so the crack initiation point given by the following equation.

$$\phi = 180 - \Phi \tag{2.6}$$

This determination is feasible due to the equivalence between the angle-coordinate of the normal vector and the crack angle, both of which carry the same information [22]. The three components of the normal vector in cylindrical coordinates can be represented as follows:

$$\vec{N} = \begin{pmatrix} N \\ \Phi \\ \Psi \end{pmatrix} \tag{2.7}$$

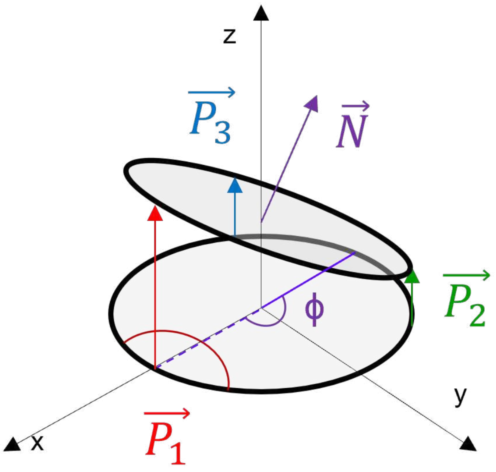

Figure 2.13: Crack position calculation.

This assessment enables the creation of a graphical representation illustrating the relationship between the ϕ value and the number of cycles. The graph's outcome serves as a precise indicator of the point at which fatigue-induced crack initiation occurs.

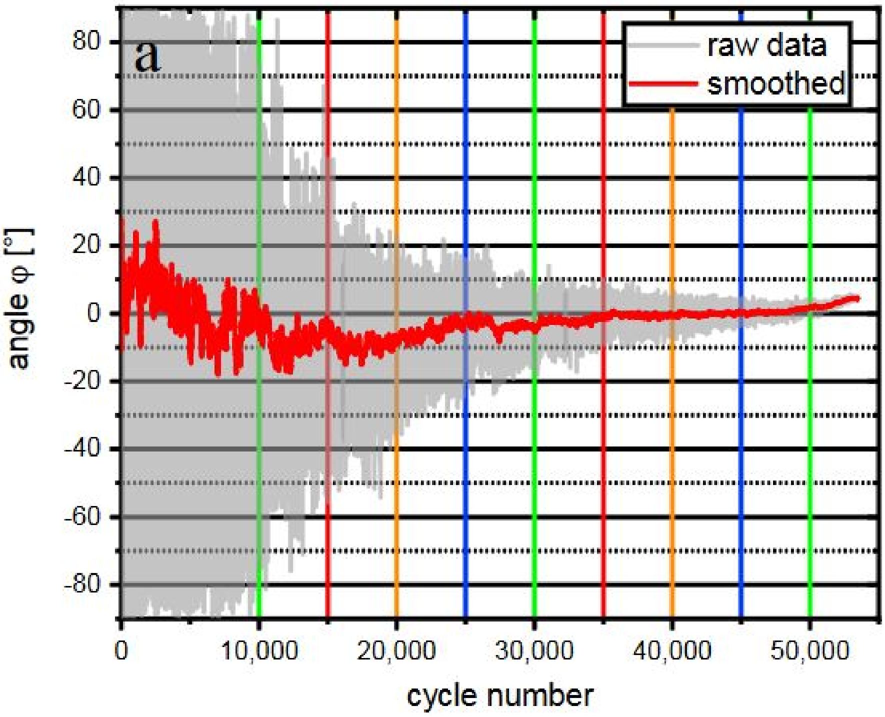

Figure 2.14: Calculated angle. Image taken from [21]

In this given example, the angle ϕ represents the angle between the crack initiation point and the position of probe P_1. Since the crack initiation corresponds to the position of probe P_1, the measured value of the phi angle is zero.

This vectors model was initially employed to determine solely the crack initiation point, providing no indication of the actual size. A significant advancement occurred in 2022 during another research conducted by Mike Nahbein and Jürgen Bär [22], where the radius-coordinate of the normal vector N was used as a criterion for estimating the crack size. Specifically, this coordinate N is plotted against the relative broken area $\frac{a_f}{W_f}$, calculated by dividing the broken area a_f by the total cross-sectional area W_f of the specimen. The plot illustrates a distinct nonlinear relationship between the two quantities and this relationship enables a precise determination of the broken area. In order to use the model independently of the starting position of the crack or, for instance, for in-situ measurements, a mathematical correlation between the radius-coordinate of the normal vector (N) and the crack size, i.e., the relative fractured surface $(\frac{a_f}{W_f})$, is required [22].

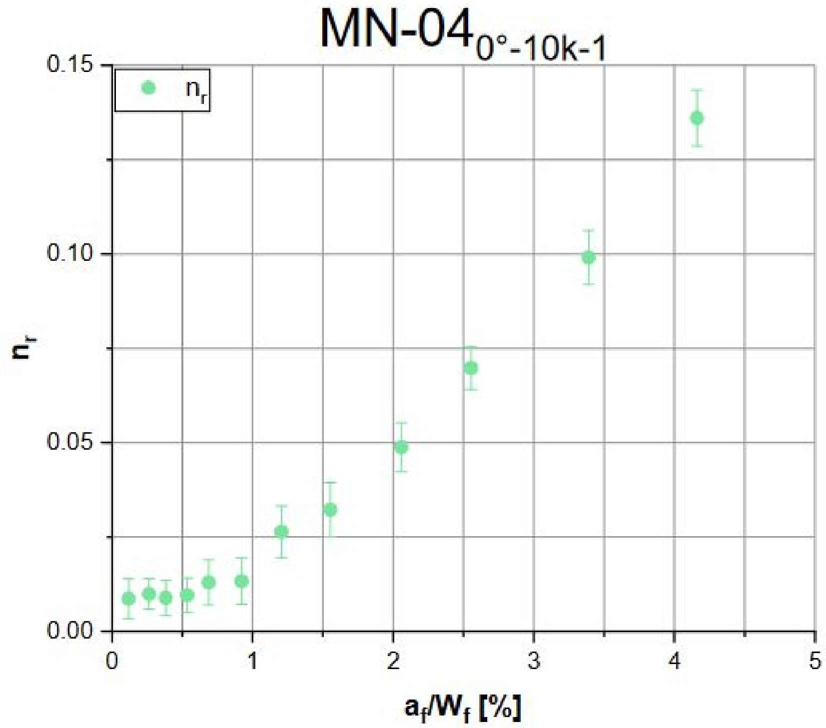

Figure 2.15: Diagram of the radius-coordinate of the normal vector n_r against the relative broken area a_f/W_f. Image taken from [22]

A first proposed solution for finding the desired correlation involves using a readjusted form of Johnson's formula 2.3, which is often used to calculate crack length from potential drop data [19, 22].

$$\frac{a_f}{W_f} = \frac{2}{\pi} \cdot \arccos \left\{ \frac{\cosh\left(\frac{\pi \cdot y_0}{2 \cdot W_f}\right)}{\cosh\left[(N+1) \cdot \operatorname{arcosh}\left(\frac{\cosh\left(\frac{\pi y_0}{2W_f}\right)}{\cos\left(\frac{\pi a_{f,k}}{2W_f}\right)}\right)\right]} \right\} \tag{2.8}$$

This Johnson's formula bases on the nonlinear correlation between the relative broken area $\frac{a_f}{W_f}$ and the radius-coordinate of the normal vector N as well as the half distance between the connection points of the potential probes y_0 and the size of the secondary starter notch $\frac{a_{f,k}}{W_f}$ [22].

A second mathematical correlation can be employed to fit the data and then compare the results obtained with Johnson's formula to determine which one better fits the experimental points. This formula, proposed by Tiedemann in 2016 [15], correlates the relative fracture area with n_r and two parameters: q, representing the inclination of the fitted curve, and t, representing the curvature.

$$\frac{a}{W_f} = q \cdot (N)^t + \frac{a_{f,k}}{[m^2]} \tag{2.9}$$

Finally, to evaluate the results, a graph was constructed, presenting the results of multiple experimental tests, and the two presented formulas (2.8 - 2.9) were compared.

These results clearly indicate that the length of a crack initiated at the surface of a notched round bar can be calculated using the three measured potential drops with high accuracy. The multiple potential measurements are excellent not only for determining the crack location but also for accurately determining the crack size, regardless of the crack initiation site's location on the circumference of the specimen [22].

Within this study, a similar approach is utilized, employing the same method and equations. However, a modification is introduced where, instead of using the relative fractured surface $\frac{a_f}{W_f}$, the relative crack depth $\frac{a}{r}$ is used. In this context, r represents the radius of

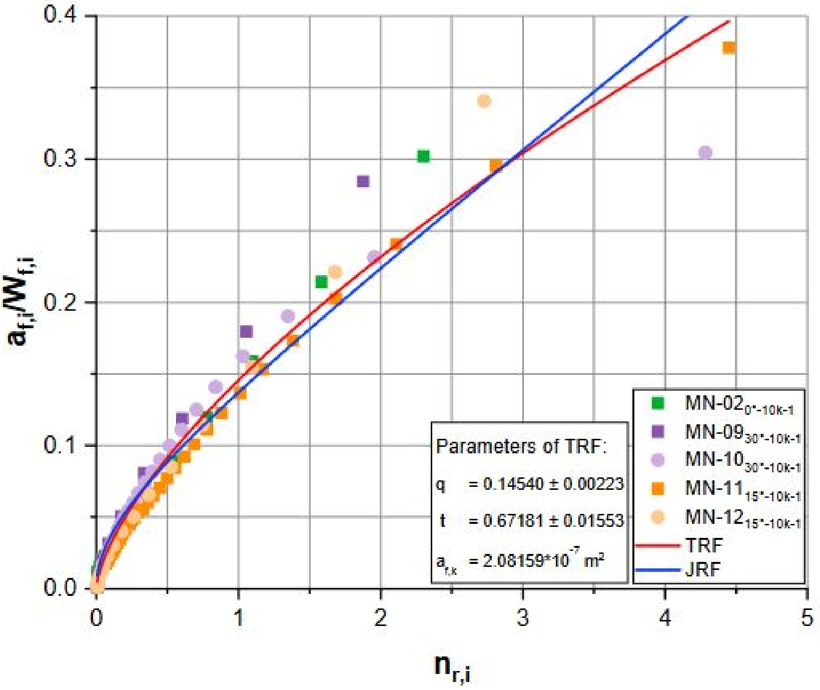

Figure 2.16: Fitting curves of JRF and TRF in comparison. Image taken from [22]

the specimen. For this reason, the equations 2.8 and 2.9 are modified as follows.

$$\frac{a}{r} = \frac{2}{\pi} \cdot \arccos \left\{ \frac{\cosh\left(\frac{\pi \cdot y_0}{2 \cdot r}\right)}{\cosh\left[(N+1) \cdot \operatorname{arcosh}\left(\frac{\cosh\left(\frac{\pi y_0}{2r}\right)}{\cos\left(\frac{\pi a_{f,k}}{2r}\right)}\right)\right]} \right\} \tag{2.10}$$

$$\frac{a}{r} = q \cdot (N)^t + \frac{a_{f,k}}{r} \tag{2.11}$$

These two equations (2.10-2.11) can be used to describe the mathematics correlation between the relative crack depth $\frac{a}{r}$ and the radius-coordinate of the normal vector N.

FE calibration

Despite several experimental, analytical, and numerical methods have been adopted in the literature to derive the calibration curves of the potential drop method (PDM), in this section the focus goes to the calibration employing FE analysis. Numerical calibrations enable the treatment of various specimen geometries and PDM operating conditions. Moreover, they are less complex than analytical calibrations and require less time com-

pared to experimental calibrations. It's worth noting that numerical calibrations also facilitate the investigation of various parameters, mainly those of a geometrical nature or related to the PDM settings, and potentially allow for optimization [8].
In the early contributions on this topic, 2D FE models were adopted to study the effect of the positions of the current and of the potential probes on the calibration curves of SEN and CTS fracture specimens [26, 11], or evaluate the effect of the potential probes locations on V-notched components [14]. It was also studied, the effects of the notch geometry, of the current input and of the mesh size adopted in the FE model [29, 8].

Nowadays, with the aid of IT tools, conducting 3D FE analysis has become possible [25, 17]. The process of obtaining PDM calibration curves, explained by Campagnolo et al. [8], using 3D finite element analysis while considering specimen geometry and loading conditions is explained in detail below. The calibration curves have been derived by means of 3D electrical FE analyses of the specimen geometries. All numerical models have been analysed by using 3D, 10-node, tetrahedral, electric solid elements (SOLID 232 of Ansys element library). To reduce the computational effort, half geometry has been considered and anti-symmetry boundary conditions have been applied on the specimen net-section, which translates into a 0-V-electrical-potential applied only to the un-cracked portion of the net-section area, to simulate the absence of electric contact between crack surfaces. Several FE analyses were conducted to evaluate various crack geometries and diverse specimen geometries. The results obtained from these analyses in this research are now presented [8].
Figure 2.17 reports the results in terms of ratio $\frac{\Delta V}{\Delta V_0}$ as a function of the normalized crack depth a/r (r being the radius of the net-section), for a circumferential crack in notched and plain specimens, respectively. It can be observed from Figure 2.17A that the smaller the notch tip radius ρ, the more sensitive the PDM.

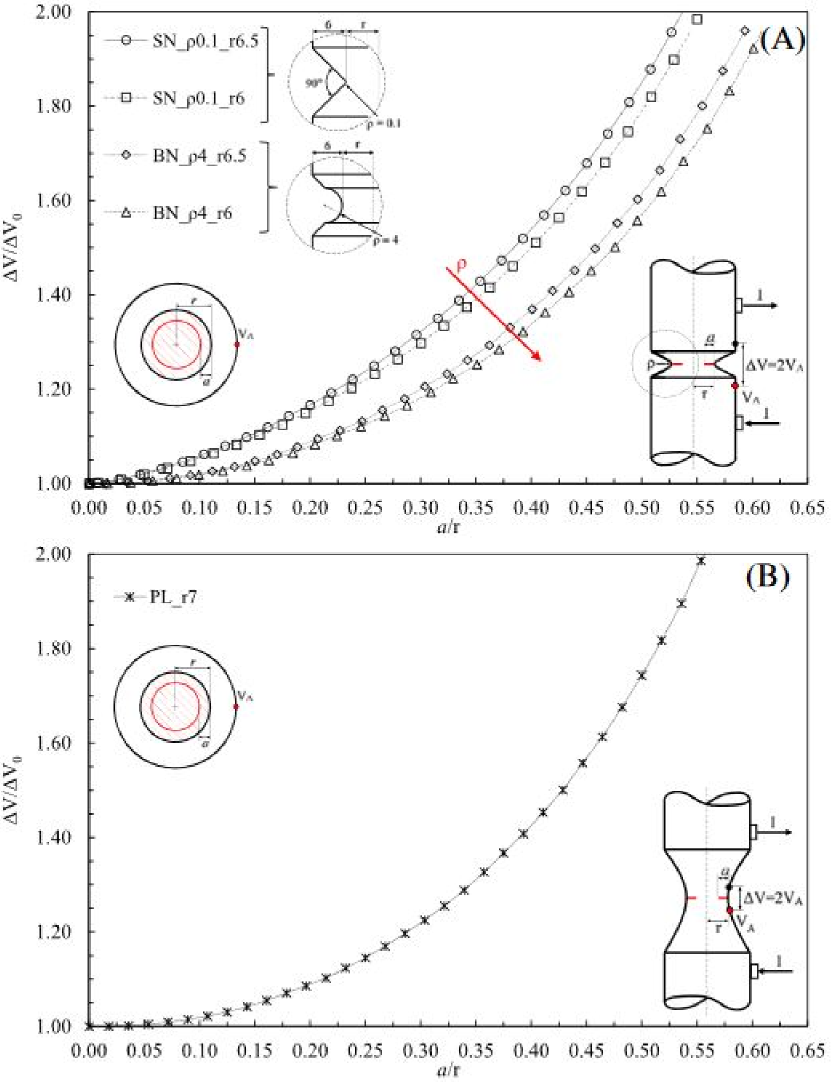

Figure 2.17: Calibration curves for a circumferential crack in the case of (A) notched and (B) plain specimens. ΔV_0 is the electrical potential of the reference un-cracked specimen (a = 0). Image taken from [8]

Figure 2.18 that the maximum sensitivity holds for two cracks at 0° and 180°, respectively, the reduction of the specimen transverse section being maximum as compared with the other cracked configurations reported in the figure. In the case of a single crack, the lower the crack angular position Θ, the more sensitive the PDM for a fixed crack aspect ratio c/a. Other examples with various geometries are available in the Campagnolo et al. search [8].

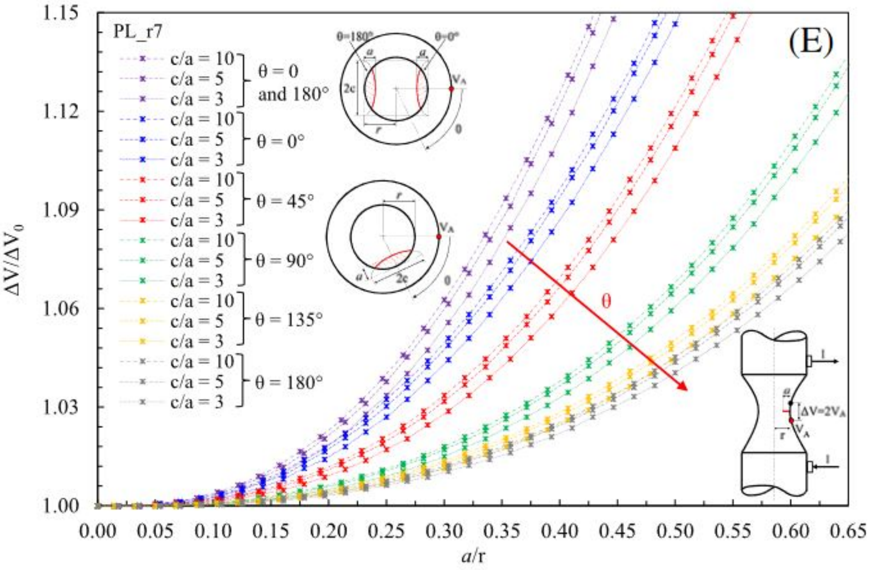

Figure 2.18: Calibration curves for a semi-elliptical surface crack in the cases of plain geometry. Image taken from [8]

Hence, it can be firmly concluded that employing this type of PDM calibration using 3D finite element (FE) analysis proves to be highly effective and in good alignment with experimental data.

Chapter 3

Materials and Methods

This section elucidates the practical aspect of this research. It delves into the details of specimen preparation, outlines the setup of the machinery, and elucidates the process of results analysis. Moreover, the chapter provides a comprehensive overview of all the employed equipment.

3.1 Specimen geometry and experimental set-up

Geometry and material

The geometric characteristics of the specimens are illustrated in the accompanying Figure 3.1. The specimens have been crafted from a solid bar employing the technique of lathe machining. This method involves material removal in order to achieve a specific dimensions. In this regard, the net section diameter has been established at $d_{\text{nett}} = 8$ mm, while the gross section diameter has been honed to measure $d_{\text{gross}} = 20$ mm.

All the tested specimens are made of AISI 304 stainless steel, also known as X5CrNi18-10. The table below provides a summary of the chemical and mechanical properties according to European legislation EN 10088-1 [6].

C (%)	Mn (%)	Si (%)	Cr (%)	Ni (%)	P (%)	S (%)
0.08	2.0	1.0	11.0-18.0	8.0-10.5	0.04	0.03

Table 3.1: Chemical composition of the austenitic stainless steel, AISI 304

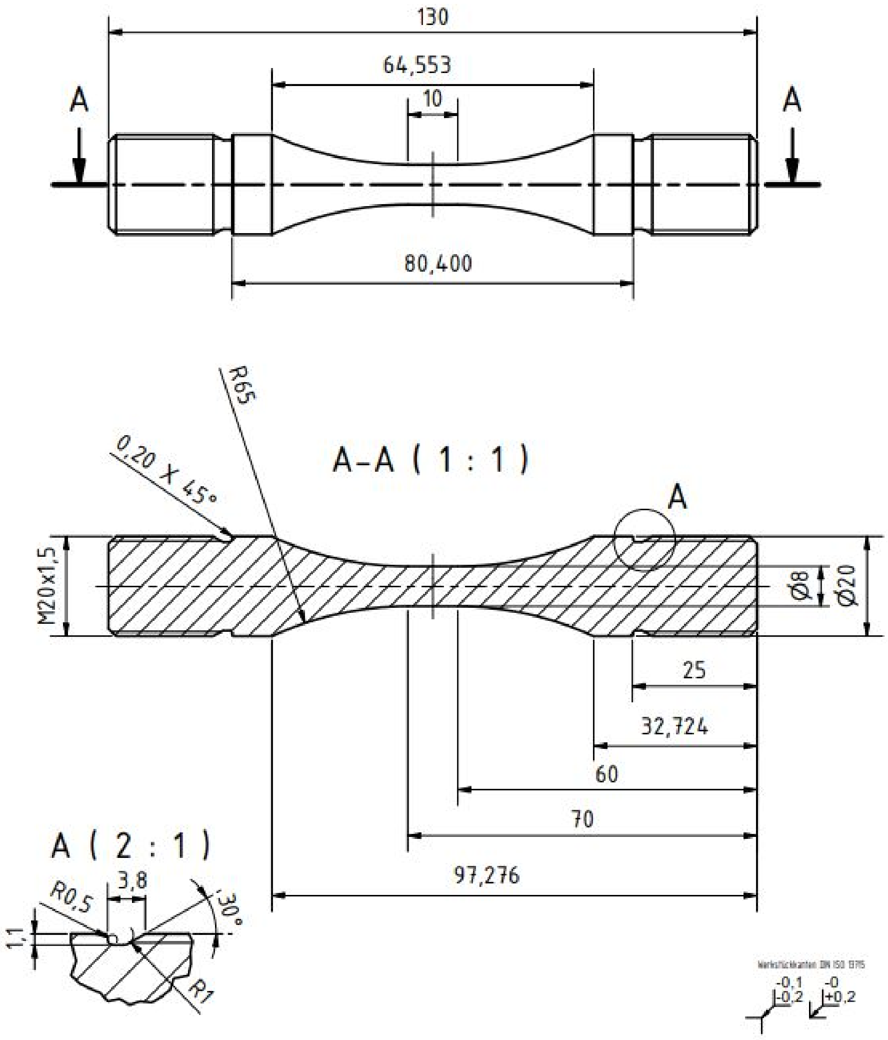

Figure 3.1: Specimens geometry

Property	Unit	Value
Young's modulus	[GPa]	196
Poisson's ratio	[-]	0.3
Density	[g/cm^3]	8.06
Yield stress	[Mpa]	205
Ultimate tensile stress	[Mpa]	515
Electrical resistivity at 20°C	[$\mu\Omega \cdot cm$]	71-78

Table 3.2: Mechanical and physical properties of the considered materials

Specimen configuration

The experimental configuration selected for the direct current potential drop method employs a setup comprising three potential probes positioned at intervals of 120 degrees from each other (Fig. 3.2). It has been experimentally verified that this method is effective for estimating the position and depth of a propagating crack in a notched specimen [22]. The aim of this study is to replicate the procedure illustrated in Chapter 2 with the specimens shown in Fig. 3.1.

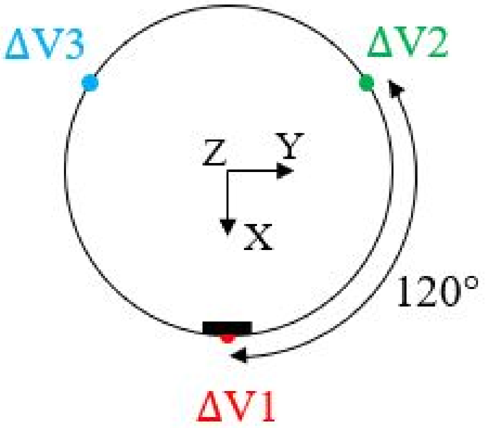

Figure 3.2: Experimental DCPD setup

Unlike notched specimens, the positioning of the potential probes in this type of specimen is by no means trivial. In fact, for the latter, the axial position of the crack initiation point is not known.

For these reasons, different potential grips distances were tested; starting from the most distant probes configuration to the closest possible configuration.

In order to ensure a precise result and to avoid multiple cracks trigger points, a small secondary notch was made in the test piece to ensure a single crack trigger. In addition, different secondary notch positions were tested to evaluate the effectiveness of the method. A summary table collects all the different configurations tested; $2Y_p$ is the distance between the potential grips, θ_n is the angle between potential probe one and the secondary notch and $\frac{y_1}{y_2}$ indicate the symmetry along the specimen's axis.

Specimen's code	$2Y_p$ [mm]	θ_n [°]	$\frac{y_1}{y_2}$
AC03	65	0	1
AC04	65	0	1.28
AC05	65	60	1
AC06	65	60	1.28
AC07	65	30	1
AC08	10	0	9
AC09	10	60	1
AC10	10	60	1
AC11	4	0	1
AC12	4	0	1

Table 3.3: Different specimen's configurations

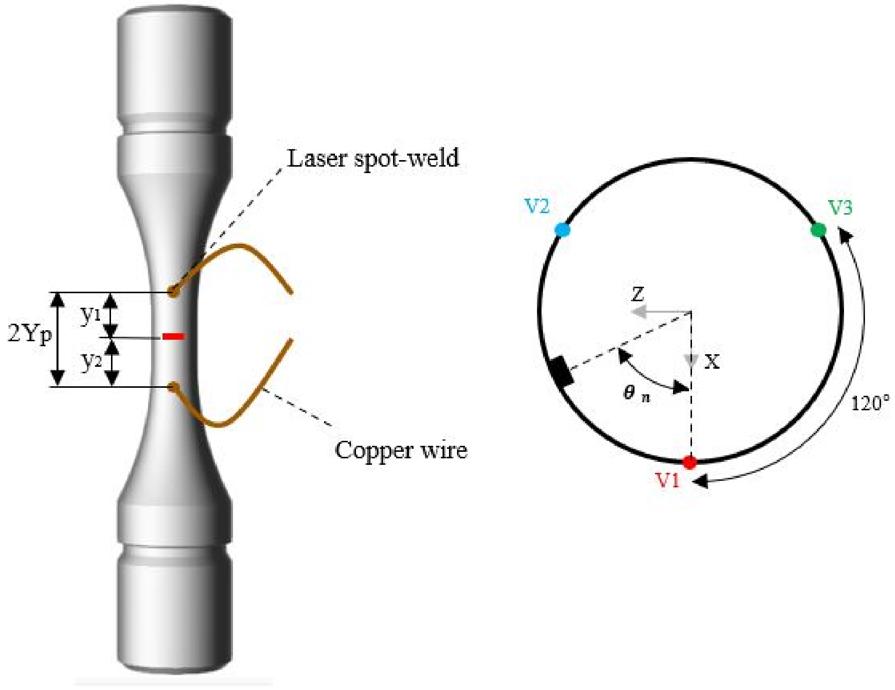

Figure 3.3: Specimen configuration

Secondary notch realization

The process for creating the secondary notch is as follows. An engraving laser model "TruMark Station 5000" of TRUMPF (Fig. 3.5b) was employed to perform the marks accurately. After clamping the specimen on the machine a simple CAD model of the notch is designed. In this case, a 1.3 mm line for the wide of the secondary notch, while the depth is controlled by the laser parameters showed in Tab. 3.5a. These parameters where meticulously tested on dummy sample in order to obtain a smooth secondary notch profile with a depth of 0.2 mm.

With the same machine and same clamping, some reference marks on the specimens surface had been done in order to obtain an 120° angle between the potential probes and the desired distance between the potential grips.

Figure 3.4 shows a microscope image of a secondary carving.

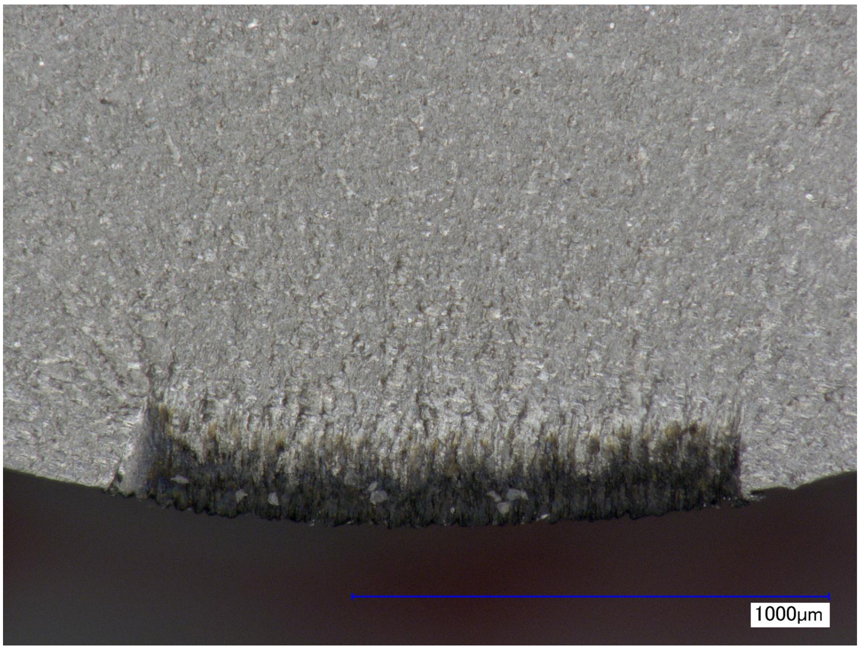

Figure 3.4: Notch dimension

Parameter	**Value**	**Unit**
Track width	0.05	mm
Power	50	%
Speed	2	mm/s
Pulse frequency	7000	Hz
Pulses per point	10	-
Pulse width	4	μs

(a) Parameters

(b) TRUMPF TruMark Station 5000

Figure 3.5: Engraving laser TruMark Station 5000

Welding wires

After that, six copper wires with a diameter of 0.22 mm were welded on the specimen to measure the potential. A handheld welding laser model VL50 by ALPHALASER (FIg. 3.6b) was employed with the parameter shown in Tab.3.6a.

Parameter	Value	Unit
Voltage	160	V
Pulse duration	5	ms
Speed	2	mm/s
Beam diameter	0.2	mm
Pulse energy	1.65	J

(a) Parameters

(b) ALPHALASER handheld welding laser VL50

Figure 3.6: Welding laser machine AlphaLaser VL50

Since the weld size was small (ca. 0.6 mm), some strategies were adopted to make it more stable. Some polish was applied directly on the weld and the wire was attached to the specimen with some tape. This process was executed very carefully in order to avoid secondary contact points between the wire and specimen.

Figure 3.7: Weld spot dimension

Indeed, in certain specimens where this approach was not implemented, an irregular potential trend was observed, highlighting the existence of an unstable and nonuniform link between the copper wire and the specimen, as exemplified in Fig. 3.8.

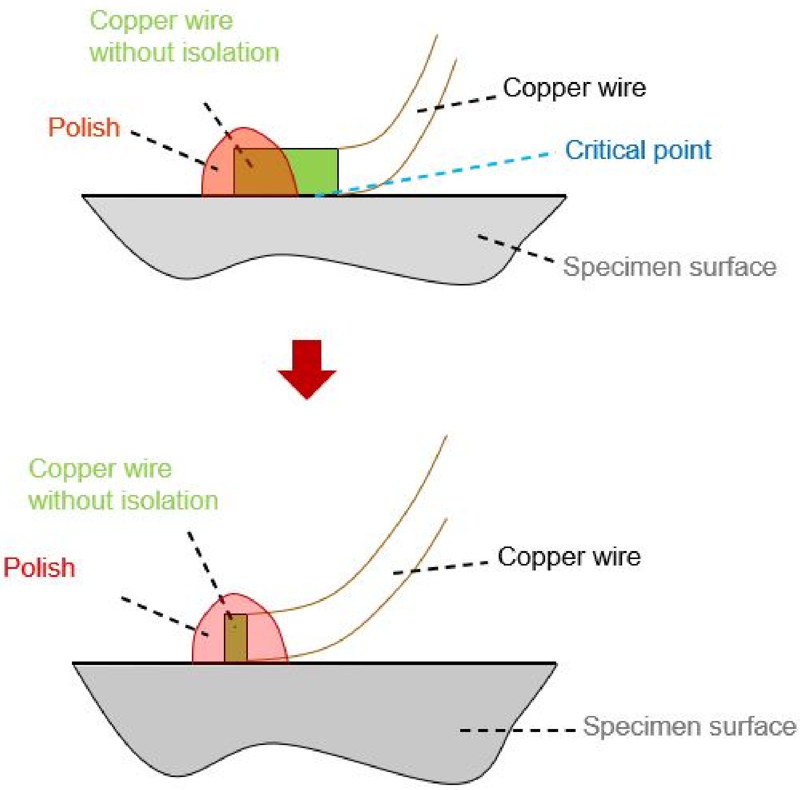

Figure 3.8: Wire preparation

3.2 Test machine setup

All the tests described were carried out with a servo-hydraulic testing machine type "PSB" from Schenck, which can apply a maximum test force of 100 kN (Fig. 3.9).
The round specimens were force-fitted by screwing them into the holding fixtures and, subsequently, they were fatigued under force control until they broke.

The control electronics employed was the system EDC580V from DOLI Elektronik GmbH. The latter is able to control the testing machine and to record the test data with the aid of the software "Test&Motion" from the same company.

Regarding the operational parameters of the Potential Drop Method (PDM), a consistent electrical current has been applied across the specimen by means of a machine called TDK-Lambda. This machine transmits current to the test specimen through a pair of

$2Y_p$	**Current**	$\Delta V_{\mathbf{i,0}}$
65 [mm]	1.6 [A]	0.91 [mV]
10 [mm]	4 [A]	0.6 [mV]
4 [mm]	7.6 [A]	0.5 [mV]

Table 3.4: Current values

electrical cables. These cables are connected to the clamping system using two screws, establishing the electrical connection necessary for the tests. The magnitude of the applied current undergoes changes contingently on the parameter $2Y_p$ resulting in alterations in the electric potential measurements for the un-cracked configuration ($\Delta V_{\mathrm{i,0}}$). These measurements typically exhibit values in the range between 0.4 and 0.9 mV (Tab. 3.4).

Figure 3.9: Schenck testing machine and DOLI Elettronic system

Fully reversed (R = -1) axial fatigue tests were performed on the Schenck machine with different load condition varying with the PDM configuration. During the test the potential drops ΔV_i (i = 1, 2 and 3) were measured by using amplifiers (type 4FAD) of the control electronics operating with a sampling rate of 1 KHz.

In the following table (3.5) the value of the loads of the fatigue tests are presented. As highlighted in 2, in order to facilitate a direct comparison between the measured potential drop and the actual crack geometry, overloads were employed to mark the crack front, as shown in Fig. 3.12. Figure 3.11 show how the load is applied during the test, in particular σ_{BL} is the Base load, σ_{OL} represent the overload while N_{OL} is the distance between overloads.

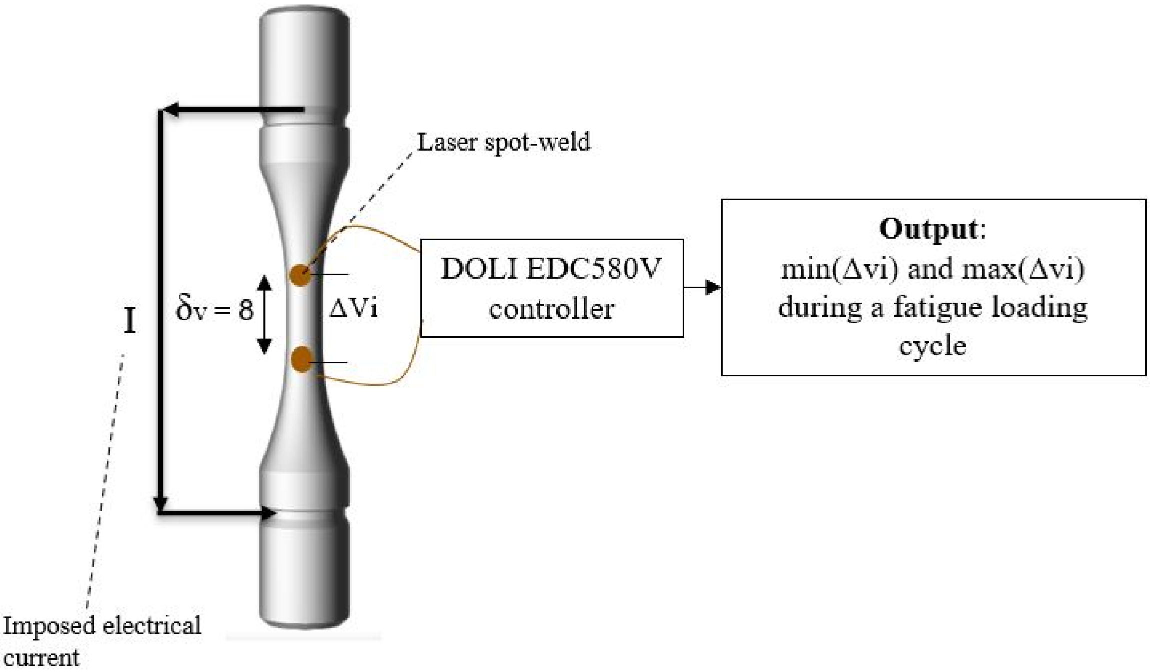

Figure 3.10: Experimental setup. δV is the distance between the two ends of each potential probe.

Specimen code	AC03	AC04	AC05-06	AC07-08-09-10	AC11-12
Base load [kN]	12	12	11	11.5	12
Overload [kN]	20	20	19	19.5	20
Repetitions [cycle]	1.5×10^4	1.0×10^4	1.0×10^4	1.2×10^4	1.2×10^4
Warm-up [cycle]	5×10^4	5×10^4	5×10^4	5×10^4	5×10^4
n° overload [-]	2	8	12 - 28	8 - 8 - 6 - 16	5 - 16

Table 3.5: Load description

Figure 3.12: Crack surface overload

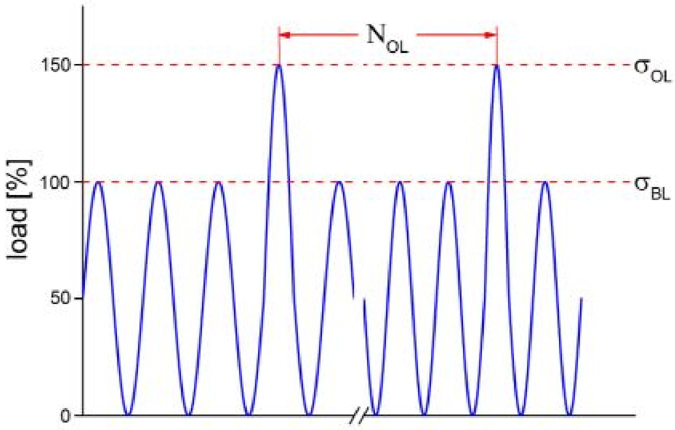

Figure 3.11: Mode of load application

Temperature measurement

The Direct Current Potential Drop Method (DCPDM) can be influenced by a range of external factors. For instance, alterations in temperature directly impact electrical resistance, leading to a subsequent elevation in the measured potential.

Given the low potential values, maintaining a consistent temperature is crucial throughout the experimental procedure. While the fluctuation in ambient temperature might not be a significant issue when employing servohydraulic testing machines, the primary concern lies in the potential heating of the oil of the testing machine. This heating effect can be bypassed introducing a temperature stabilization phase prior to the experiment.

During the latter phase, the temperature of the entire system can be levelled out, thus eliminating the chance of undesired temperature-related influences during the experiment [12].

For this reason, in the current study, 5×10^4 warm up cycles before the beginning of the test had been performed, applying a load of about 3kN. The graph in the figure 3.13 illustrates the maximum and minimum force values recorded in relation to the number of cycles. This graph highlights the difference between the warm-up phase and the actual work phase.

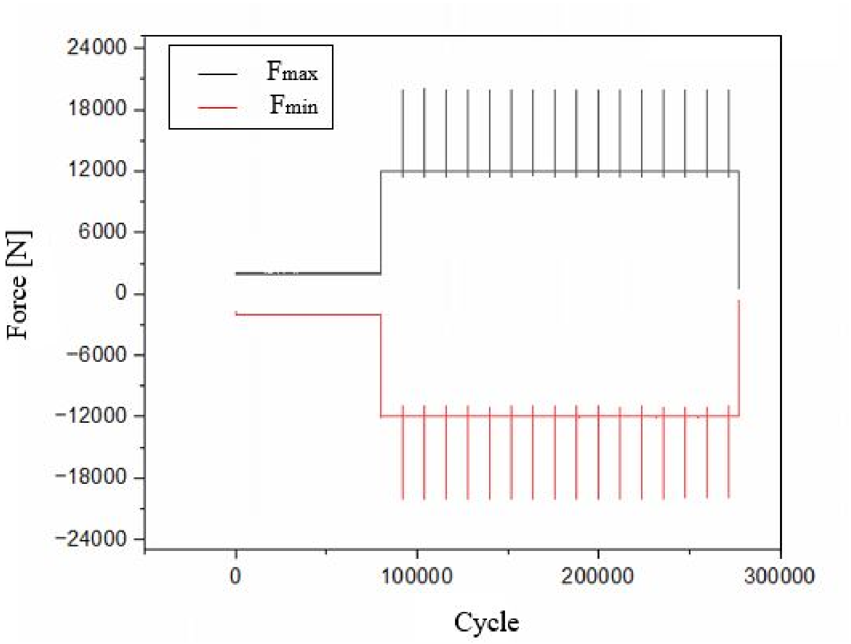

Figure 3.13: Warm-up phase and Working zone

For the purpose of monitoring the specimen's temperature throughout the testing process, a PT1000-type sensor was employed. This sensor was attached to the specimen's surface using tape, with precise positioning within the net section of the specimen. This specific location was chosen due to its heightened susceptibility to temperature fluctuations. The sensor remains consistently linked to the aforementioned electronic system, which in turn captures and logs the maximum temperature readings at one-minute intervals.

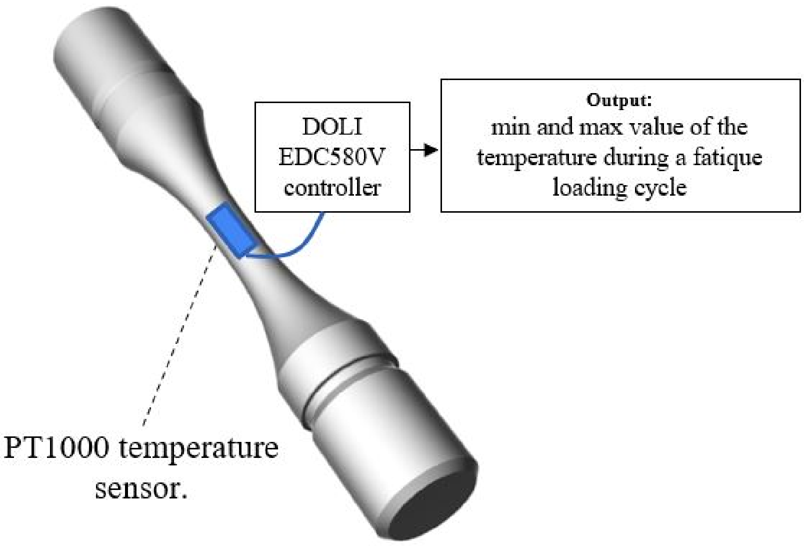

Figure 3.14: PT1000 temperature sensor set-up

The figure 3.15 displays a picture of the final specimen setup. In this image, one can clearly observe the thin copper wires connected to the surface of the specimen at the marked red spots. Additionally, the two cables responsible for supplying the current to the test specimen are visible.

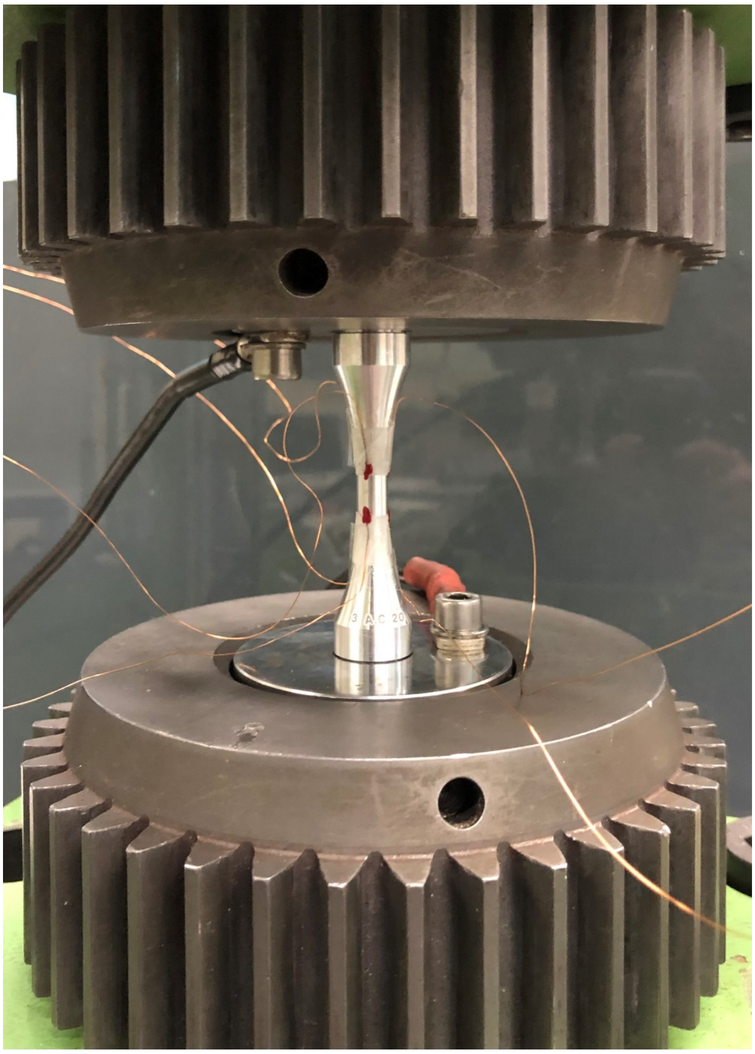

Figure 3.15: Specimen final set-up

3.3 Data Analysis

After fracturing each specimen, it becomes feasible to correlate the crack geometry observed during each overload event with the corresponding potential values measured by the probes. This data-set enables the establishment of a relationship between these two variables. Subsequently, this correlation can be utilized to calibrate theoretical or numerical models capable of predicting crack geometry solely based on potential value input.

Crack geometry analysis

Although they are also visible to the naked eye, a Keyence VHX-2000 brand digital microscope with a magnification of 150x was employed to capture the image of the overloads onto the crack surface. An example can be seen in Fig. 3.12.

With this magnified picture it is possible to measure the depth a and the area A of each overload as illustrate in Fig. 3.16, employing the software of the microscope.

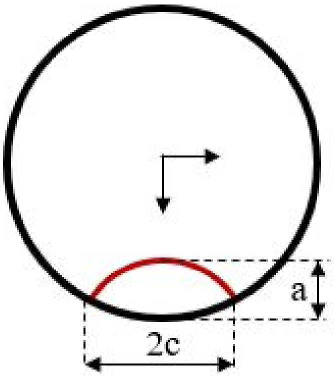

Figure 3.16: Measured dimensions at the fracture surface

All the data are then stored to Origin Pro software together with the data provided by the software Test&Motion of the potentials value measurements. This file contains all the information of each tested specimens; in particular:

- Number of cycles
- Maximum and minimum value of the applied force
- Maximum value of the potential measured for each probe (ΔV_1, ΔV_2, ΔV_3)
- Temperature measurement
- Value of the crack depth at each overload
- Value of the crack area at each overload

With all this information, it is possible to use the methods already introduced in the previous chapter to determine the crack initiation angle and find a correlation between the measured potential value and the actual crack depth.

Crack initiation angle

The same mathematical model illustrated in Chapter 2 for estimating the crack initiation angle was used in this research. A detailed list of operations carried out to achieve the objective follows.

Firstly, the relative potential values P_i' are calculated from the actual potential value ΔV_i and the potential of the specimen without cracks, denoted as $\Delta V_{i,0}$.

$$P_i' = \frac{\Delta V_i}{\Delta V_{i,0}} \qquad i = 1, 2, 3 \tag{3.1}$$

The relative potentials P_1', P_2' and P_3' are treated as vectors in cylindrical coordinate.

$$\vec{P_1} = \begin{pmatrix} r \\ 0° \\ P_1' \end{pmatrix} \quad \vec{P_2} = \begin{pmatrix} r \\ 120° \\ P_2' \end{pmatrix} \quad \vec{P_3} = \begin{pmatrix} r \\ 240° \\ P_3 \end{pmatrix} \tag{3.2}$$

The aim is to evaluate the normal vector $\vec{N}$ to the plane generated by these three vectors.

$$\vec{N} = \begin{pmatrix} N \\ \Phi \\ \Psi \end{pmatrix} \tag{3.3}$$

The procedure for calculating the components of the normal vector involves changing from cylindrical coordinates to Cartesian coordinates.

$$\begin{cases} x = r \cdot \cos\theta \\ y = r \cdot \sin\theta \\ z = z \end{cases} \tag{3.4}$$

Next, the normal vector is calculated using the vector product, and its components are again transformed into cylindrical coordinates.

$$\begin{cases} r = \sqrt{x^2 + y^2} \\ \phi = \arctan\dfrac{y}{x} \\ z = z \end{cases} \tag{3.5}$$

By implementing these operations in a calculation software such as Origin Pro for each potential value measured during the test, it is possible to evaluate the trend of the calculated ϕ value as a function of the number of cycles. This graph serves as an indicator of the crack initiation point. Notably, as the crack size grows, the accuracy in pinpointing the crack's location improves.

Analytical calibration curves

Analytical calibration curves were derived by solving the Johnson formula. The formula was adapted to match the geometry of the specimen being used. Furthermore, to utilize all three potential probes in the chosen configuration effectively, an additional modification was made to the formula. This modification involved utilizing the value of n_r from the normal vector N (Eq. 3.3) instead of focusing solely on a single potential difference. This particular value encapsulates information about the readings from all three probes.

$$\frac{a}{r} = \frac{2}{\pi} \cdot \arccos \left\{ \frac{\cosh\left(\frac{\pi \cdot y_0}{2 \cdot r}\right)}{\cosh\left[(N+1) \cdot \operatorname{arcosh}\left(\frac{\cosh\left(\frac{\pi y_0}{2r}\right)}{\cos\left(\frac{\pi a_{f,k}}{2r}\right)}\right)\right]} \right\} \tag{3.6}$$

First, a graph was plotted with n_r as a function of the parameter a/r, demonstrating a non-linear trend, as depicted in the example figure 3.17. Following this, Johnson's modified formula was simulated on this graph, with the specimen radius and the depth of the secondary notch set as fixed parameters, while the half distance between the potential grips y_0 left as a free parameter.

The same procedure was also employed using another mathematical relationship, specifically the Tiedemann equation discussed in Chapter 2. In this scenario, the only fixed parameter is the depth of the secondary notch $a_{f,k}$, while q and t are the two best-fitting parameters.

$$\frac{a}{r} = q \cdot (N)^t + \frac{a_{f,k}}{r} \tag{3.7}$$

FE calibration curves

In this section, the methodology for conducting finite element (FE) analyses to determine the calibration curves is explained. Essentially, the experiment is recreated in a virtual environment using Ansys APDL to enable a comprehensive comparison between the experimental and numerical results.

With this concept in mind, it is essential to have a comprehensive understanding of

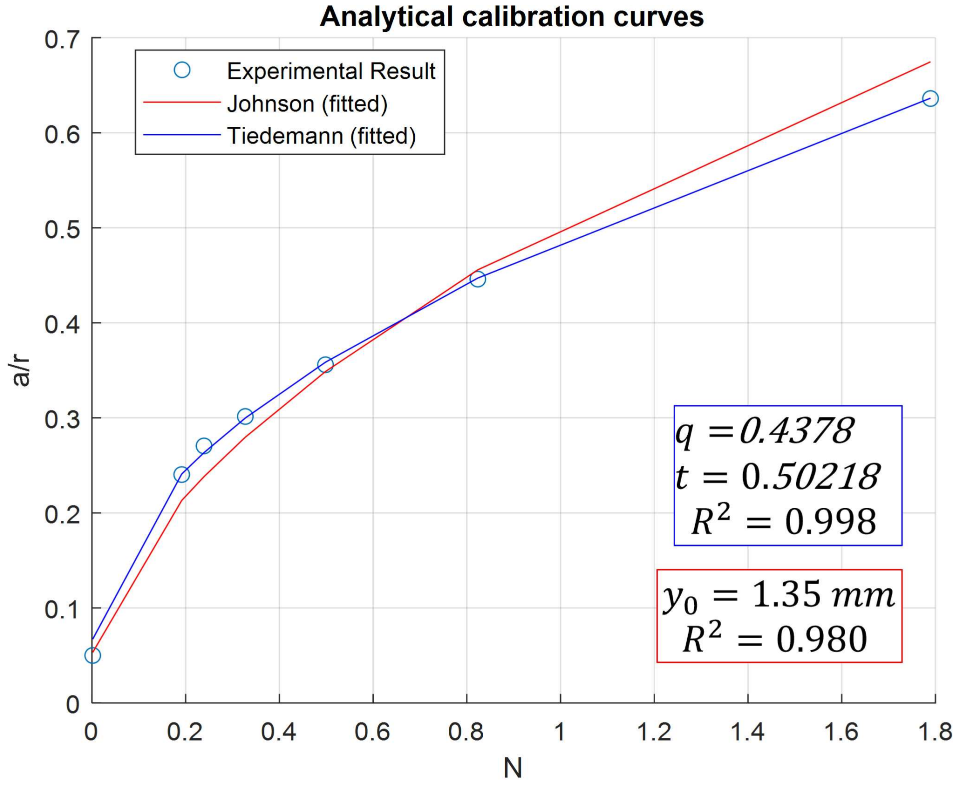

Figure 3.17: N and $\frac{a}{r}$ correlation

not only the specimen's geometry but also the geometry of the crack. As evident from the photos capturing the fracture surfaces of each specimen, the cracks exhibit a semi-elliptical shape. Consequently, it is imperative to determine, for each crack, the values of 'a', representing the depth, and 'c/a', where 'c' is the semi-axis length of the ellipse.

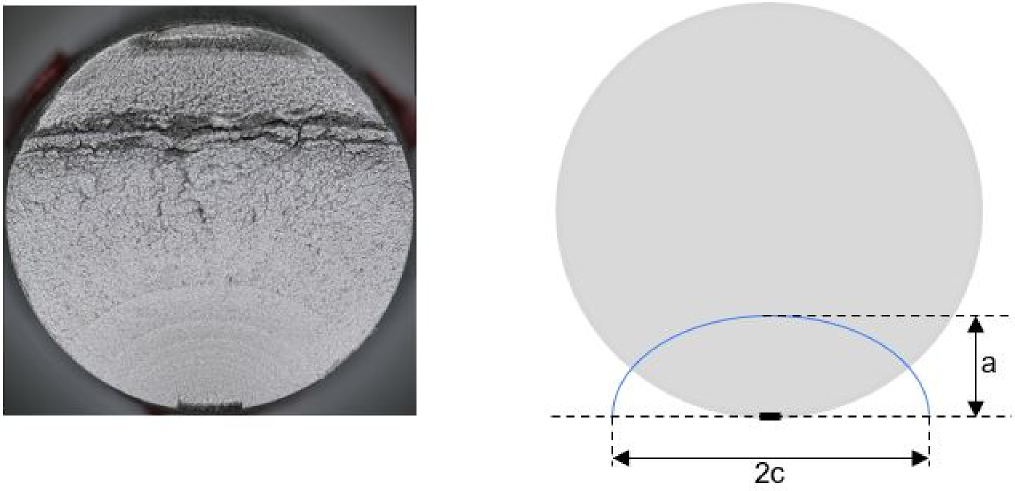

Figure 3.18: Semi-elliptical crack geometry

While the 'a'-value can be readily measured directly from the fracture surface using in-

struments such as a microscope, determining the semi-axis value is more intricate. To ascertain this value, it was necessary to construct a semi-ellipse that accurately represents the geometry of the true crack, allowing for the extrapolation of the desired value.
To do this, the image of the fracture surface was imported into a digital image processing tool where crack profiles were drawn following the mark left by the overload.

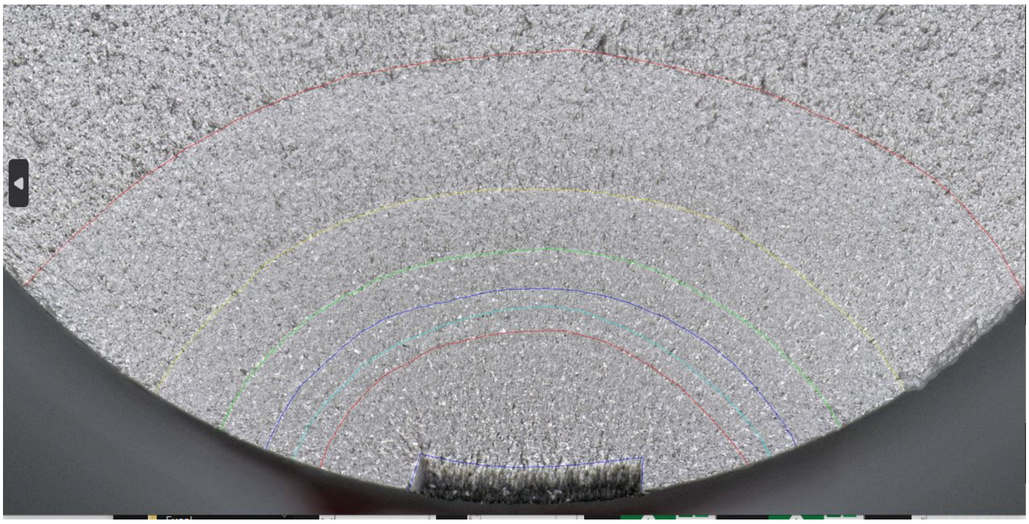

Figure 3.19: Digital image processing: marking overload lines

These traces enable us to utilize an online tool called 'WebPlotDigitizer' for extracting data directly from the image. More specifically, for each trace, the tool generates a series of points, which it provides in a *.txt format, containing coordinates (x, y).
By utilizing a straightforward MATLAB code, it becomes possible to determine the value of 'a' and the form factor 'c/a' by importing the coordinates for each overload conducted and fitting a semi-ellipse centered at the secondary notch. This procedure is repeated for all tested specimens, providing comprehensive results for each. Furthermore, in addition to determining the crack depth and form factor, the code also performs calculations for the crack area and its inclination with respect to the center. An illustrative example of the results obtained from one of the test specimens is shown graphically in Figure 3.20 and summarized in Table 3.6.

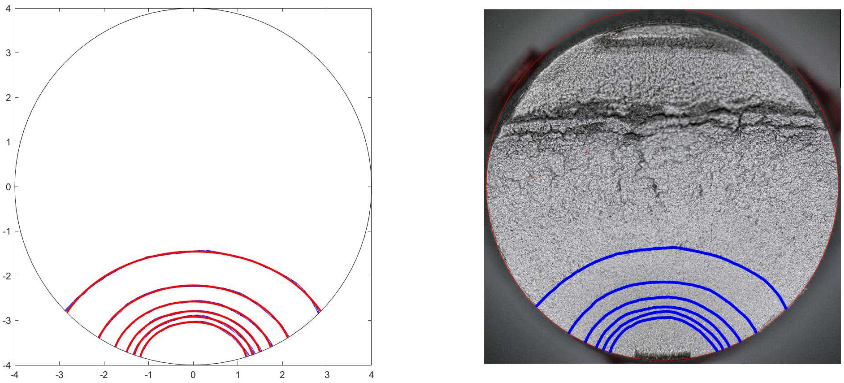

Figure 3.20: Fitted semi-ellipse path over specimen surface crack

N°	**a**	$\boldsymbol{\frac{c}{a}}$	θ	**Area**
[#]	[mm]	[-]	[grad]	[mm^2]
0	0.256	3.000	0.000	0.271
11	0.961	1.257	0.042	1.678
12	1.082	1.251	0.076	2.094
13	1.206	1.277	0.048	2.613
14	1.424	1.276	-0.040	3.567
15	1.784	1.263	0.086	5.373
16	2.544	1.265	0.289	10.162

Table 3.6: Matlab output for crack depth and form factor

The calibration curves have been derived by means of 3D electrical FE analyses of the specimen geometries. Dealing with semi-elliptical surface cracks, the effects of the aspect ratio c/a and the crack depth a, the crack angular position Θ_n with respect to the potential probes (see Figure 3.21), the distance of the between the potential grips $2Y_p$ have been investigated, according to the following FE analyses:

- The aspect ratio c/a was varied between 1 and 3, such range being appropriate with experimental results.

- The crack depth a was varied between 0.2 mm and 3.5 mm

- The angle Θ_n and the distance $2Y_p$ was controlled by means of a special grid designed on the specimen surface. Angle Θ_n varied between 0° and 180° with a step of 10°, while $2Y_p$ cover the entire length of the specimen with a step of 1 mm.

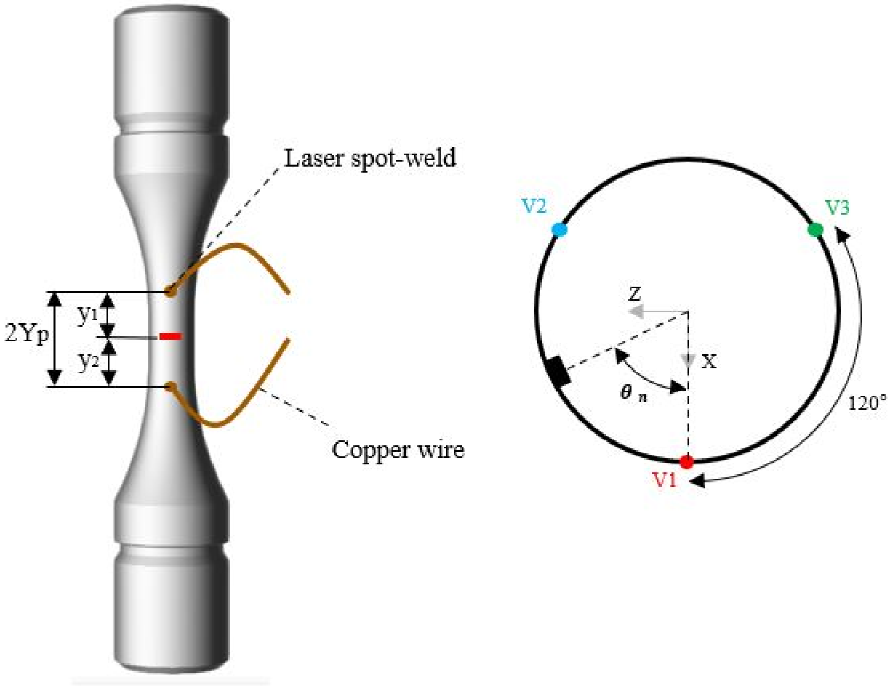

Figure 3.21: Specimen configuration: angular position Θ_n and distance $2Y_p$

All numerical models have been analysed by using 3D, 10-node, tetrahedral, electric solid elements (SOLID 232 of Ansys element library). To reduce the computational effort, half geometry has been considered and anti-symmetry boundary conditions have been applied on the specimen net-section, which translates into a 0-V-electrical-potential applied only to the un-cracked portion of the net-section area, to simulate the absence of electric contact between crack surfaces. To simulate the experimental set-up the applied current was input in all FE models [8]. To measure the potential drop ΔV between the two potential grips has been simply evaluated the value $2V$.

These analyses allow for the determination of potential values at various points on the specimen surface by taking into account various crack sizes and different shape ratio values; however, one important factor not taken into account is the load applied to the specimen and the resulting deformation it undergoes.

To evaluate the accuracy of the numerical results obtained, we conducted structural finite element (FE) analyses, followed by electrical analyses, employing the tool Ansys Workbench. The obtained results from both types of analyses were then compared for accuracy and consistency. More specifically, our objective was to evaluate not only the influence of the applied load but also the effect of the weld point shape. The presence of a weld spot creates a 'ball' approximately 0.5mm in size on the surface of the test specimen.

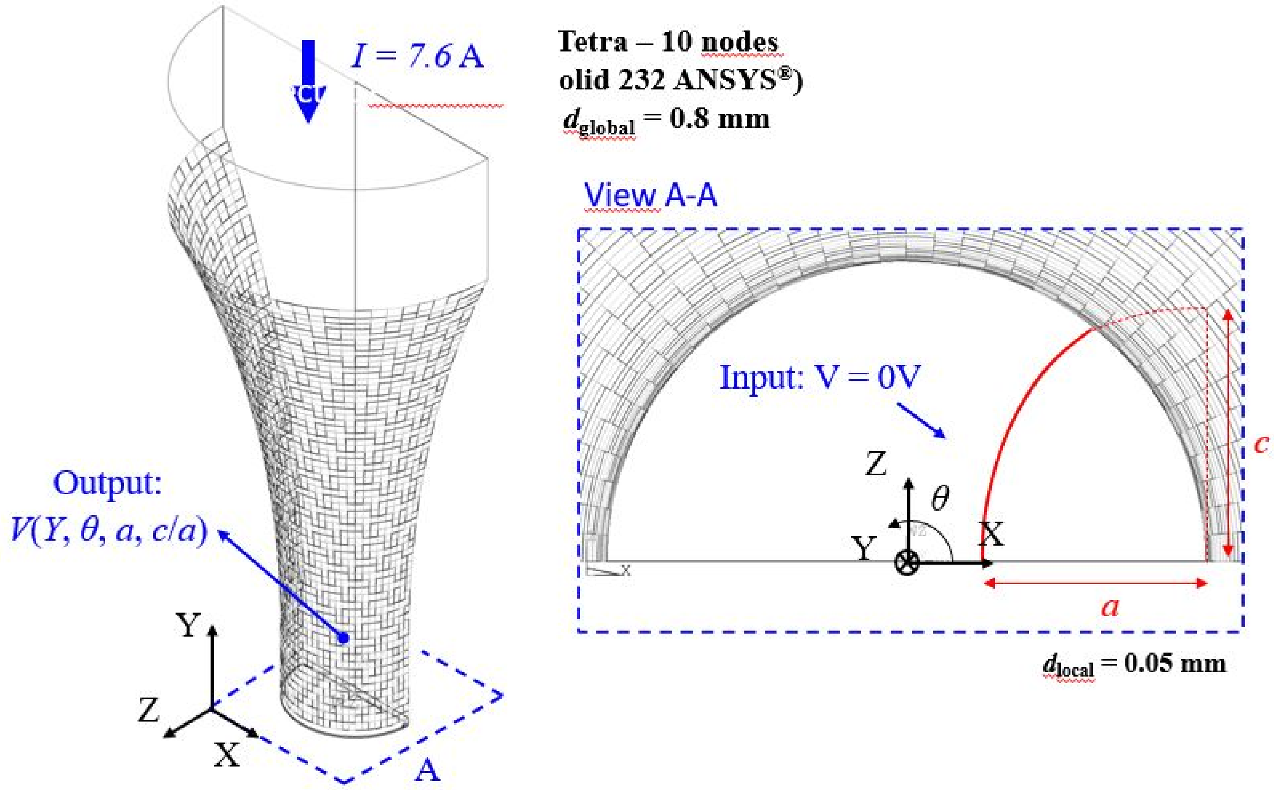

Figure 3.22: Specimen 3D design for electrical FE analysis.

Consequently, we aimed to assess how the finite element software integrates the potential values along the surface of this point and how it interacts with the applied load.

To conduct these analyses, it was imperative to model the geometry of both the specimen and the welding point in 3D using CAD software, specifically SolidWorks. Subsequently, we created the crack geometry within the ANSYS SpaceClaim environment. This allowed us to initiate the process by performing static structural analyses. The outcomes of these analyses were then utilized for electrical analyses, enabling the extraction of potential values at specified points.

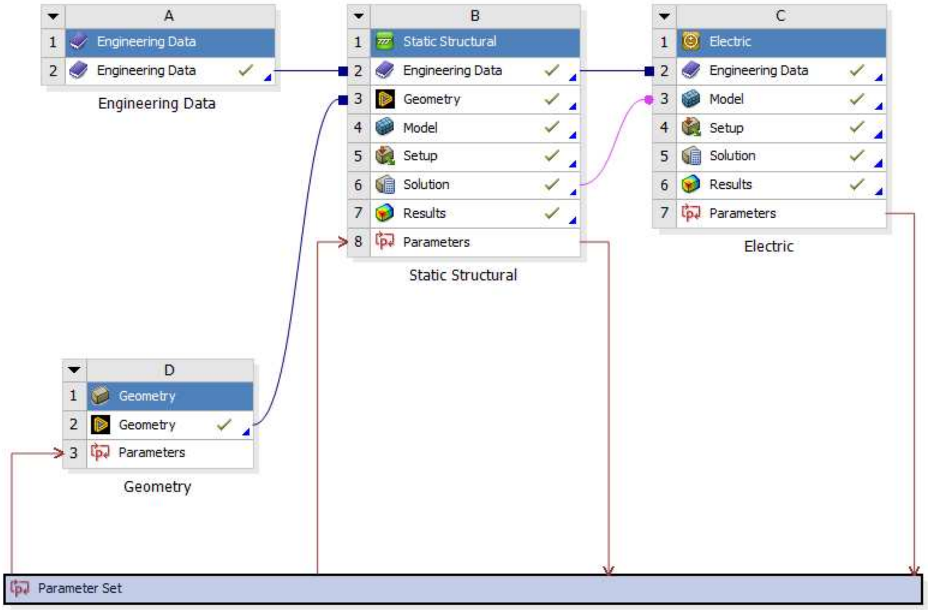

Figure 3.23: Workbench analysis steps

The image 3.23 shows the various steps of the analysis performed followed by the explanation of each step.

- On Engineering Data section the material properties of the specimen, specifically austenitic stainless steel X5CrNi18-10, were defined and entered into the ANSYS library. This particular steel has a Young's modulus of E=196 GPa and an electrical resistivity of ρ=7.9e-4 Ωmm.

  For the copper in the welding point, the material properties were defined using the values available in the ANSYS library.

- The specimen's geometry was depicted in a three-dimensional representation. The two images (3.24-3.25) below provide a visual representation of how the secondary notch and welding point were precisely created.

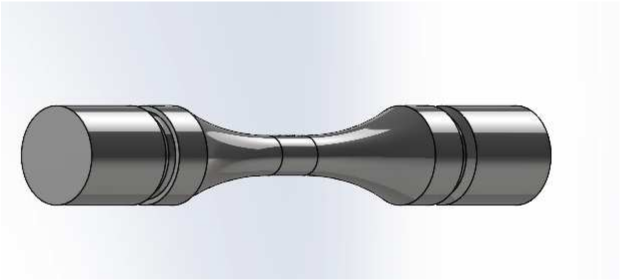

Figure 3.24: 3D Specimen Geometry (SolidWorks)

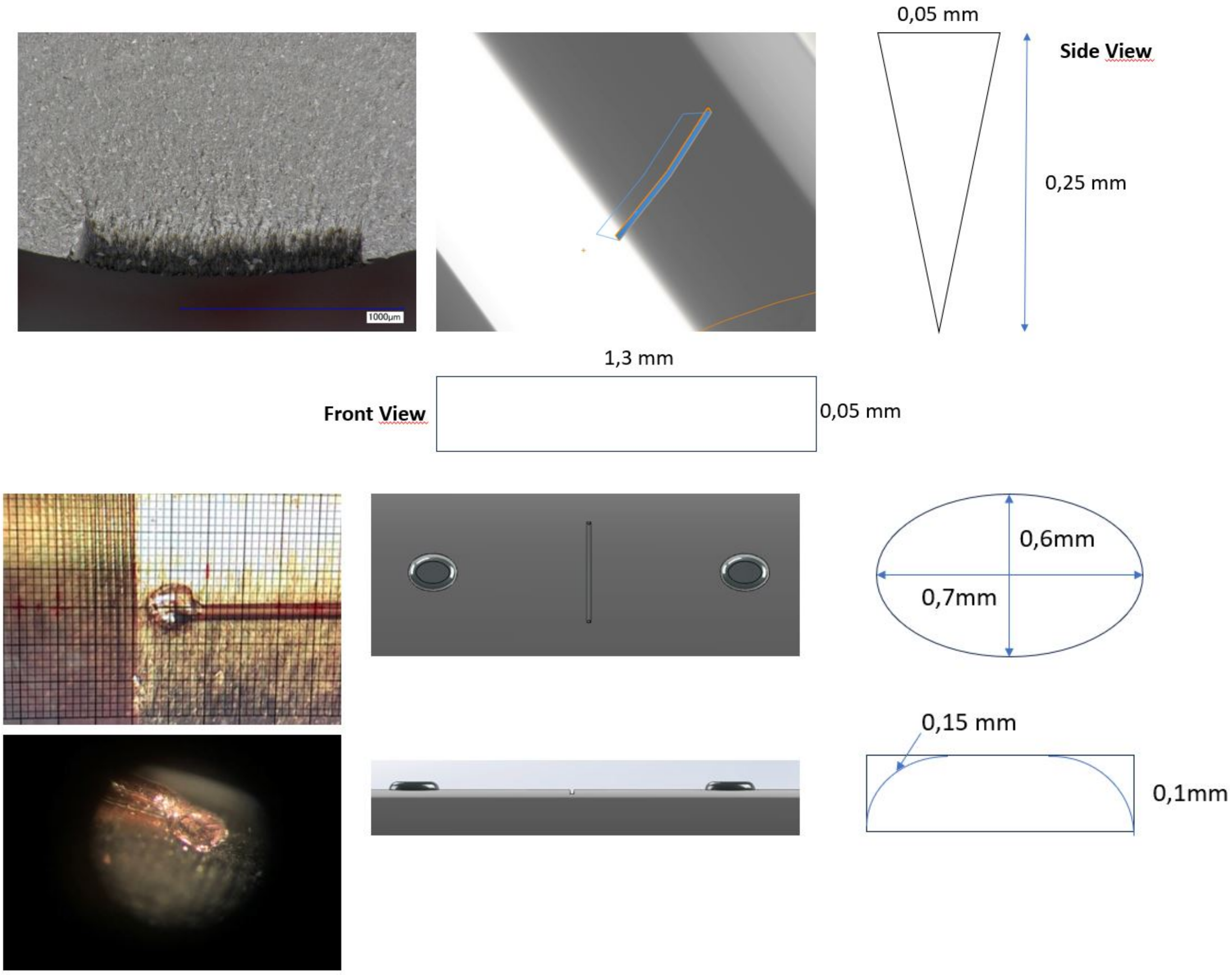

Figure 3.25: Secondary notch and Welding spot 3D geometry

- The geometry was subsequently imported into Ansys' SpaceClaim, where the crack geometry was created. The experimental parameters of a specific tested specimen, identified by the code AC12, were used as a reference to accurately represent the crack geometry.

- Following the assignment of materials for the specimen (steel) and the welding points (copper), the next step involved meshing the specimen. Tetrahedral elements, varying in size based on the specimen's geometry, were utilized for the meshing process.

- Having reached this point, it is possible to launch the structural static simulation by imposing constraints on the structure at the grips and applying a tension of 12kN.

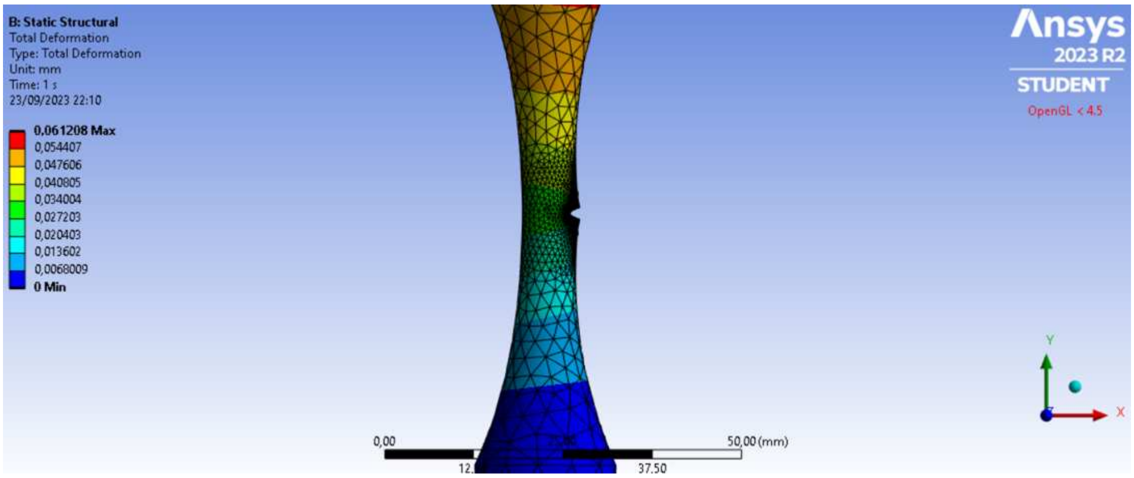

Figure 3.26: Static Structural FE Analysis

- Ultimately, the results obtained from the structural simulation were utilized as input for the electrical analyses. Specifically, the potential value on the surface of the welding point was meticulously recorded during these electrical analyses.

The subsequent chapter delves into a detailed discussion comparing the various results obtained from the analyses.

Chapter 4

Results

4.1 Temperature measurement results

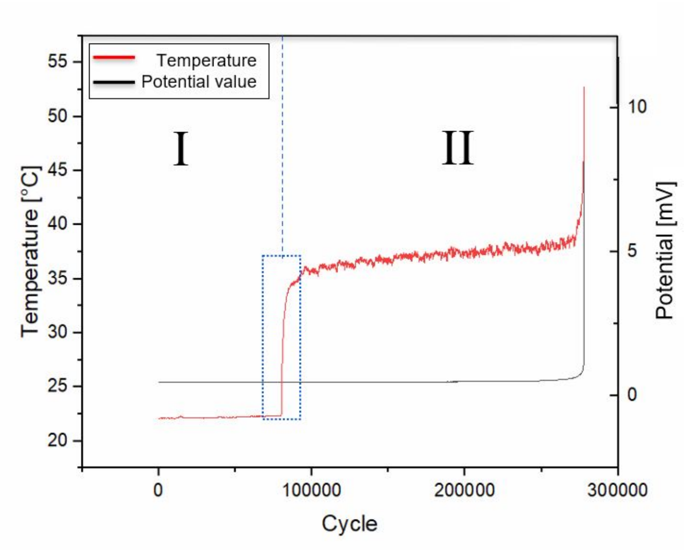

Figure 4.1: Temperature variation during the fatigue test

The resulting graph can be divided into two zones: the warm-up zone and the working zone indicated in Fig. 4.1 with I and II respectively. In addition, it is possible to zoom into the transition zone between the warm-up and work zone to assess how the change in temperature affects the potential reading.

In the designated warm-up phase using the specified parameter set, the temperature experienced a mere increase of 0.3°C, while maintaining the potential value at a constant level of 0.474-0.475 mV.

The temperature sensor indicated a substantial temperature shift between the warm-up

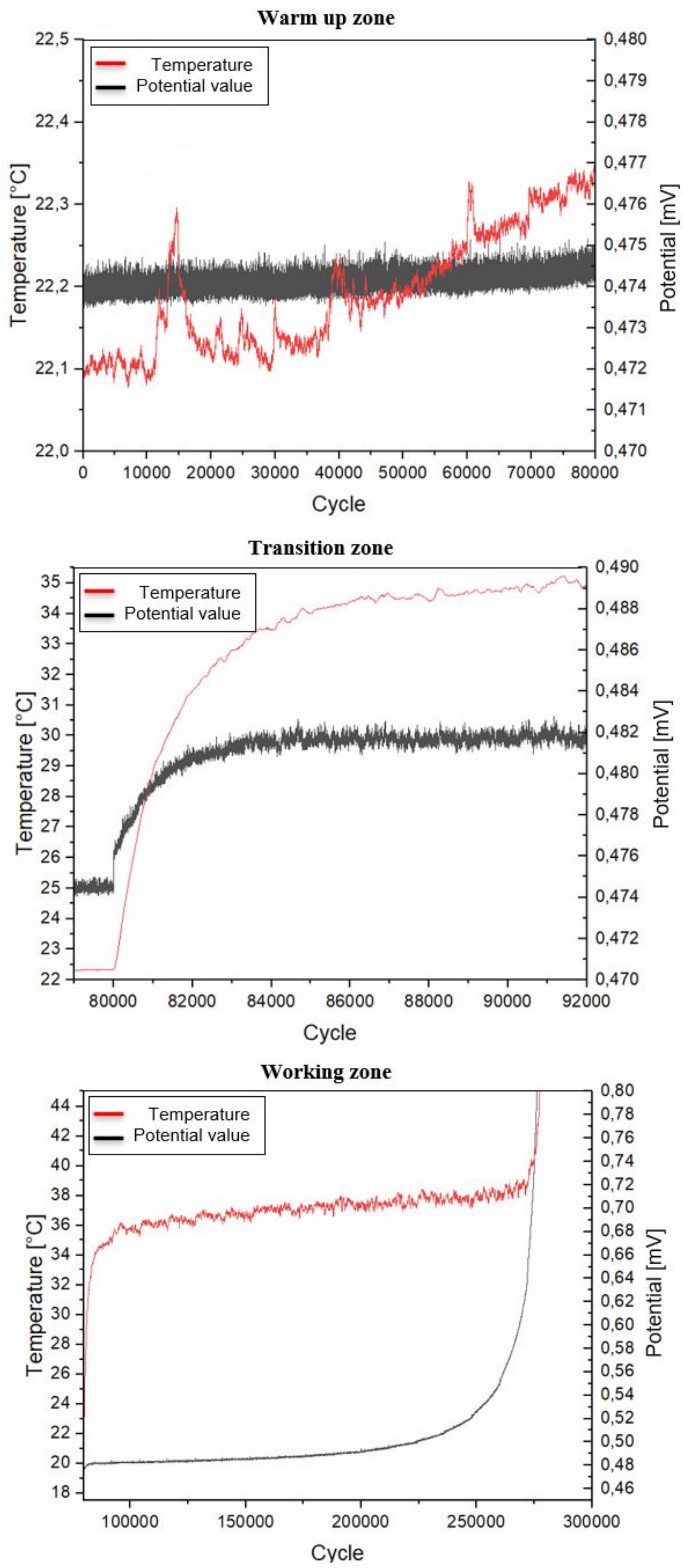

Figure 4.2: Areas of the Temperature graph

zone and the operational zone (from 23.3°C to 35°C), displaying a step-like pattern on the chart. Subsequently, during the operational phase, the temperature exhibited a linear increase, reaching approximately 37°C.
The second graph clearly shows how the considerable temperature variation impacted the potential value. As a result, the potential value underwent a transition from 0.474 mV to 0.482 mV.

4.2 Experimental results

This section focuses on presenting the results obtained through the application of the DCPD technique. Firstly, we present the results obtained from both the application of the analytical method and the finite element simulations.

4.2.1 Potentials graphs measurements

All the graphs presented in this section refer to the signals recorded by the DOLI EDC580V equipment. Specifically, the x-axis represents the cycle number, while the y-axis represents the potential value at the overload.

Distance of welding spot $2Y_0$=65mm

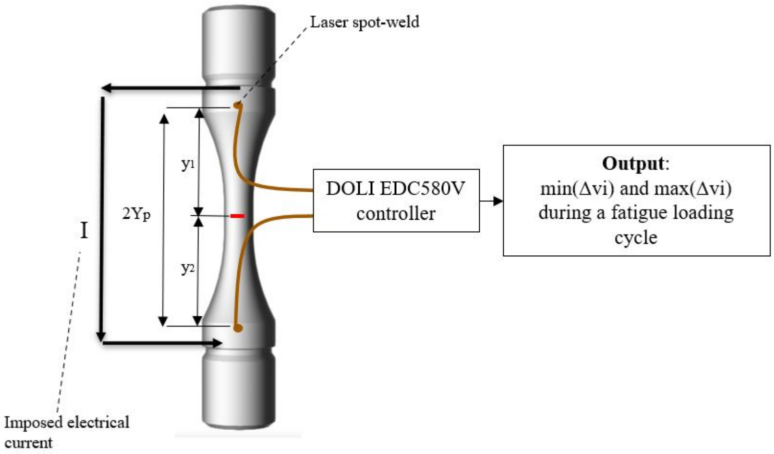

Figure 4.3: Specimen configuration

A total of five specimens were subjected to testing using this configuration (Figure 4.3), with variations in the meridian and axial positions of the secondary notch. Despite these variations, the graphs depicting the relative potentials exhibit a similar trend—specifically, there is no noticeable difference observed between the ΔV_1, ΔV_2 and ΔV_3 values across all tested specimens (Figure 4.7). Owing to the distance between the potential probes, the DCPD method proves incapable of detecting the presence of a propagating crack within the specimen. This limitation is evident in the graphs presented in the figure. Consequently, this outcome prompted a modification in the configuration of subsequent test specimens, with a focus on evaluating distances between soldering points that are less than or equal to 10mm.

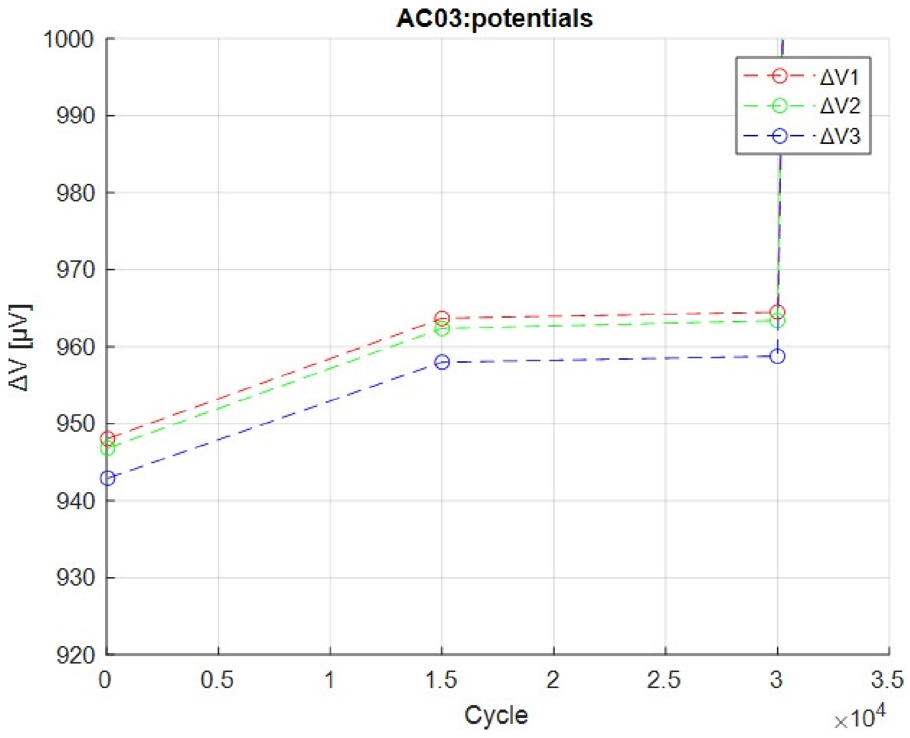

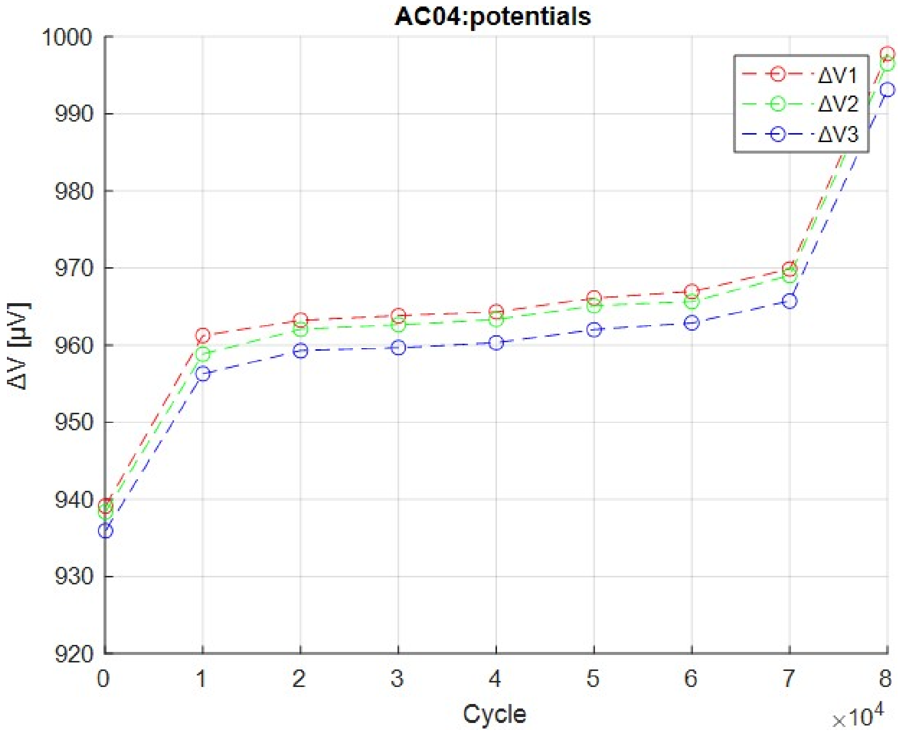

Figure 4.4: Potential graphs: $2Y_0$=65mm Specimen Code AC04

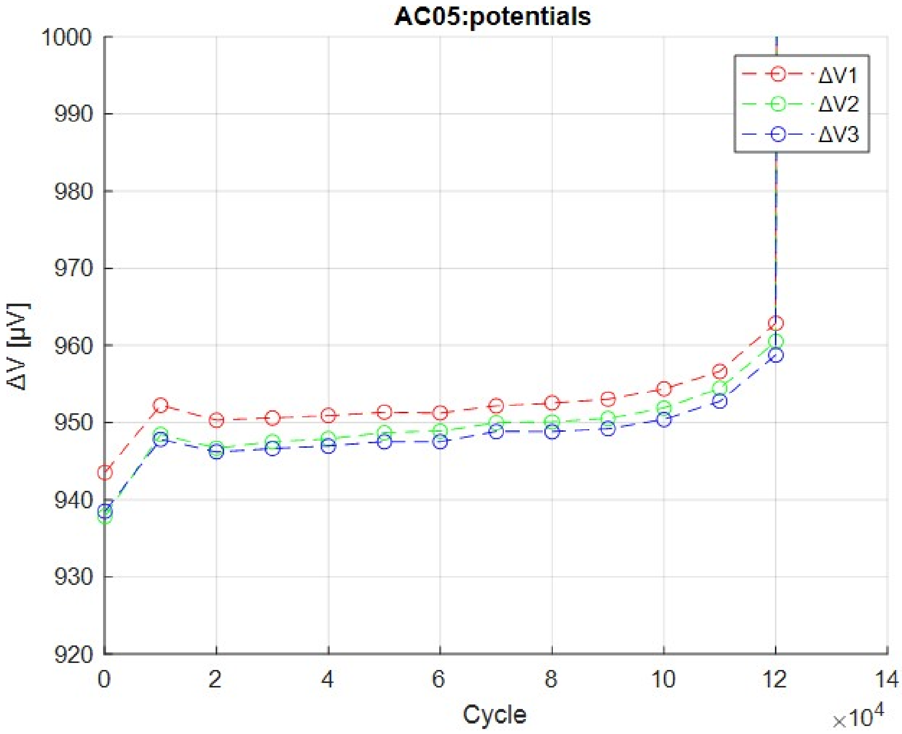

Figure 4.5: Potential graphs: $2Y_0$=65mm Specimen Code AC05

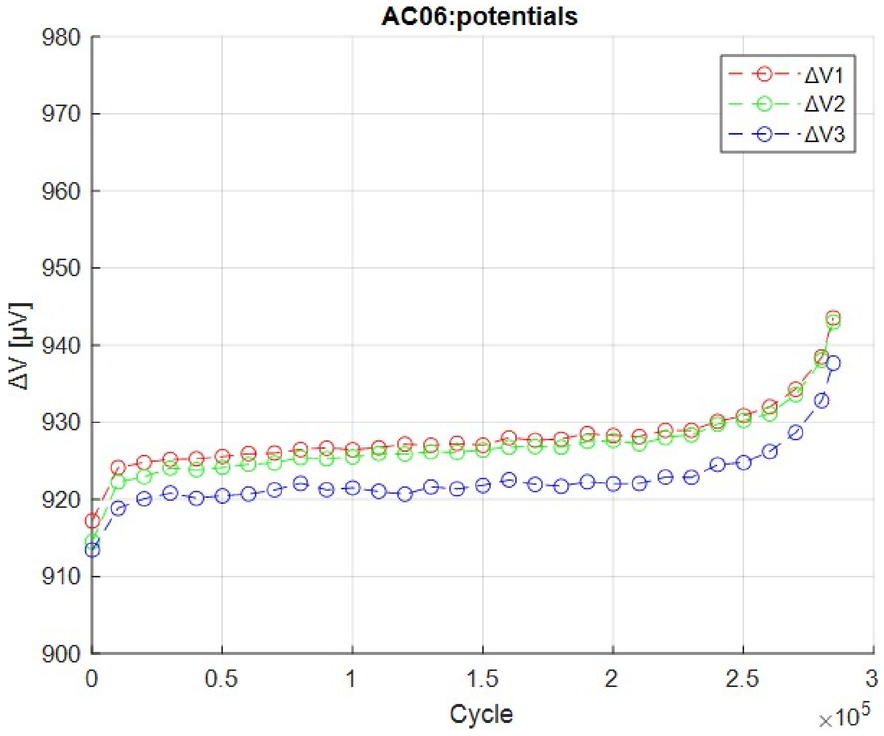

Figure 4.6: Potential graphs: $2Y_0$=65mm Specimen Code AC06

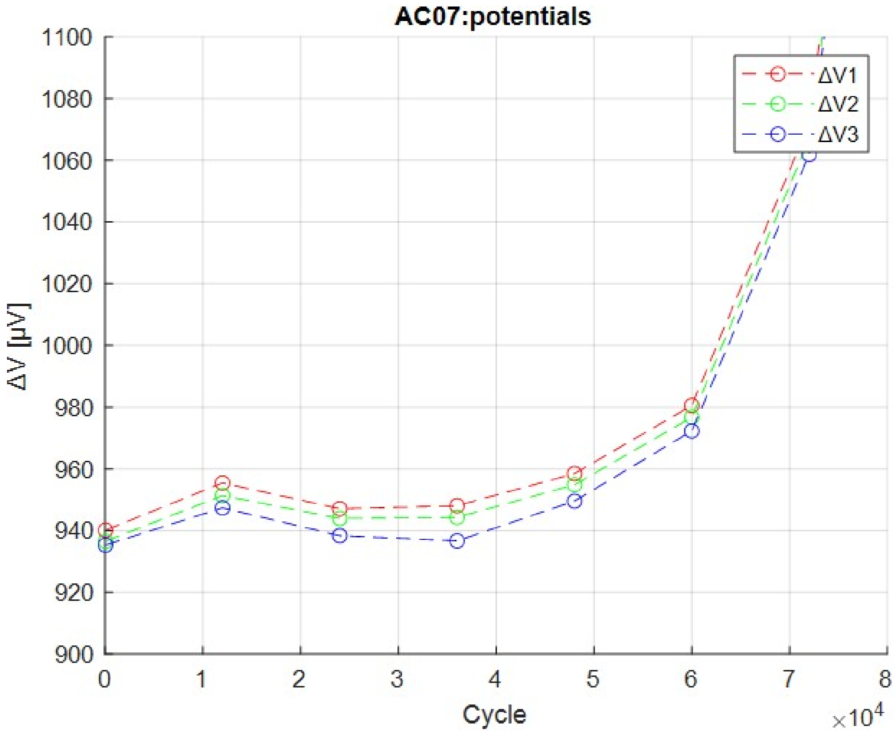

Figure 4.7: Potential graphs: $2Y_0$=65mm Specimen Code AC07

Distance of welding spot $2Y_0$=10mm

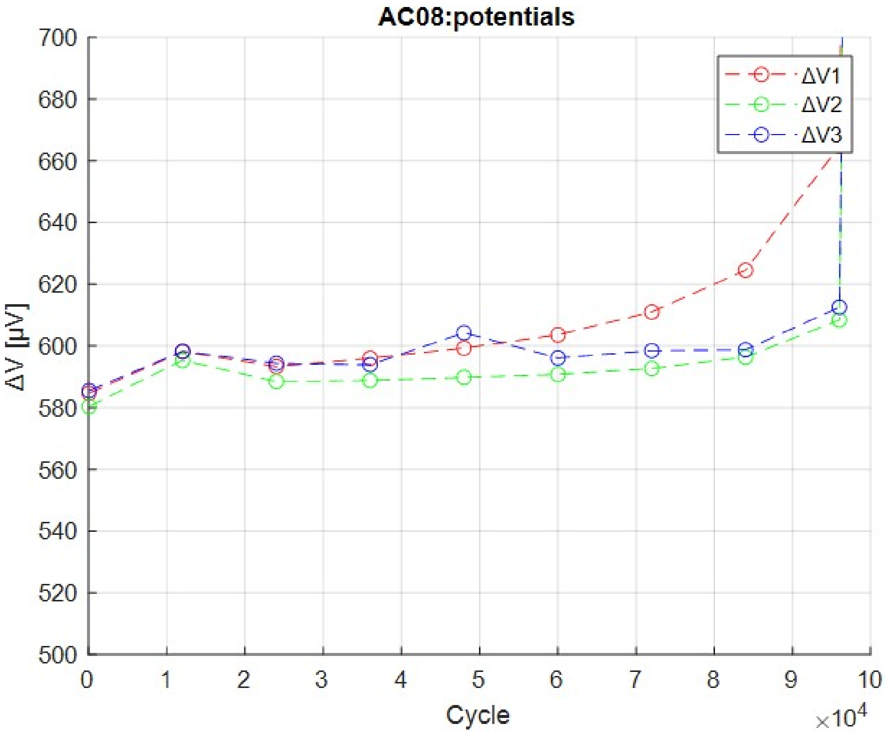

Figure 4.8: Potential graphs: $2Y_0$=10mm Specimen Code AC08

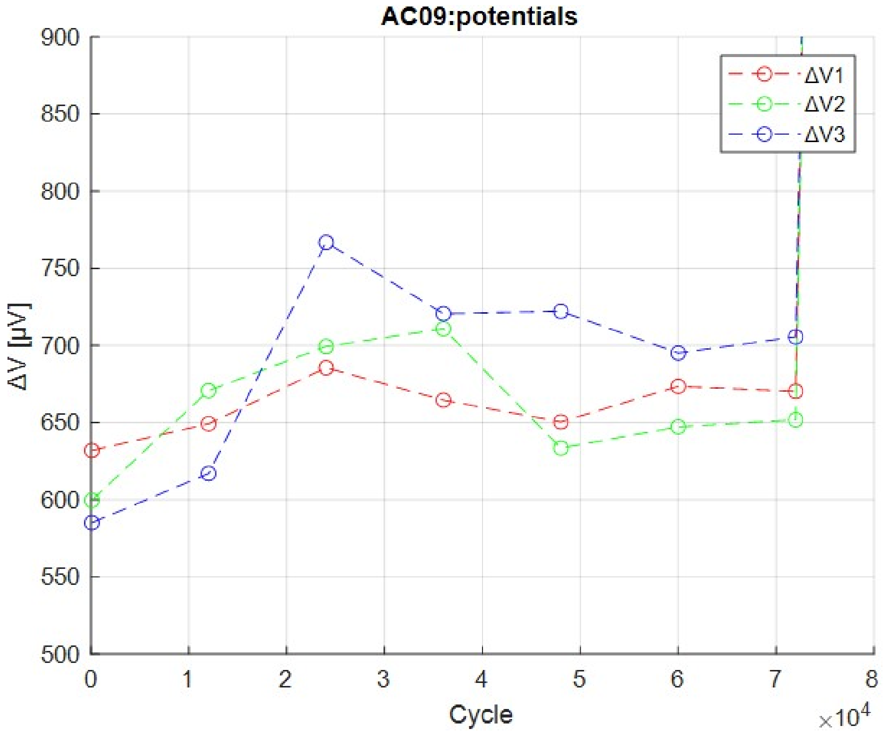

Figure 4.9: Potential graphs: $2Y_0$=10mm Specimen Code AC09

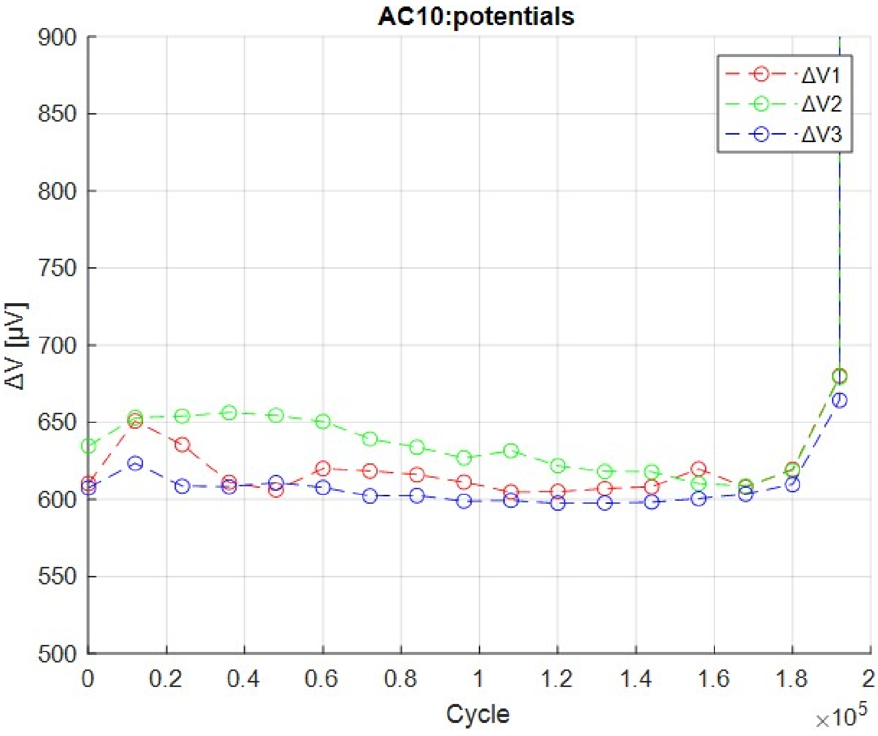

Figure 4.10: Potential graphs: $2Y_0$=10mm Specimen Code AC10

The precise positioning of the copper cables on the specimen surface demands meticulous attention. As depicted in the figure (4.11), when examining the graphs illustrating the measured potentials of test specimens AC09 and AC10, it becomes evident that the trend undergoes abrupt changes during the test. This observation leads us to realize that there were inaccuracies in the connection of the probes, emphasizing the criticality of ensuring correct connections.

One plausible explanation for this observed trend could lie in the manner in which the cable is secured. As a precaution to prevent the soldering point from breaking, tape was applied to secure the wire. However, this procedure likely introduces secondary contacts between the copper wire and the specimen surface, potentially leading to inaccuracies in the recorded potential values.

In contrast, the AC08 test exhibited the anticipated trend, demonstrating a notable increase in the potential value ΔV_1, aligning with the presence of a propagating crack at probe number 1. Both analytical and numerical finite element analyses are therefore possible with this specimen.

Distance of welding spot $2Y_0$=4mm

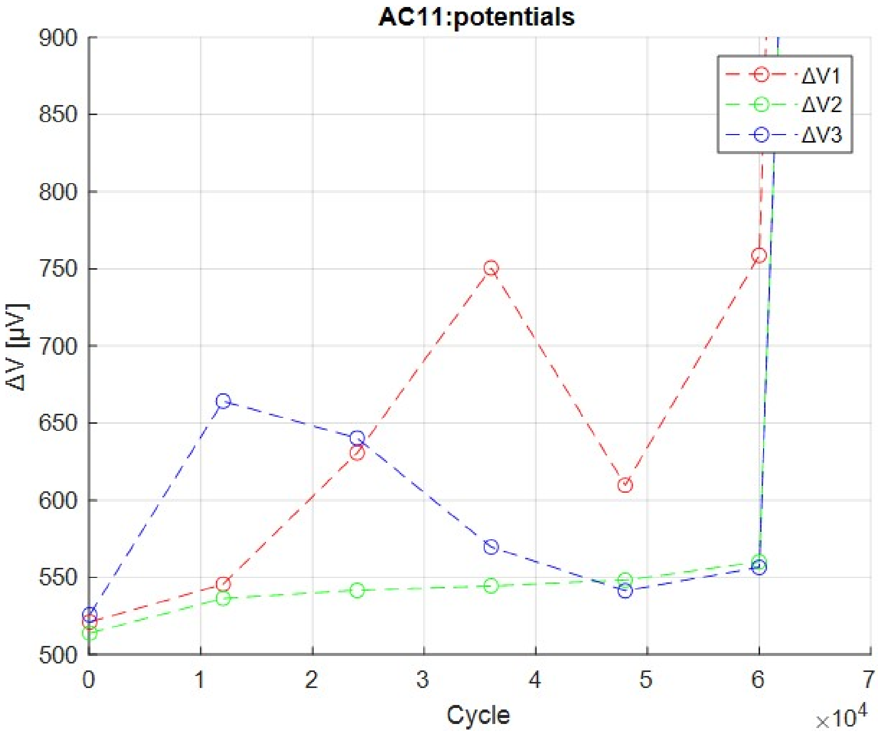

Figure 4.11: Potential graphs: $2Y_0$=4mm Specimen Code: AC11

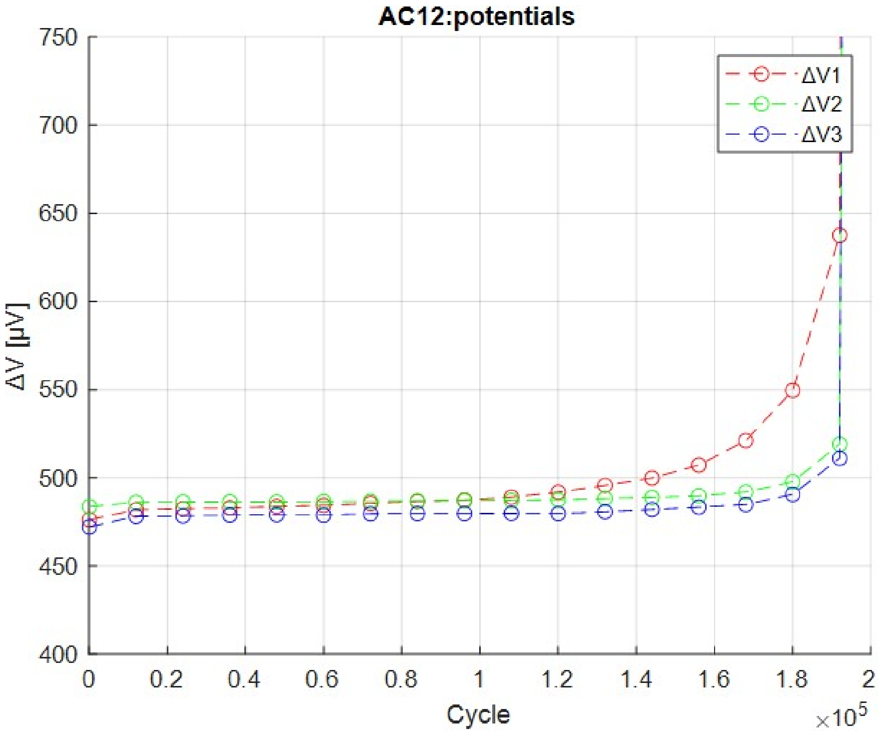

Figure 4.12: Potential graphs: $2Y_0$=4mm Specimen Code: AC12

Further reducing the distance between the welding spots leads to an even greater enhancement in the resolution of the DCPD method. After resolving additional positioning issues, Figure 4.12 illustrates the trend of clean, linear potentials. Notably, there is a noticeable increase in the recorded potential at probe one when a propagating crack is detected at that specific point.

4.2.2 Analysis of crack location by means of the Vector Model

Below, we present the results obtained from applying the method explained in the previous chapter, focusing on the evaluation of crack position. The graphs showcased are specific to specimens AC08 and AC12, providing insightful visual representations.

Specimen Code: AC08

In this particular specimen, configured with three potential probes spaced $2Y_0$=10mm apart, and a propagating crack at potential probe number 1, we calculated the angle using the vector model and compared it with the experimental results.

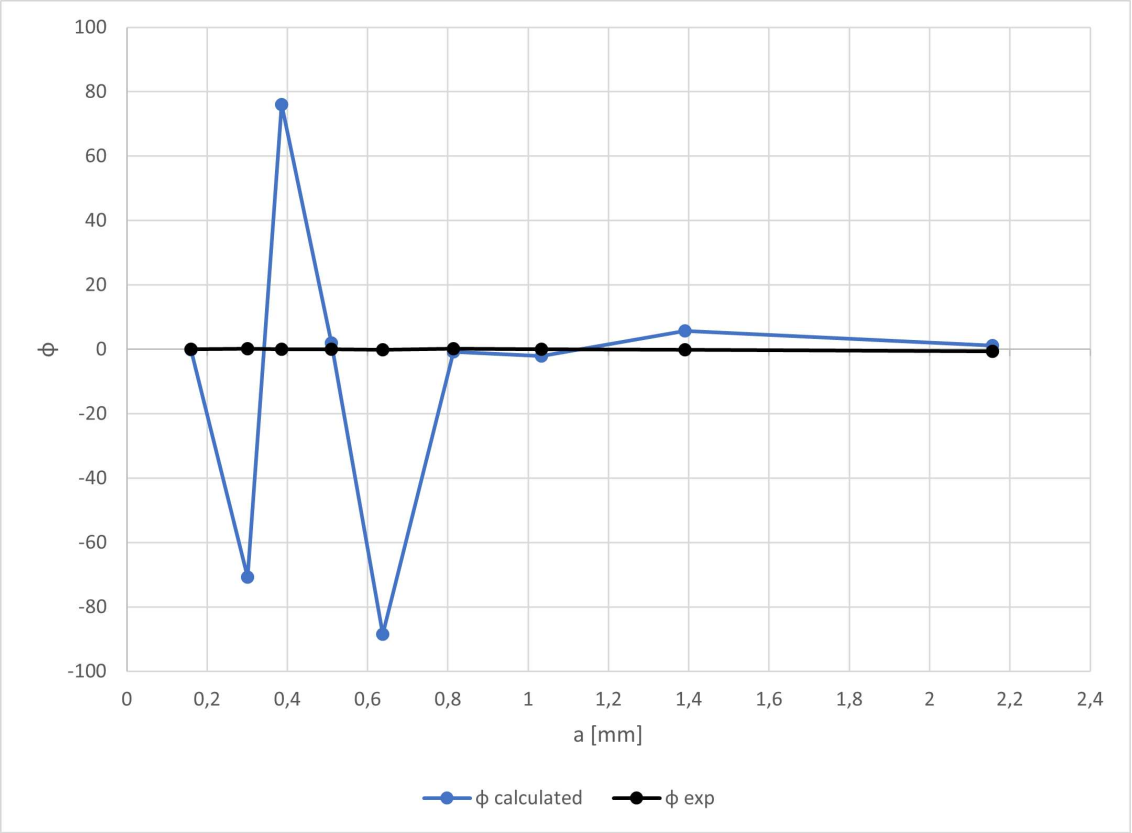

Figure 4.13: Experimental vs Calculated crack angle position, AC08

The graph illustrates that as the crack size increases, the calculated angle approaches and converges with the true experimental angle. Accurate estimates of crack position are achieved for values of 'a' approximately greater than 0.8-0.9 mm.

Specimen Code: AC12

Similar results were also obtained with this specimen always having a 3-potential probe configuration but with 4mm spacing and crack propagating always at probe number 1. In this case, there is a deviation from the experimental angle of 15° when the crack size is 0.9mm and as a increases, the calculated angle converges (figure 4.14).

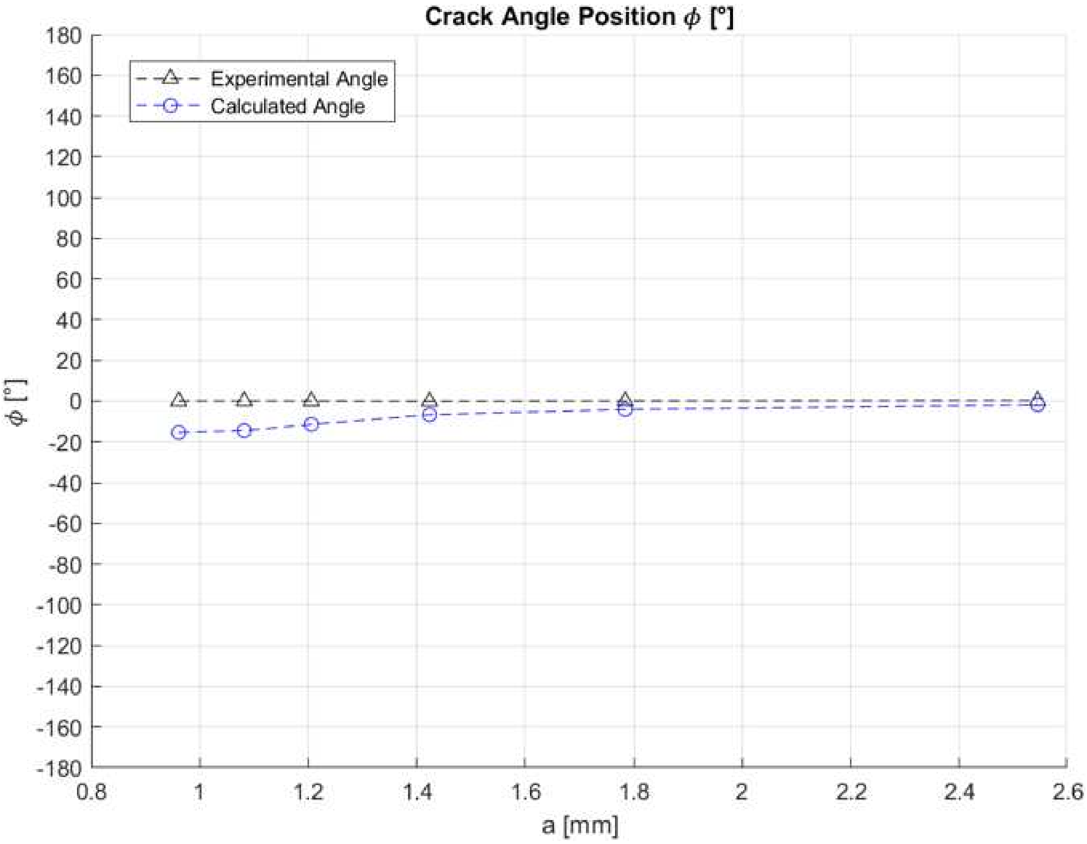

Figure 4.14: Experimental vs Calculated crack angle position, AC12

4.2.3 Analytical calibration curves

The calibration curves were obtained by fitting the following equations to the experimental points obtained.

$$\frac{a}{r} = \frac{2}{\pi} \cdot \arccos\left\{ \frac{\cosh\left(\frac{\pi \cdot y_0}{2 \cdot r}\right)}{\cosh\left[(N+1) \cdot \operatorname{arcosh}\left(\frac{\cosh\left(\frac{\pi y_0}{2r}\right)}{\cos\left(\frac{\pi a_{f,k}}{2r}\right)}\right)\right]} \right\} \tag{4.1}$$

$$\frac{a}{r} = q \cdot (N)^t + \frac{a_{f,k}}{r} \tag{4.2}$$

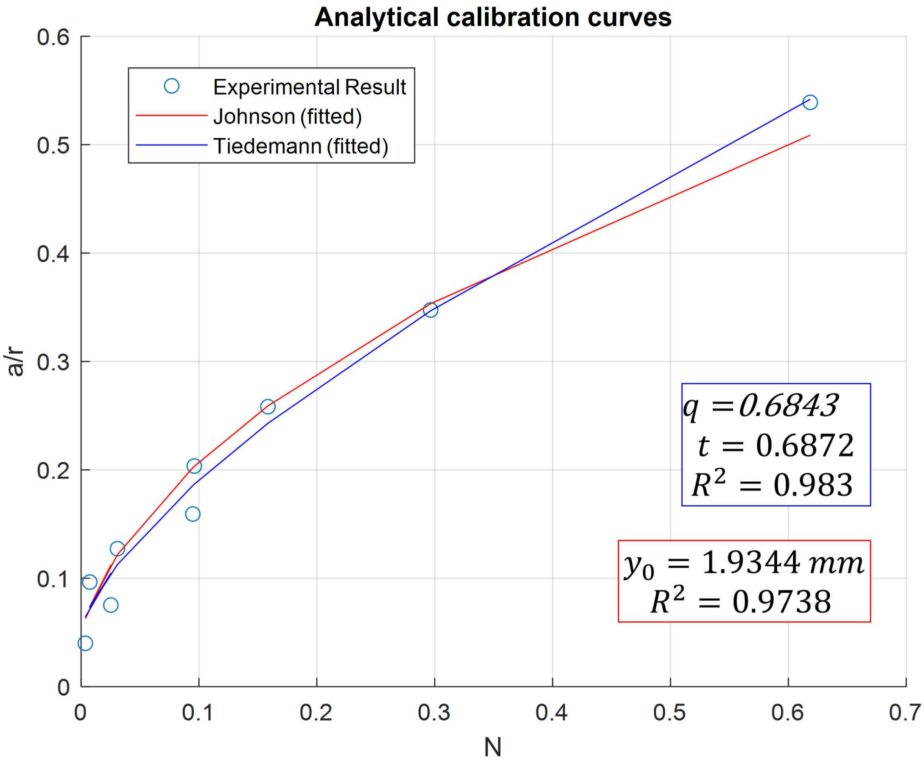

Figure 4.15: Johnson and Tiedemann Formula fitted. Specimen:AC08

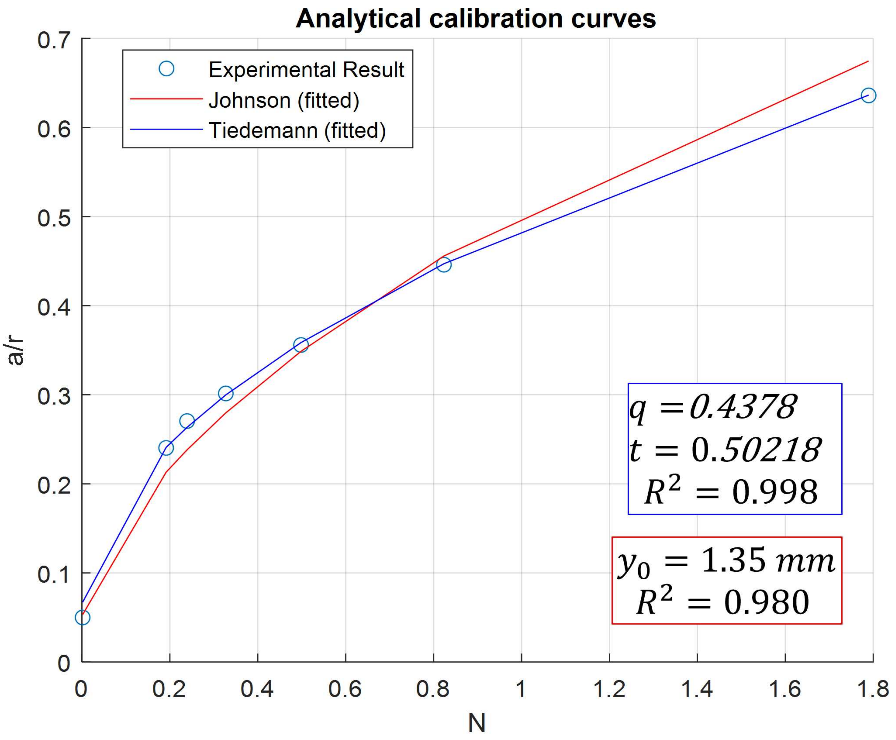

Figure 4.16: Johnson and Tiedemann Formula fitted. Specimen:AC12

4.2.4 FE Calibration curves

The result of the electrical analysis conducted in ANSYS using 10-node tetrahedral elements (solid 232) is depicted in the graph presented in the figure 4.18. It is evident that as the angular distance increases, the sensitivity of the method decreases. Conversely, with an increase in the shape ratio 'c/a,' the sensitivity tends to rise. The graph illustrates the potential measurements taken at a distance 'y_0' of 2 mm with angular positions of 0°, 60°, 120°, and 180°, respectively.

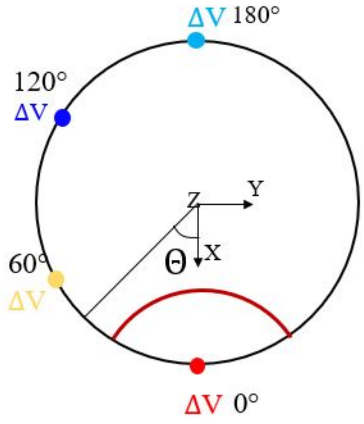

Figure 4.17: FE configuration

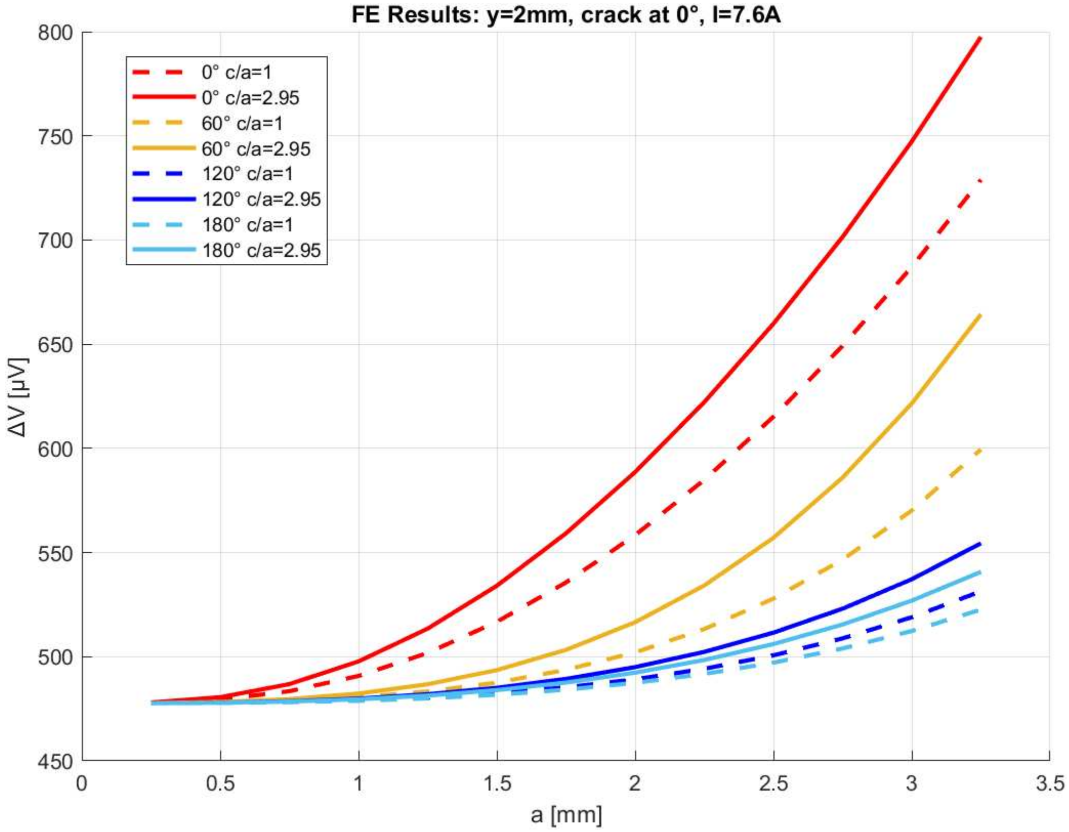

Figure 4.18: FE Calibration curves: y=2mm

When we adjust the analysis parameters and set the distance to y=5mm from the crack surface, Figure 4.19 reveals a noticeable decrease in the sensitivity of the method. The curves tend to converge, and in the most extreme case of y=32mm, they completely overlap. This observation underscores the strong influence of reading distance on PDM methods. To obtain meaningful and accurate results, it becomes apparent that the reading distance should be no less than 5mm.

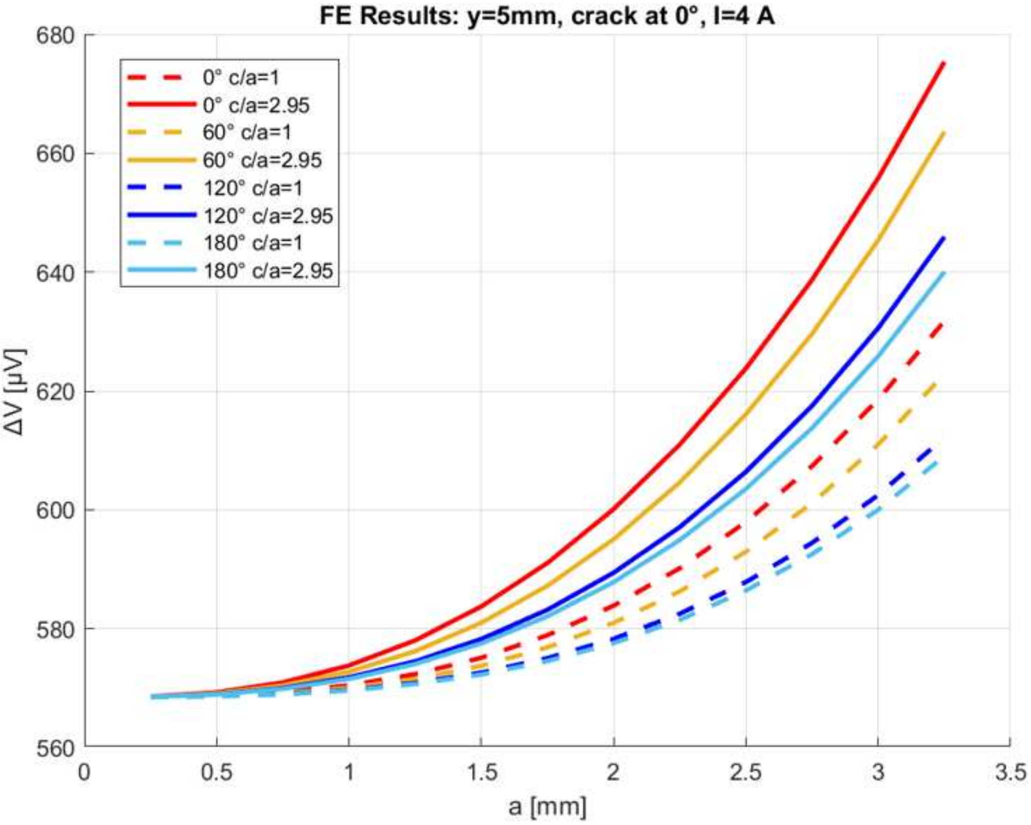

Figure 4.19: FE Calibration curves: y=5mm

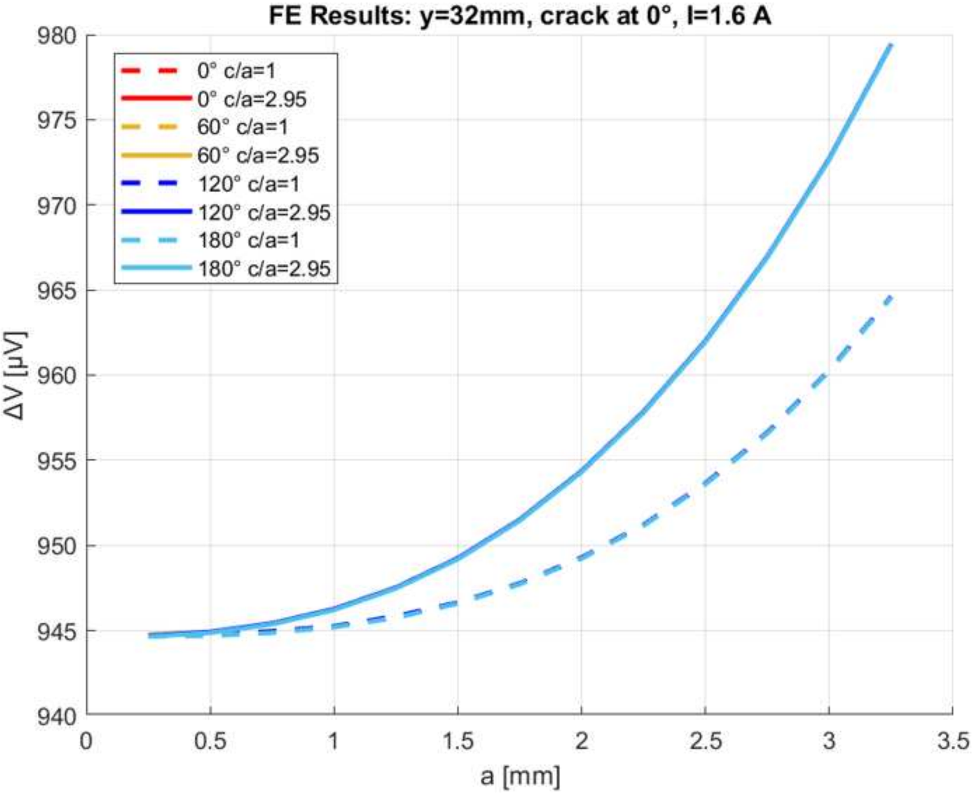

Figure 4.20: FE Calibration curves: y=32mm

Influence of y_0 to PDM sensitivity

The following graph shows the development of the potential as a function of distance y_0, considering a crack propagating at the potential probe. For simplicity, a constant c/a ratio of 1.23 has been considered in this example, while the crack depth varies from 0.2 to 3.5.

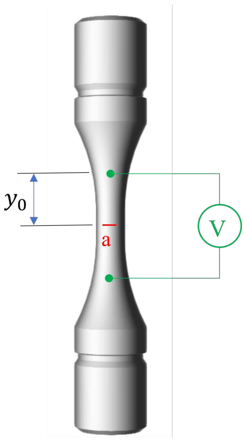

Figure 4.21: y_0 distance between crack and welding spot

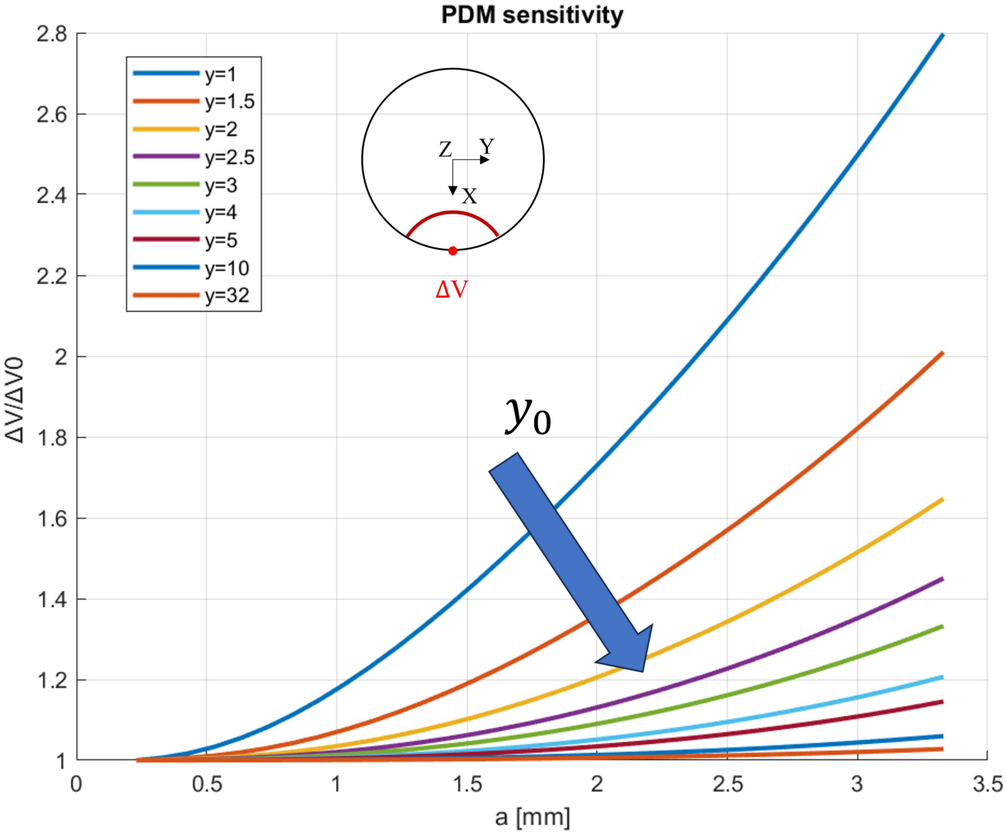

Figure 4.22: Relative Potential trend as function of a. Influence of y_0

Influence of Symmetric and Asymmetric configuration

This graph is intended to highlight the difference in potential readings between the symmetrical and asymmetrical configuration. In the graph, the dotted lines refer to the symmetrical configuration while the solid lines refer to the asymmetrical configuration. For the sake of simplicity, a constant c/a value of 1.23 has been considered while a varies from 0.2 to 3.5. The values chosen for the distance y0 refer to the experimental test set-up of specimen code AC08.

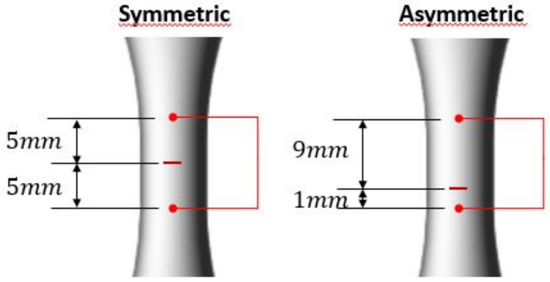

Figure 4.23: Symmetric and Asymmetric configuration

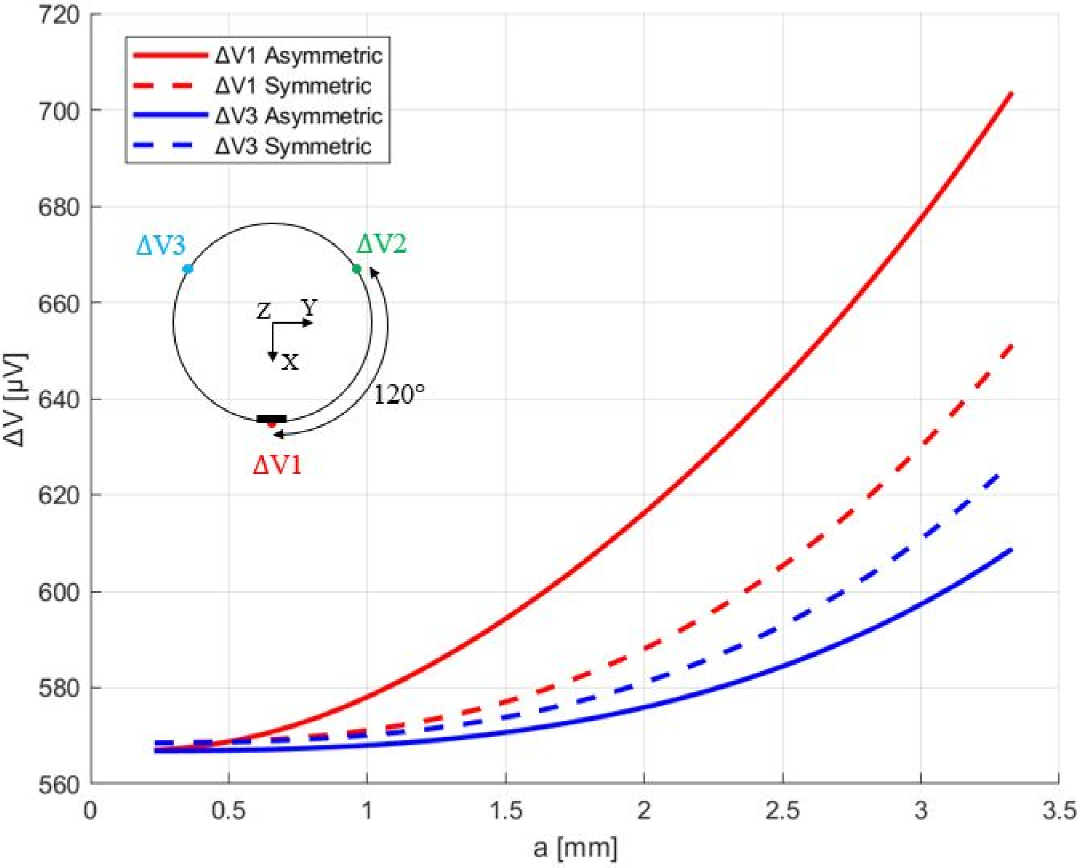

Figure 4.24: Potentials trend. Dotted lines for symmetrical, solid lines for asymmetrical.

Validation of FE calibration curves

These calibration curves were subsequently validated by comparison with experimental results and evaluating the percentage deviation.
To achieve this, the experimentally measured values were initially plotted in Figure 4.18 to assess whether they fell within the c/a value variation range. The results for test specimens AC08 and AC12 are illustrated in Figure .

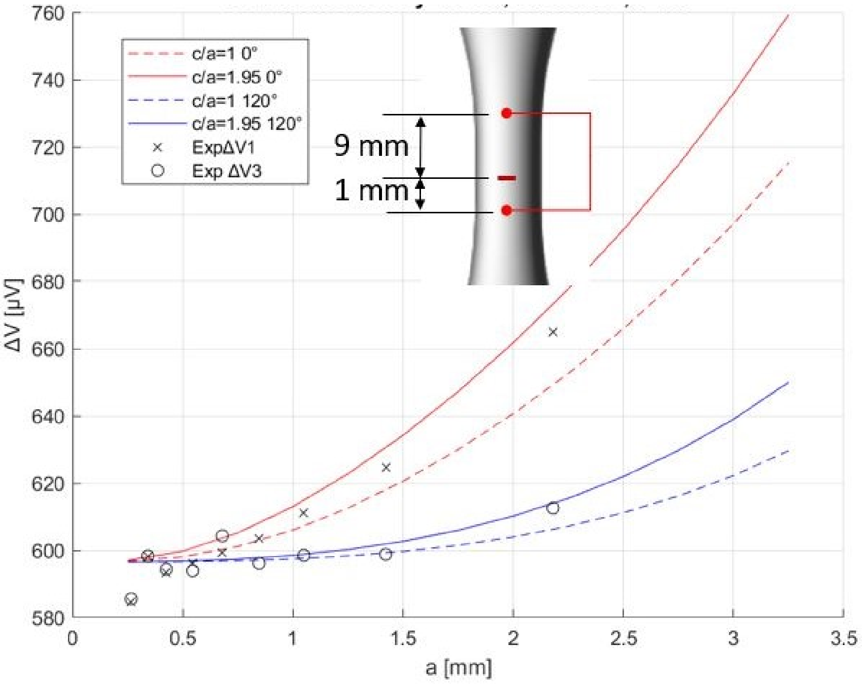

Figure 4.25: FE validation for specimen AC08

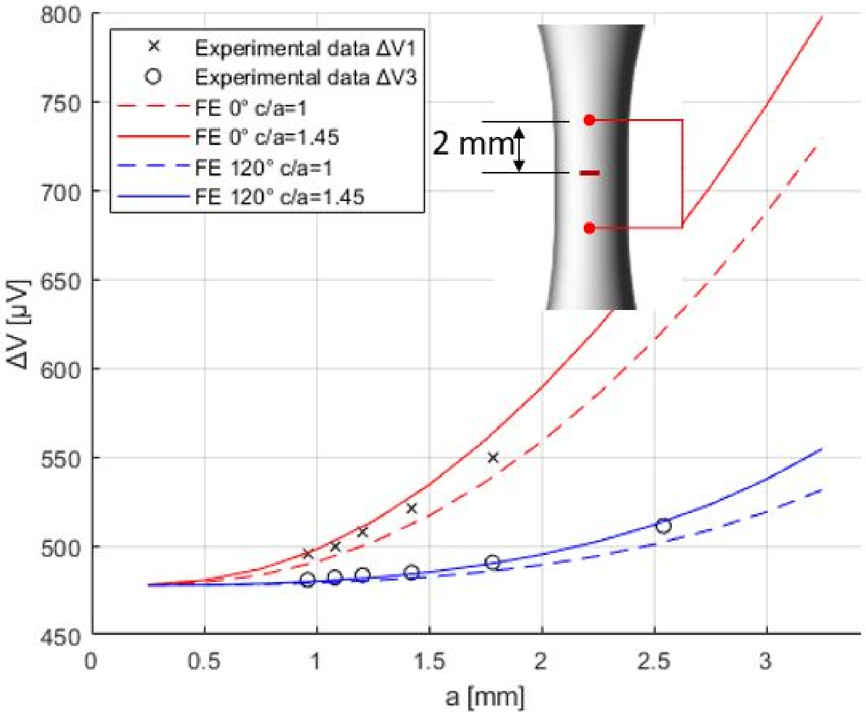

Figure 4.26: FE validation for specimen AC12

In the pursuit of more precise results, further FEM analyses were conducted. This involved configuring the experimentally measured values of 'a' and 'c/a' for an accurate comparison of deviations between experimentally measured values and those obtained through FEM simulations.

The following tables provide the experimental results for 'a' and 'c/a' concerning specimens AC08 and AC12.

AC08		
N° [#]	**a** [mm]	$\frac{c}{a}$ [-]
0	0.266	3.000
1	0.342	2.568
2	0.425	2.045
3	0.545	1.638
4	0.680	1.462
5	0.847	1.406
6	1.049	1.351
7	1.421	1.251
8	2.181	1.234

AC12		
N° [#]	**a** [mm]	$\frac{c}{a}$ [-]
0	0.256	3.000
11	0.961	1.257
12	1.082	1.251
13	1.206	1.277
14	1.424	1.276
15	1.784	1.263
16	2.544	1.265

After calculating the point values using FE analysis, the resistivity value for each specimen was calibrated using the first experimental data point. Subsequently, the percentage deviation between the experimentally measured values and the numerical values obtained from FEM analysis was calculated. In both cases, the deviation was found to be less than 1%.

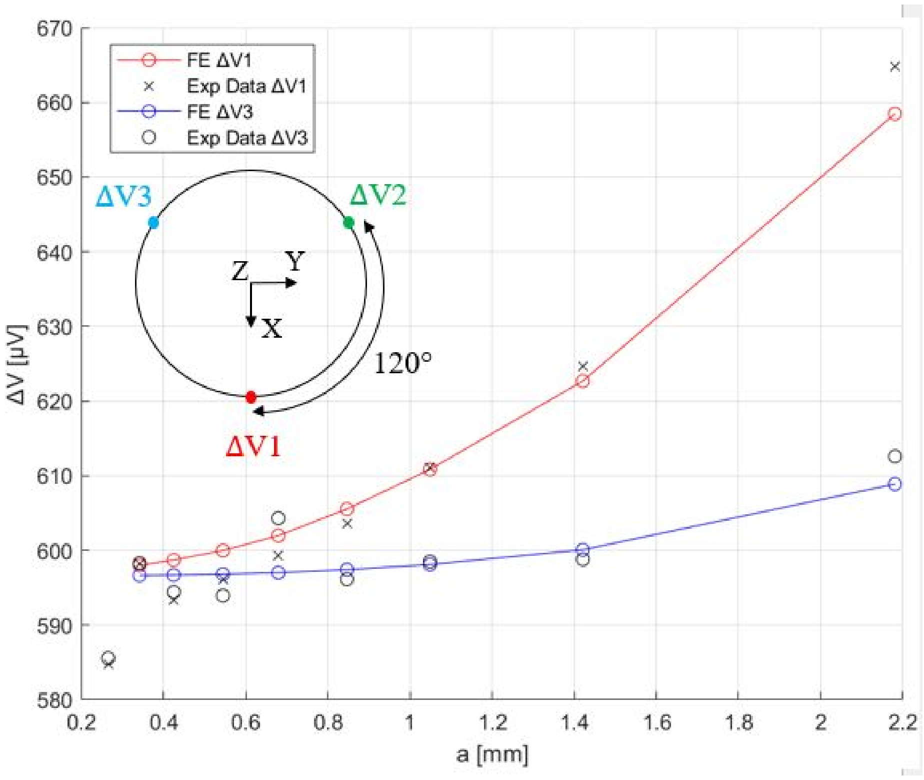

Figure 4.27: FE Validation: Specimen code AC08

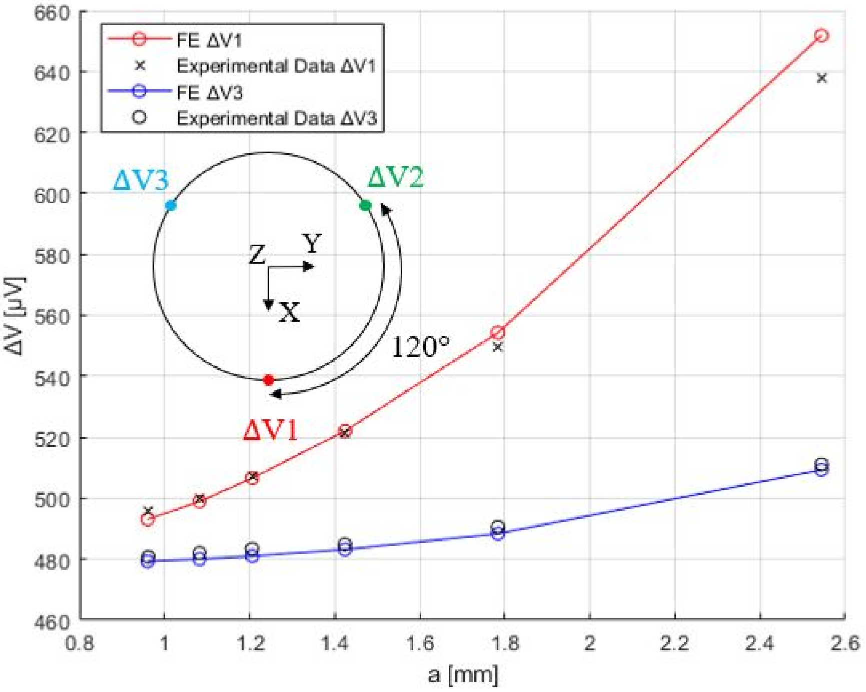

Figure 4.28: FE Validation: Specimen code AC12

4.2.5 Influence of load and welding spot

Thanks to the analyses performed in the ANSYS Workbench environment, we were able to achieve two significant objectives.

Firstly, we determined the influence of the load applied to the test specimen on the potential readout.

Secondly, we assessed how the potential varies within the molten copper ball on the surface of the test specimen.

The following table presents the results obtained from these analyses, which were carried out for two different crack sizes, allowing for a comparison with the values of specimen code AC12. The maximum and minimum potential measurements were recorded at the distances indicated in Figure 4.29, while Figure 4.31 displays the potential scale readings on the surface of the weld ball.

AC12									
c	a	F	KI min	KI max	ΔV_{max}	ΔV_{min}	$\Delta V_{avarage}$	ΔV_{exp}	ΔV_{APDL}
-	mm	kN	MPa$\sqrt{m}$	MPa$\sqrt{m}$	μV	μV	μV	μV	μV
1.21	0.96	12	309.4	325.1	501.4	489.9	496.2	495.7	494.9
3.2	2.54	12	618.8	745.2	658.9	654.4	655.0	637.6	654.1

Table 4.1: Static Structural & Electrical FEA results

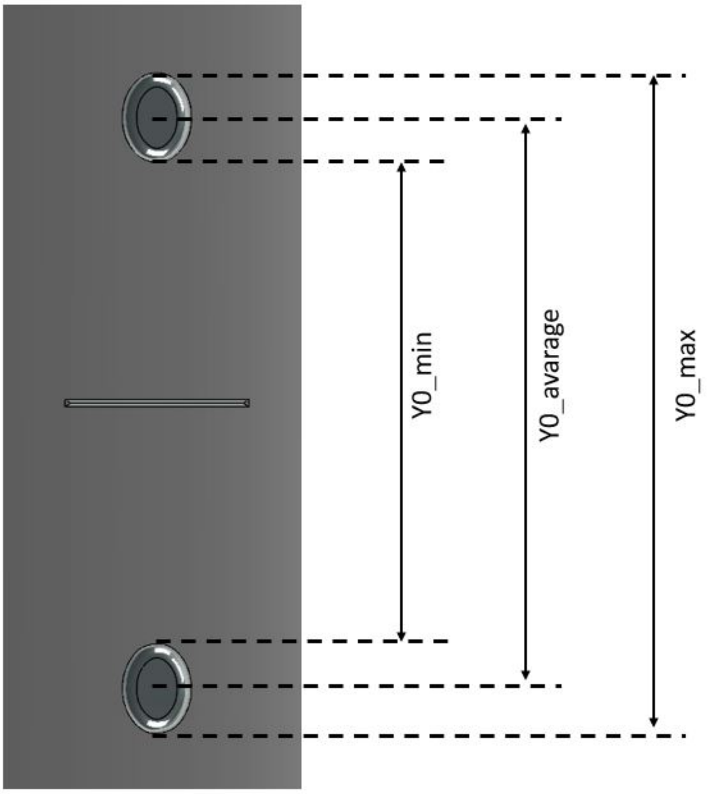

Figure 4.29: Measurement distance of potentials

The disparity between potential values measured at the most distant and closest points is minimal, resulting in a percentage deviation of approximately 1% between the two measurements. However, when compared to the average value of these measurements, it becomes evident that the applied load has no discernible influence on the potential readings.

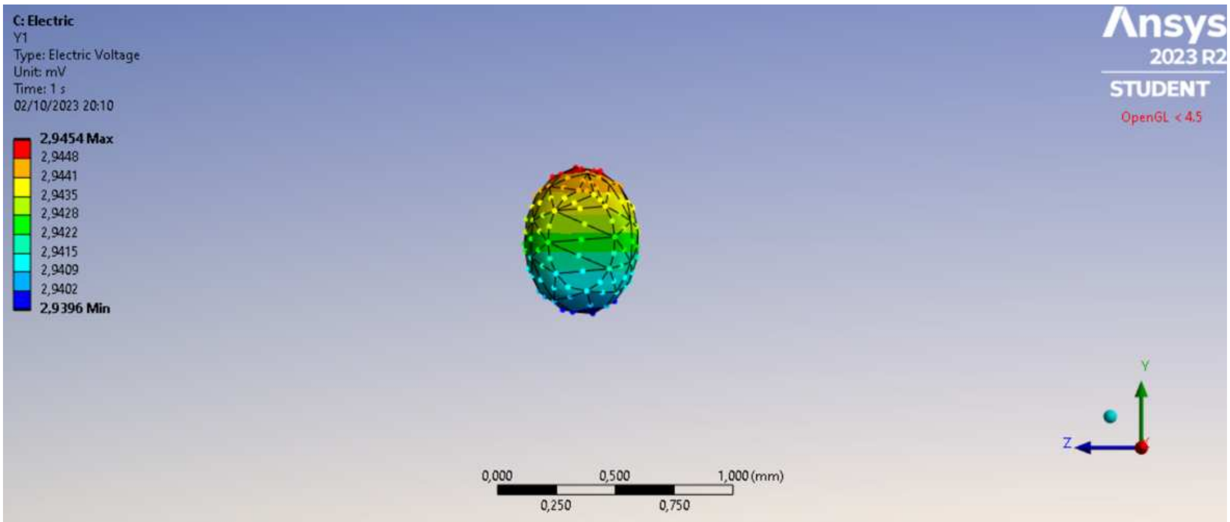

Figure 4.30: Potential scale readings on the surface of the weld ball

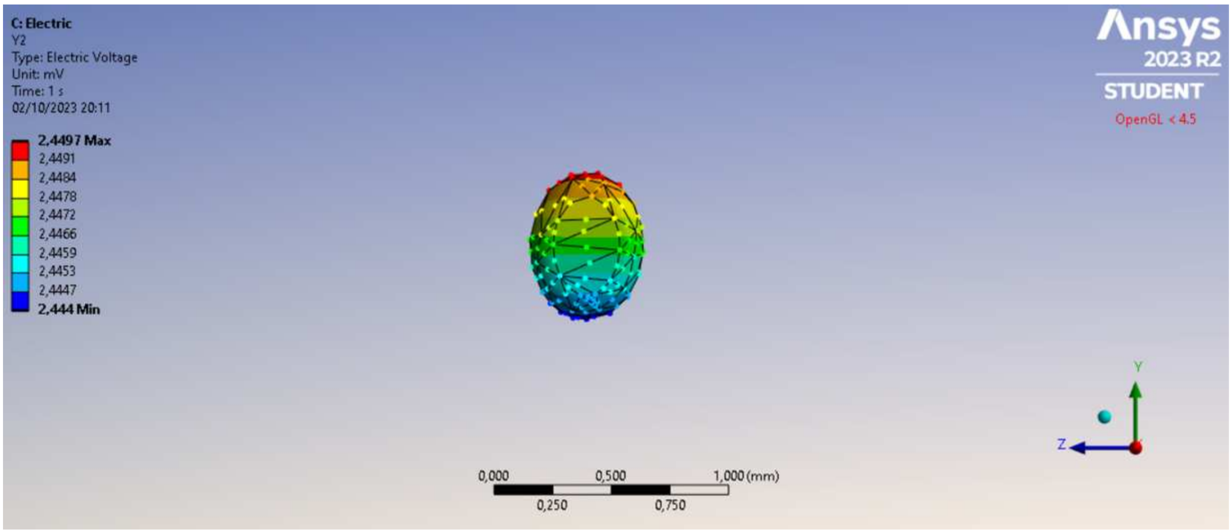

Figure 4.31: Potential scale readings on the surface of the weld ball

Chapter 5

Conclusion

In the present research, a three-probe potential drop method (PDM) was employed to estimate crack area, location, and configuration along semi-elliptical crack paths within round bars subjected to fatigue testing. The calibration of the chosen PDM configuration was obtained through two primary methods: the utilization of 3-dimensional electrical finite element (FE) models, representing single-edge round bars adopted in the experimental tests, and analytical calibration employing the Johnson and Tiedemann formula. Additionally, the technique for estimating the crack position was employed and rigorously tested on the specimen geometries.

The analysis encompassed a range of semi-elliptical surface cracks, involving variations in aspect ratios (c/a) within the range of 1 to 3, angular positions (Θ) spanning from 0° to 180° with respect to one potential probe, and crack depths (a) between 0.2 mm to 3 mm. Numerous configurations of the DCPD parameter and setup were also investigated to comprehensively assess their performance.

The following conclusions can be drawn:

- **Optimal Multi-Probe Configuration:** The multi-probe configuration emerged as the optimal choice for determining the desired quantities, positioning, and aspect ratio estimation. Through a series of rigorous tests, the ideal setup for this specimen geometry was identified. The configuration's performance is notably influenced by the spacing between potential probes. However, this research successfully pinpointed an ideal setup that exhibited high sensitivity in detecting propagating cracks, with potential values remaining free from interference by secondary contacts.

- **Effective Crack Initiation Position Estimation:** The proposed method for estimating the crack initiation position demonstrated its effectiveness, particularly for cracks larger than approximately 0.8 mm. The method exhibited a maximum error of approximately 20°.
- **Calibration Using Johnson's and Tiedemann's Functions:** The utilization of Johnson's and Tiedemann's functions for constructing the calibration curves exhibited a favorable trend in agreement with the experimental results. In most cases, the coefficient of determination (R^2) exceeded 0.98, indicating strong alignment between the model and experimental observations.
- **Validation of Numerical Analyses:** The numerical analyses employed for calibration were rigorously validated by comparing the results with experimental data obtained through fatigue testing of the specimens under axial loading. Notably, a high level of agreement was achieved, with the deviation between experimentally measured crack depths and those estimated from calibration curves derived via dedicated FE analyses typically falling within the range of $\pm 2\%$.

In summary, this research underscores the effectiveness of the multi-probe PDM configuration for crack analysis and positioning. It also highlights the success of the proposed crack initiation position estimation method, the reliability of Johnson's and Tiedemann's functions for calibration, and the strong agreement between numerical analyses and experimental results. These findings contribute to the advancement of crack detection and characterization methods in structural integrity assessment.

Appendix A

Specimens details

A.1 Nomenclature

$D_{\mathbf{nett}}$	Nett section diameter	$D_{\mathbf{gross}}$	Gross section diameter
$L_{\mathbf{nett}}$	Nett section length	$L_{\mathbf{tot}}$	total length
$h_{\mathbf{notch}}$	Notch depth	$a_{\mathbf{notch}}$	Notch width
$2Y_{\mathbf{p}}$	Probe distance	$\frac{\boldsymbol{y_1}}{\boldsymbol{y_2}}$	pre crack centering parameter
N° probe	Probes number	θ_s	Probe spacing
θ_f	vertical probes alignement	θ_n	angle between pre-crack and probes U1
ΔF_b	Base Load Force	$\boldsymbol{f}$	frequency
ΔF_o	Over Load Force	$Cycle_{b,o}$	n° of cycle

Table A.1: Nomenclature

A.2 Probe grips distance: 65 mm

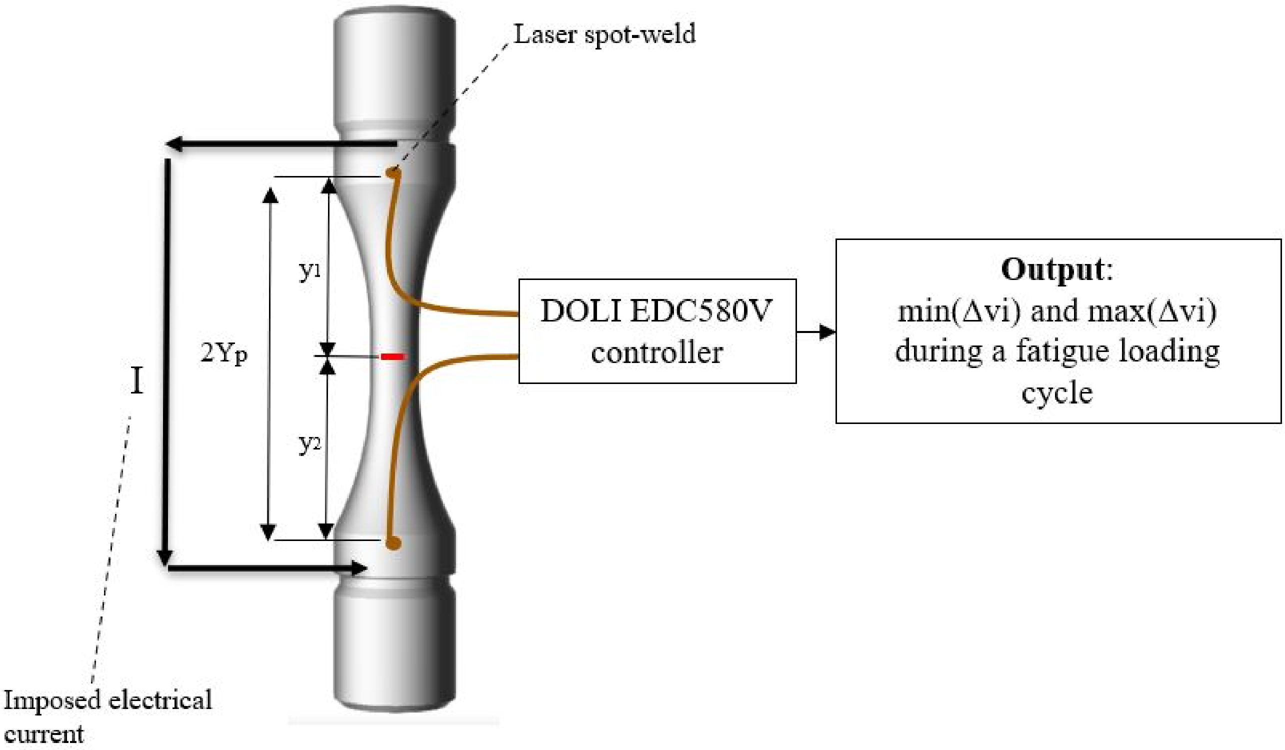

Figure A.1: Specimen configuration: y=32mm

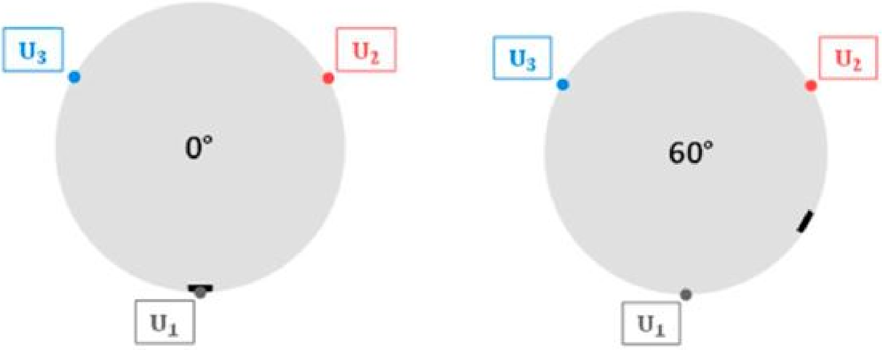

Figure A.2: secondary notch position

A.2.1 Specimens AC03

Specimens

Code	AC03	**Type**	Single-edge crack round bar
Test	DCPD	**Material**	AISI 304
Date	20.03.23	**Operator**	Codemo

Geometry

$D_{\mathbf{nett}}$	8 mm	$D_{\mathbf{gross}}$	20 mm
$L_{\mathbf{nett}}$	10 mm	$L_{\mathbf{tot}}$	64 mm
$h_{\mathbf{notch}}$	0.3 mm	$a_{\mathbf{notch}}$	1.3 mm
$2Y_{\mathbf{p}}$	65 mm	$\frac{\boldsymbol{y_1}}{\boldsymbol{y_2}}$	1 -
N° probe	3	θ_s	120°
θ_f	0°	θ_n	0°

Load

Type	Force control	**R**	-1
ΔF_b	12 KN	$\boldsymbol{f}$	20 Hz
ΔF_o	20 KN	$\boldsymbol{f}$	0.5 Hz
$Cycle_b$	14999	$Cycle_o$	1

DCPD

Device	DOLI EDC580V	**Current**	1.6 A
Mode	Free running	**Type**	Local current input
ρ	71.4 e-8 Ωm		

Results

N° [#]	**a** [mm]	$\frac{\boldsymbol{c}}{\boldsymbol{a}}$ [-]	θ [deg]	**Area** [mm^2]	**V1** [μV]	**V2** [μV]	**V3** [μV]
0	0.587	1.723	2.144	0.847	948.094	946.860	942.949
1	0.891	1.453	1.951	1.636	963.702	962.395	958.021
2	1.472	1.260	1.839	3.763	964.519	963.424	958.792

Photo

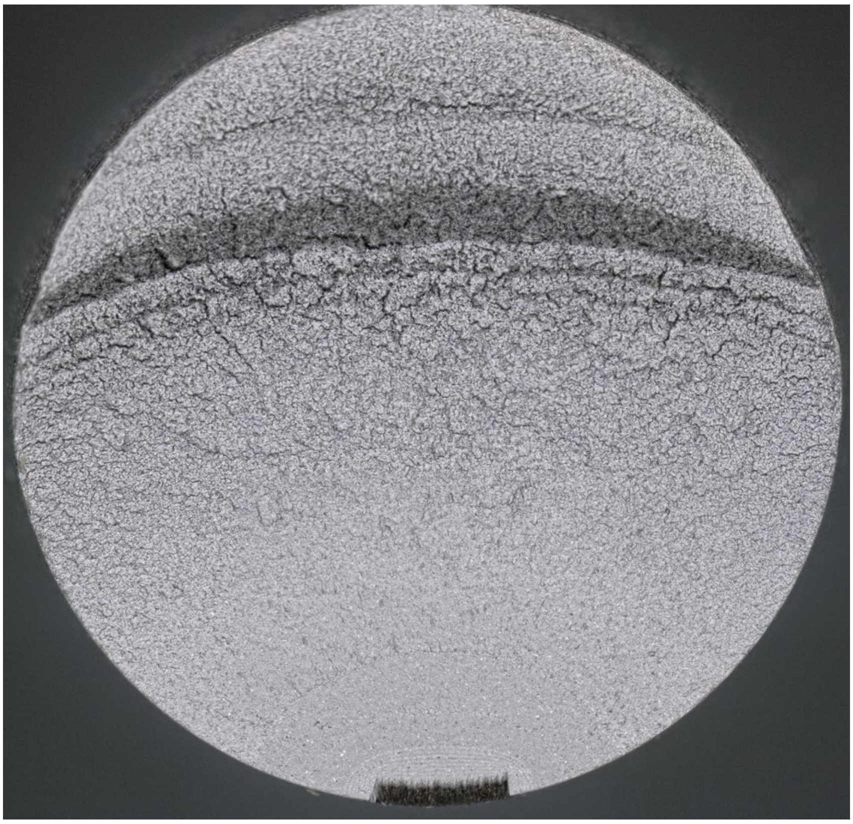

(a) crack surface magnification

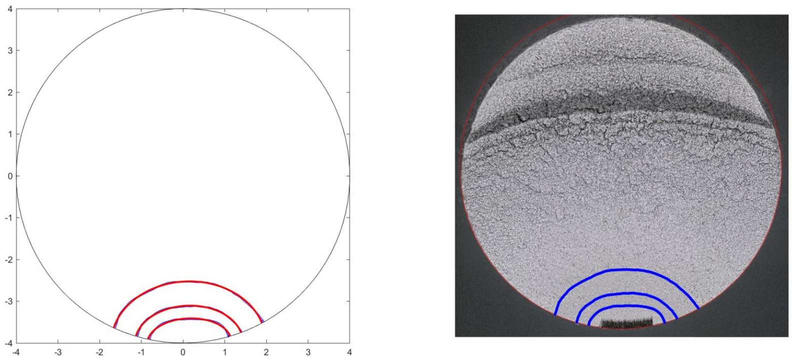

(b) fitted cracks

Figure A.3: AC03 specimen setup

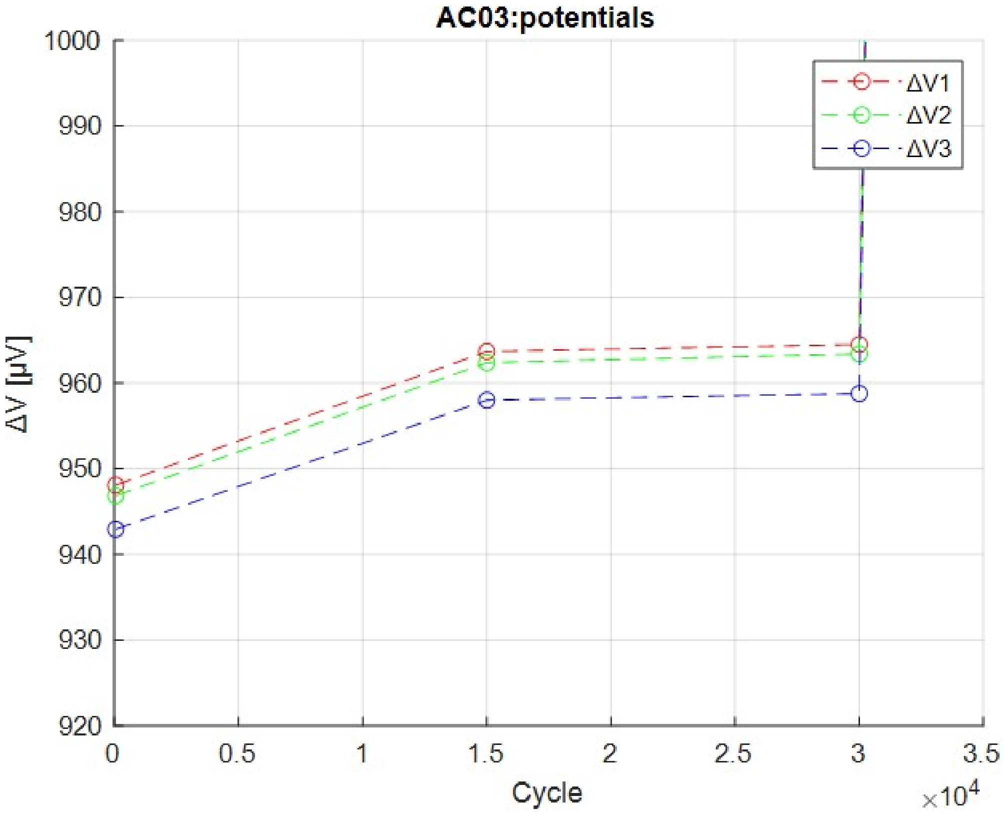

Figure A.4: Potential values AC03

A.2.2 Specimen AC04

Specimens

Code	AC04	**Type**	Single-edge crack round bar
Test	DCPD	**Material**	AISI 304
Date	24.03.23	**Operator**	Codemo

Geometry

$D_{\mathbf{nett}}$	8 mm	$D_{\mathbf{gross}}$	20 mm
$L_{\mathbf{nett}}$	10 mm	$L_{\mathbf{tot}}$	64 mm
$h_{\mathbf{notch}}$	0.3 mm	$a_{\mathbf{notch}}$	1.3 mm
$2Y_{\mathbf{p}}$	65 mm	$\frac{\boldsymbol{y_1}}{\boldsymbol{y_2}}$	1.28 -
N° probe	3	θ_s	120°
θ_f	0°	θ_n	0°

Load

Type	Force control	**R**	-1
ΔF_b	12 KN	$\boldsymbol{f}$	20 Hz
ΔF_o	20 KN	$\boldsymbol{f}$	0.5 Hz
$Cycle_b$	9999	$Cycle_o$	1

DCPD

Device	DOLI EDC580V	**Current**	1.6 A
Mode	Free running	**Type**	Local current input
ρ	71.4 e-8 Ωm		

Results

N°	**a**	$\frac{\boldsymbol{c}}{\boldsymbol{a}}$	θ	**Area**	**V1**	**V2**	**V3**
[#]	[mm]	[-]	[grad]	[mm^2]	[μV]	[μV]	[μV]
0	0.263	3.000	+0.000	0.286	939.166	938.416	935.957
1	0.385	2.353	-0.024	0.487	961.274	958.872	956.318
2	0.517	1.748	-0.212	0.672	963.257	962.090	959.306
3	0.633	1.556	-0.272	0.900	963.845	962.677	959.698
4	0.799	1.419	-0.037	1.300	964.345	963.353	960.343
5	0.984	1.355	-0.240	1.865	966.129	965.132	962.047
6	1.250	1.319	-0.199	2.866	966.984	965.670	962.911
7	1.674	1.305	-0.483	4.888	969.910	969.046	965.750
8	3.144	1.373	-1.515	15.120	997.800	996.556	993.147

Photo

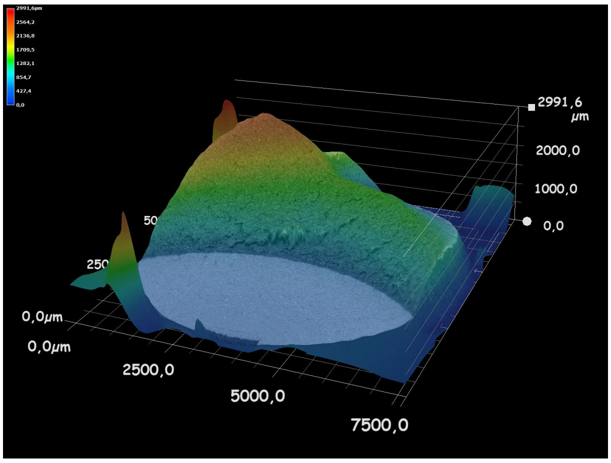

(a) 3D crack surface magnification

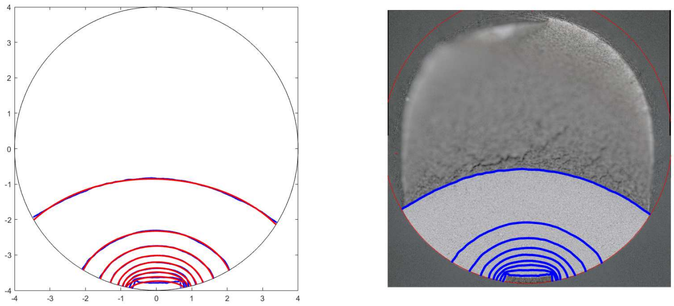

(b) fitted cracks

Figure A.5: AC04 specimen setup

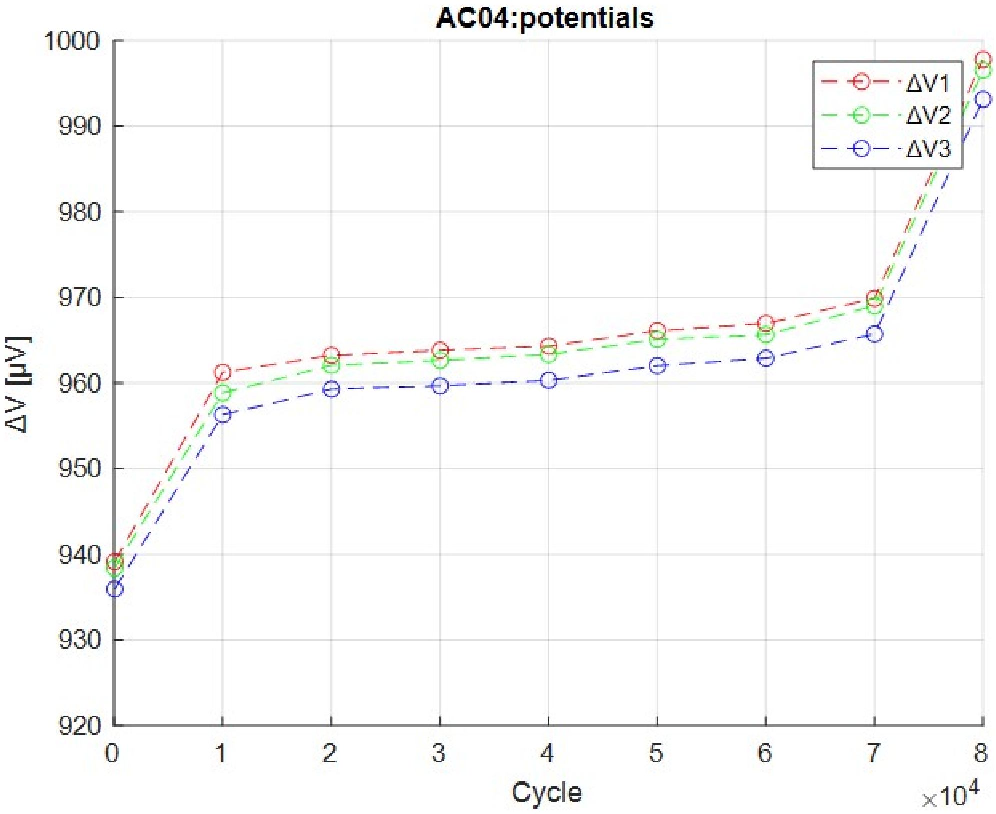

Figure A.6: Potentials valure AC04

A.2.3 AC05

Specimens

Code	AC05	**Type**	Single-edge crack round bar
Test	DCPD	**Material**	AISI 304
Date	28.03.23	**Operator**	Codemo

Geometry

$D_{\mathbf{nett}}$	8 mm	$D_{\mathbf{gross}}$	20 mm
$L_{\mathbf{nett}}$	10 mm	$L_{\mathbf{tot}}$	64 mm
$h_{\mathbf{notch}}$	0.3 mm	$a_{\mathbf{notch}}$	1.3 mm
$2Y_{\mathbf{p}}$	65 mm	$\frac{\boldsymbol{y_1}}{\boldsymbol{y_2}}$	1 -
N° probe	3	θ_s	120°
θ_f	0°	θ_n	60°

Load

Type	Force control	**R**	-1
ΔF_b	11 KN	$\boldsymbol{f}$	20 Hz
ΔF_o	19 KN	$\boldsymbol{f}$	0.5 Hz
$Cycle_b$	9999	$Cycle_o$	1

DCPD

Device	DOLI EDC580V	**Current**	1.6 A
Mode	Free running	**Type**	Local current input
ρ	71.4 e-8 Ωm		

Results

N° [#]	**a** [mm]	$\frac{c}{a}$ [-]	θ [grad]	**Area** [mm^2]	**V1** [μV]	**V2** [μV]	**V3** [μV]
0	0.231	4.000	+0.000	0.274	943.551	937.879	938.514
1	0.270	3.359	+0.417	0.324	952.268	948.504	947.839
2	0.329	2.628	+0.300	0.392	950.335	946.699	946.231
3	0.397	2.143	+0.124	0.479	950.623	947.530	946.656
4	0.468	1.838	+0.103	0.579	950.932	947.921	946.990
5	0.563	1.599	-0.026	0.734	951.372	948.715	947.540
6	0.661	1.458	+0.107	0.926	951.262	948.917	947.549
7	0.787	1.378	-0.001	1.233	952.191	950.008	948.865
8	0.903	1.361	+0.038	1.590	952.567	950.119	948.836
9	1.074	1.308	+0.024	2.141	953.065	950.548	949.240
10	1.298	1.283	-0.097	3.012	954.377	951.916	950.429
11	1.616	1.284	+0.088	4.531	956.663	954.461	952.795
12	2.199	1.304	+0.086	7.993	962.905	960.539	958.768

Photo

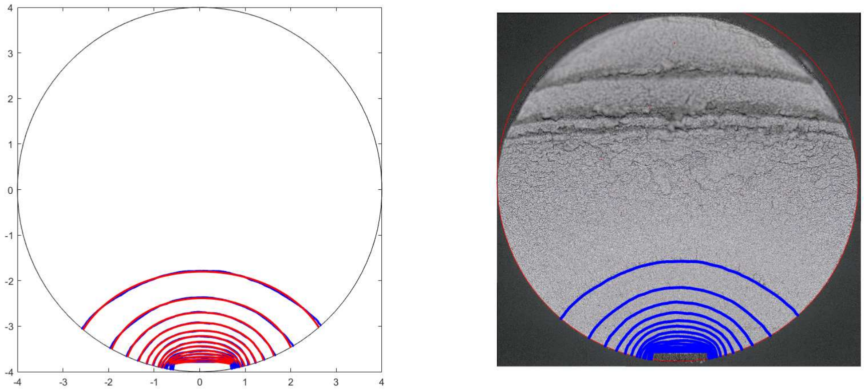

(a) fitted cracks

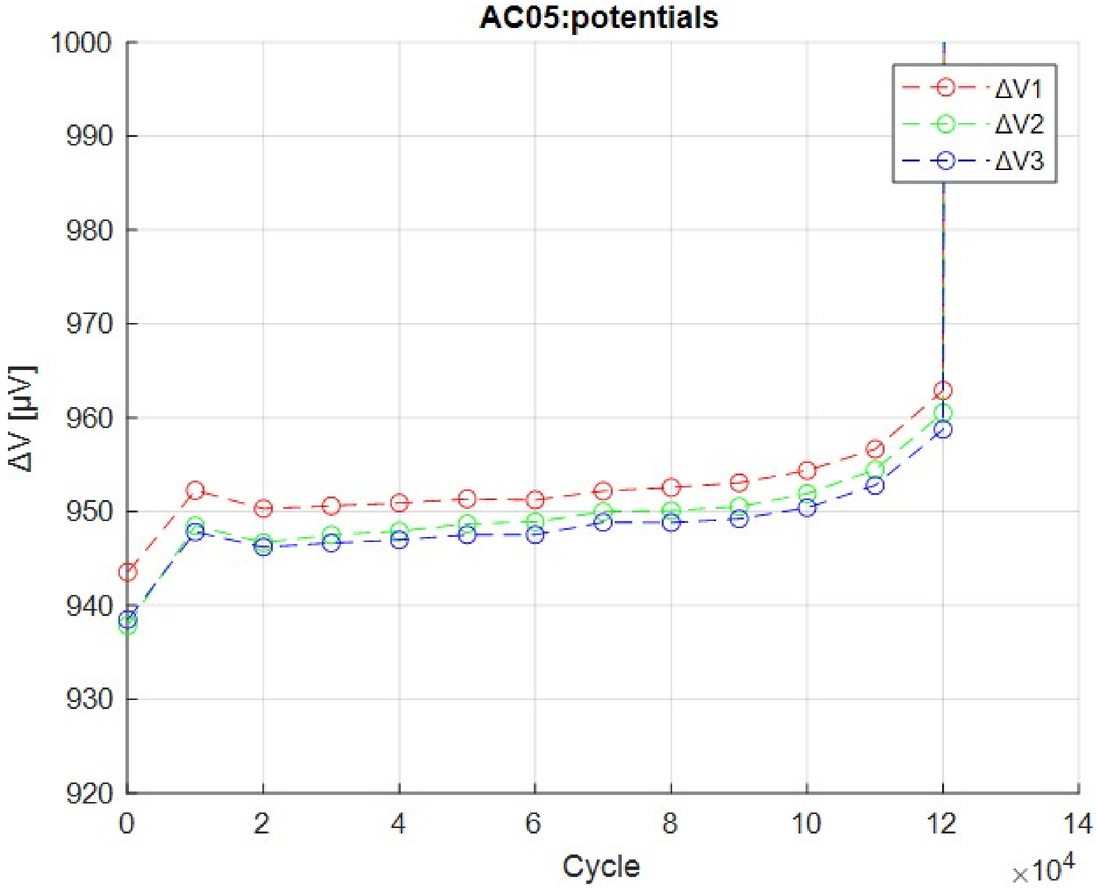

(b) Potential values

Figure A.7: AC05 specimen setup

A.2.4 AC06

Specimens

Code	AC06	**Type**	Single-edge crack round bar
Test	DCPD	**Material**	AISI 304
Date	3.04.23	**Operator**	Codemo

Geometry

$D_{\mathbf{nett}}$	8 mm	$D_{\mathbf{gross}}$	20 mm
$L_{\mathbf{nett}}$	10 mm	$L_{\mathbf{tot}}$	64 mm
$h_{\mathbf{notch}}$	0.3 mm	$a_{\mathbf{notch}}$	1.3 mm
$2Y_{\mathbf{p}}$	65 mm	$\frac{\boldsymbol{y_1}}{\boldsymbol{y_2}}$	1.28 -
N° probe	3	θ_s	120°
θ_f	0°	θ_n	60°

Load

Type	Force control	**R**	-1
ΔF_b	11 KN	$\boldsymbol{f}$	20 Hz
ΔF_o	19 KN	$\boldsymbol{f}$	0.5 Hz
$Cycle_b$	9999	$Cycle_o$	1

DCPD

Device	DOLI EDC580V	**Current**	1.6 A
Mode	Free running	**Type**	Local current input
ρ	71.4 e-8 Ωm		

Results

N° [#]	**a** [mm]	$\boldsymbol{\frac{c}{a}}$ [-]	θ [grad]	**Area** [mm^2]	**V1** [μV]	**V2** [μV]	**V3** [μV]
0	0.270	3.000	0.000	0.298	917.249	914.529	913.471
21	1.287	1.275	1.624	2.953	928.181	927.219	922.098
22	1.390	1.291	1.598	3.440	928.969	928.034	922.919
23	1.495	1.293	1.624	3.944	928.969	928.394	922.871
24	1.630	1.286	1.860	4.613	930.143	929.781	924.533
25	1.802	1.301	2.146	5.579	930.886	930.259	924.803
26	2.042	1.281	2.647	6.930	932.017	931.142	926.230
27	2.433	1.266	2.935	9.402	934.324	933.601	928.693
28	2.748	1.262	2.103	11.602	938.491	938.073	932.850

Photo

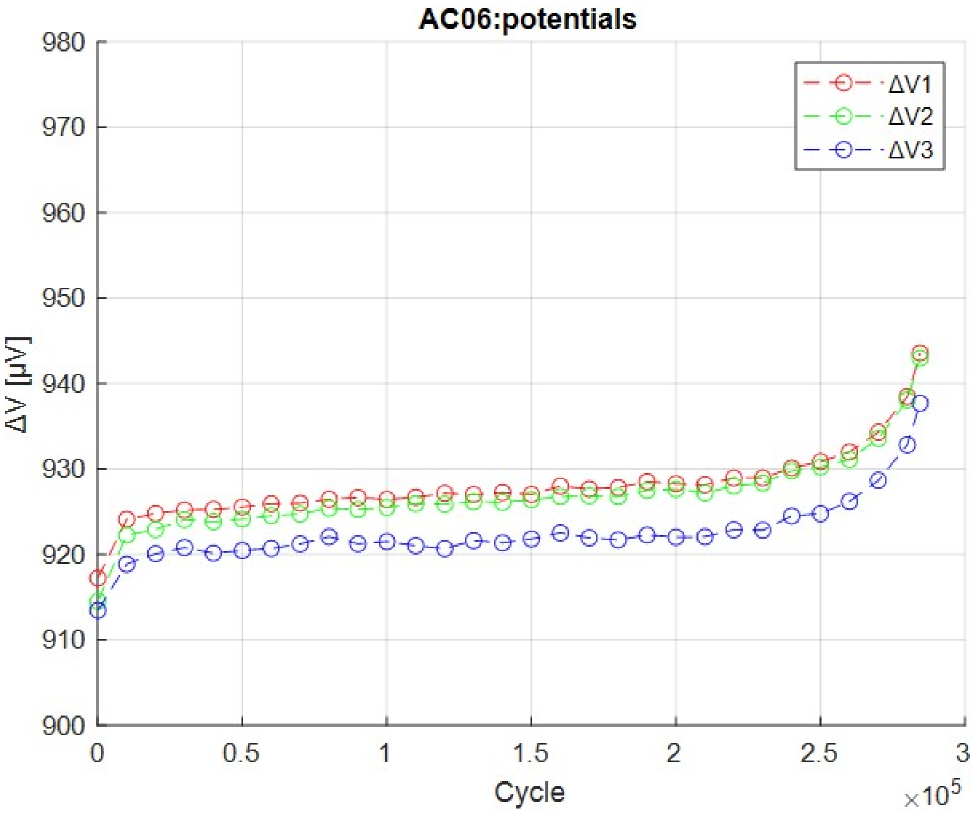

(a) potential values

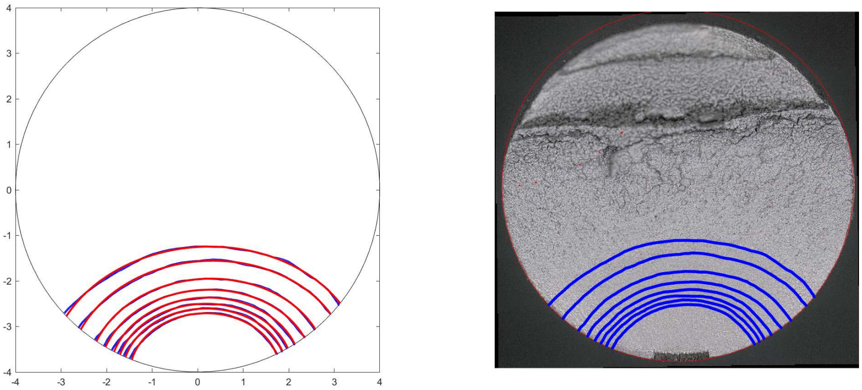

(b) fitted cracks

Figure A.8: AC06 specimen setup

A.2.5 AC07

Specimens

Code	AC07	**Type**	Single-edge crack round bar
Test	DCPD	**Material**	AISI 304
Date	16.04.23	**Operator**	Codemo

Geometry

$D_{\mathbf{nett}}$	8 mm	$D_{\mathbf{gross}}$	20 mm
$L_{\mathbf{nett}}$	10 mm	$L_{\mathbf{tot}}$	64 mm
$h_{\mathbf{notch}}$	0.3 mm	$a_{\mathbf{notch}}$	1.3 mm
$2Y_{\mathbf{p}}$	65 mm	$\frac{\boldsymbol{y_1}}{\boldsymbol{y_2}}$	1 -
N° probe	3	θ_s	120°
θ_f	0°	θ_n	30°

Load

Type	Force control	**R**	-1
ΔF_b	11.5 KN	$\boldsymbol{f}$	20 Hz
ΔF_o	19.5 KN	$\boldsymbol{f}$	0.5 Hz
$Cycle_b$	11999	$Cycle_o$	1

DCPD

Device	DOLI EDC580V	**Current**	1.6 A
Mode	Free running	**Type**	Local current input
ρ	71.4 e-8 Ωm		

Results

N°	**a**	$\frac{\boldsymbol{c}}{\boldsymbol{a}}$	θ	**Area**	**V1**	**V2**	**V3**
[#]	[mm]	[-]	[grad]	[mm^2]	[μV]	[μV]	[μV]
0	0.280	3.000	0.000	0.322	940.178	936.614	935.384
4	0.641	1.484	0.036	0.885	958.526	954.903	949.622
5	0.887	1.268	-0.063	1.448	980.598	976.780	972.367
6	1.006	1.366	-0.344	1.957	1072.030	1066.815	1061.952
7	1.378	1.265	-0.482	3.334	1371.626	1365.912	1361.807
8	2.203	1.247	-0.517	7.812	1438.844	1430.380	1427.021

Photo

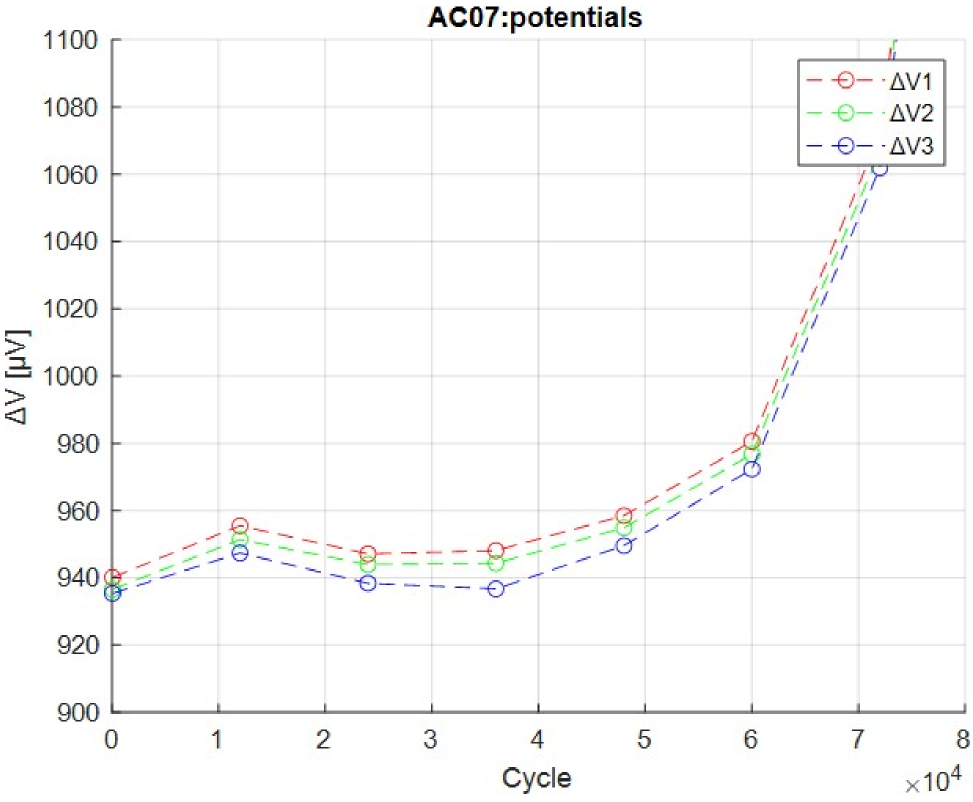

(a) Potential values

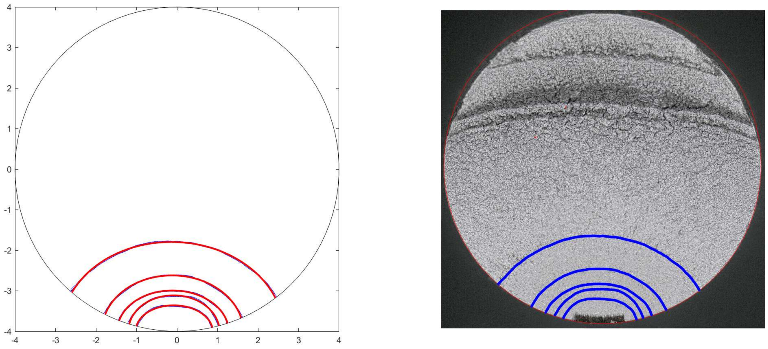

(b) fitted cracks

Figure A.9: AC07 specimen setup

A.3 Probe grips distance: 10 mm

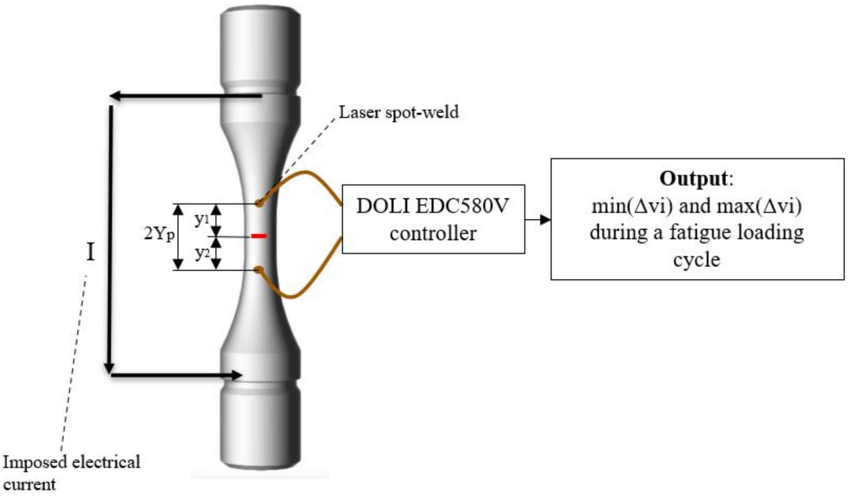

Figure A.10: specimen configuration y=5mm

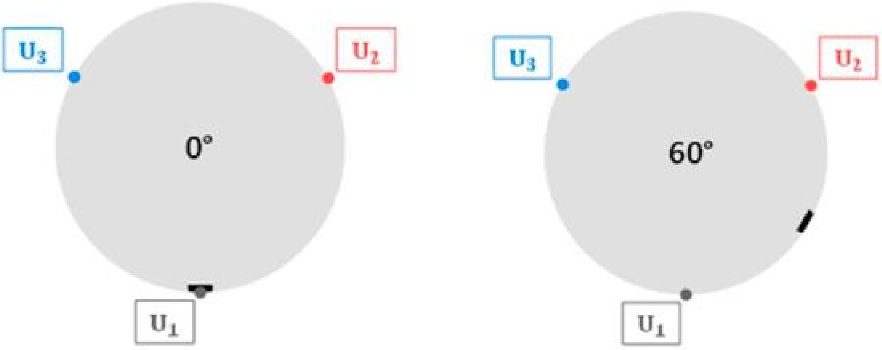

Figure A.11: secondary notch position

A.3.1 AC08

Specimens

Code	AC08	**Type**	Single-edge crack round bar
Test	DCPD	**Material**	AISI 304
Date	18.04.23	**Operator**	Codemo

Geometry

$D_{\textbf{nett}}$	8 mm	$D_{\textbf{gross}}$	20 mm
$L_{\textbf{nett}}$	10 mm	$L_{\textbf{tot}}$	64 mm
$h_{\textbf{notch}}$	0.3 mm	$a_{\textbf{notch}}$	1.3 mm
$2Y_{\mathbf{p}}$	10 mm	$\frac{y_1}{y_2}$	9 -
N° probe	3	θ_s	120°
θ_f	0°	θ_n	0°

Load

Type	Force control	**R**	-1
ΔF_b	11.5 KN	f	20 Hz
ΔF_o	19.5 KN	f	0.5 Hz
$Cycle_b$	11999	$Cycle_o$	1

DCPD

Device	DOLI EDC580V	**Current**	4 A
Mode	Free running	**Type**	Local current input
ρ	71.4 e-8 Ωm		

Results

N°	**a**	$\frac{c}{a}$	θ	**Area**	**V1**	**V2**	**V3**
[#]	[mm]	[-]	[grad]	[mm^2]	[μV]	[μV]	[μV]
0	0.266	3.000	+0.000	0.291	584.732	607.815	585.575
1	0.342	2.568	+0.132	0.416	598.205	623.435	598.298
2	0.425	2.045	+0.019	0.526	593.374	616.273	594.421
3	0.545	1.638	+0.033	0.704	596.070	616.628	593.963
4	0.680	1.462	-0.085	0.979	599.362	617.676	604.319
5	0.847	1.406	+0.189	1.443	603.649	618.670	596.154
6	1.049	1.351	-0.006	2.099	611.058	620.679	598.510
7	1.421	1.251	-0.178	3.504	624.597	624.523	598.815
8	2.181	1.234	-0.609	7.622	664.847	637.148	612.592

Photo

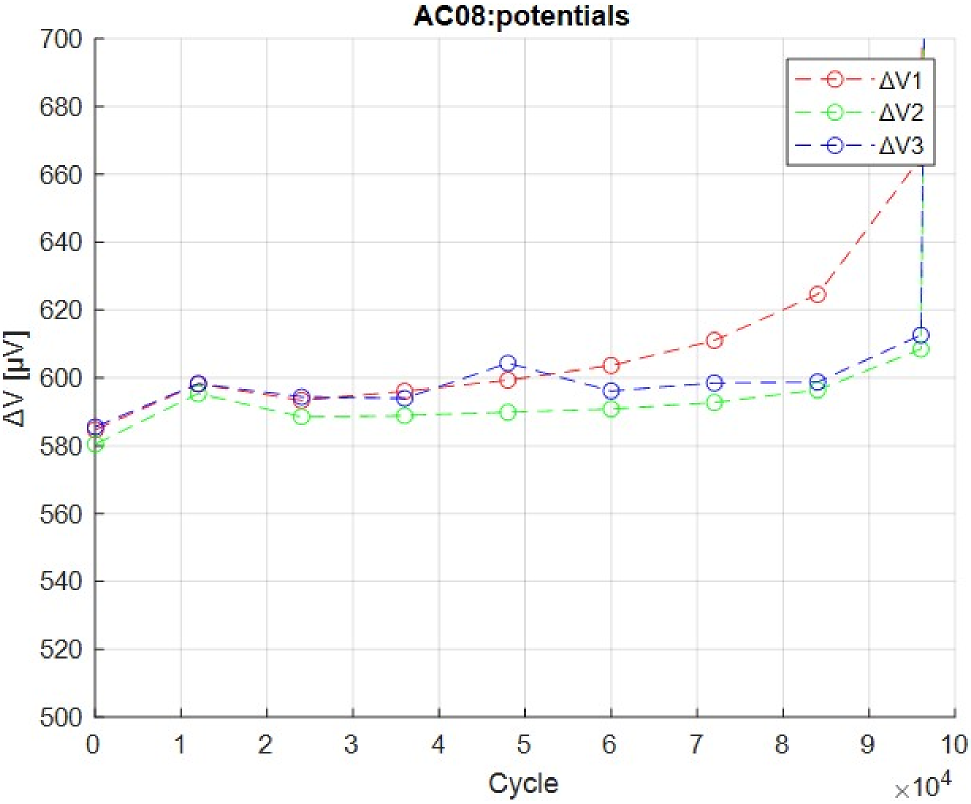

(a) potential values

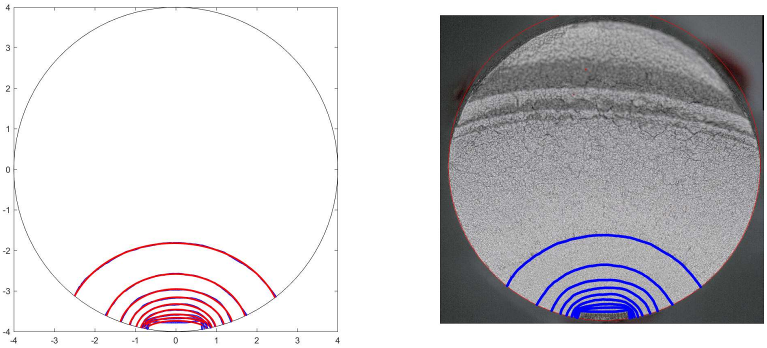

(b) fitted cracks

Figure A.12: AC08 specimen setup

A.3.2 AC09

Specimens

Code	AC09	**Type**	Single-edge crack round bar
Test	DCPD	**Material**	AISI 304
Date	22.04.23	**Operator**	Codemo

Geometry

$D_{\textbf{nett}}$	8 mm	$D_{\textbf{gross}}$	20 mm
$L_{\textbf{nett}}$	10 mm	$L_{\textbf{tot}}$	64 mm
$h_{\textbf{notch}}$	0.3 mm	$a_{\textbf{notch}}$	1.3 mm
$2Y_{\textbf{p}}$	10 mm	$\boldsymbol{\frac{y_1}{y_2}}$	1 -
N° probe	3	θ_s	120°
θ_f	0°	θ_n	60°

Load

Type	Force control	**R**	-1
ΔF_b	11.5 KN	$\boldsymbol{f}$	20 Hz
ΔF_o	19.5 KN	$\boldsymbol{f}$	0.5 Hz
$Cycle_b$	11999	$Cycle_o$	1

DCPD

Device	DOLI EDC580V	**Current**	4 A
Mode	Free running	**Type**	Local current input
ρ	71.4 e-8 Ωm		

Results

N°	**a**	$\boldsymbol{\frac{c}{a}}$	θ	**Area**	**V1**	**V2**	**V3**
[#]	[mm]	[-]	[grad]	[mm^2]	[μV]	[μV]	[μV]
0	0.385	2.679	0.000	0.535	632.018	599.763	585.158
1	0.528	1.706	0.565	0.685	649.350	670.853	617.150
2	0.682	1.458	0.671	0.983	685.643	699.475	766.838
3	0.850	1.358	0.644	1.415	664.642	710.912	720.615
4	1.071	1.294	0.629	2.109	650.573	633.610	722.239
5	1.404	1.260	0.691	3.446	673.623	647.381	695.186
6	2.004	1.289	0.652	6.726	670.405	651.974	705.682

Photo

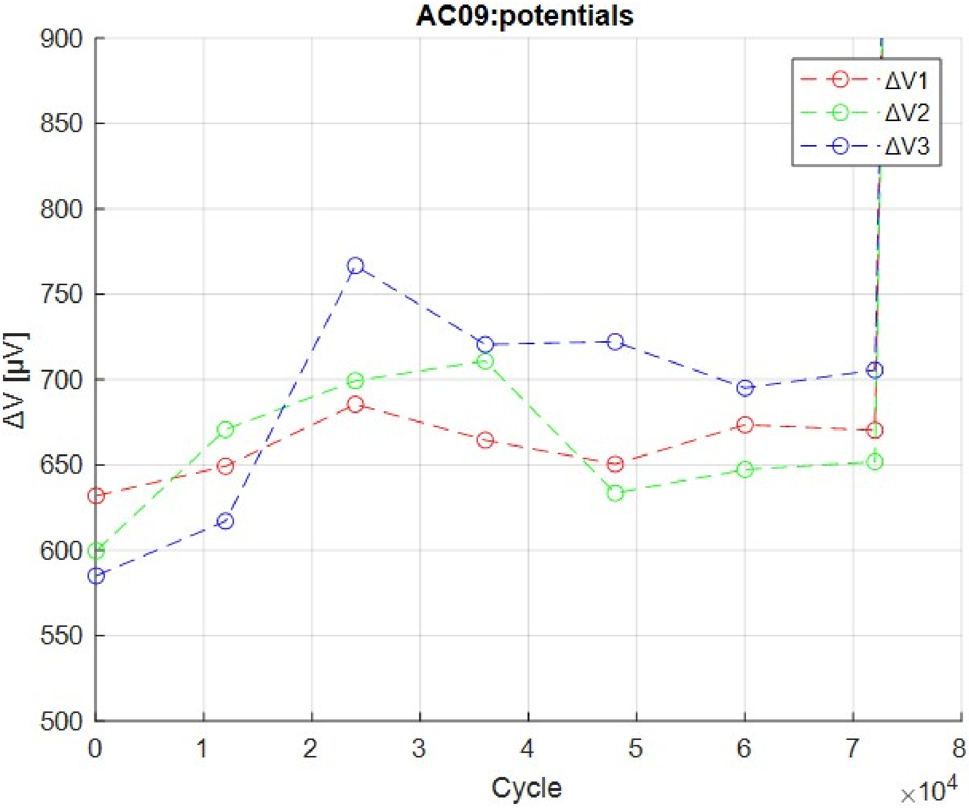

(a) potential values

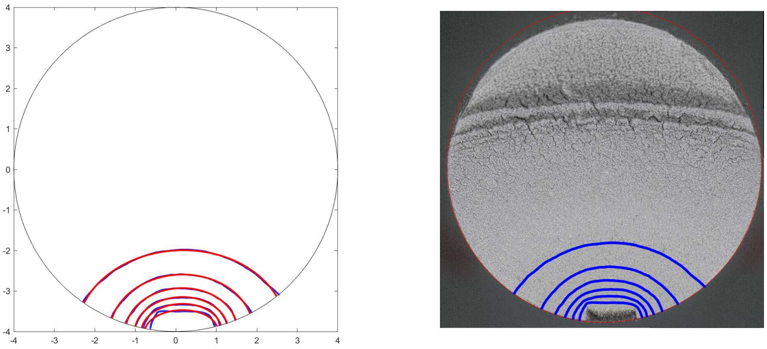

(b) fitted cracks

Figure A.13: AC09 specimen setup

A.3.3 AC10

Specimens

Code	AC10	**Type**	Single-edge crack round bar
Test	DCPD	**Material**	AISI 304
Date	10.05.23	**Operator**	Codemo

Geometry

$D_{\mathbf{nett}}$	8 mm	$D_{\mathbf{gross}}$	20 mm
$L_{\mathbf{nett}}$	10 mm	$L_{\mathbf{tot}}$	64 mm
$h_{\mathbf{notch}}$	0.3 mm	$a_{\mathbf{notch}}$	1.3 mm
$2Y_{\mathbf{p}}$	10 mm	$\frac{\boldsymbol{y_1}}{\boldsymbol{y_2}}$	1 -
N° probe	3	θ_s	120°
θ_f	0°	θ_n	60°

Load

Type	Force control	**R**	-1
ΔF_b	11.5 KN	$\boldsymbol{f}$	20 Hz
ΔF_o	19.5 KN	$\boldsymbol{f}$	0.5 Hz
$Cycle_b$	11999	$Cycle_o$	1

DCPD

Device	DOLI EDC580V	**Current**	4 A
Mode	Free running	**Type**	Local current input
ρ	71.4 e-8 Ωm		

Results

N° [#]	**a** [mm]	$\frac{\boldsymbol{c}}{\boldsymbol{a}}$ [-]	θ [grad]	**Area** [mm^2]	**V1** [μV]	**V2** [μV]	**V3** [μV]
0	0.318	3.000	0.000	0.408	610.465	634.758	607.636
10	1.059	1.307	-0.501	2.082	605.195	621.922	597.635
11	1.162	1.309	-0.555	2.484	607.146	618.147	597.788
12	1.293	1.309	-0.646	3.038	608.314	617.938	598.387
13	1.470	1.311	-0.837	3.860	619.847	610.344	600.670
14	1.723	1.297	-0.935	5.133	608.140	608.821	603.596
15	2.148	1.286	-1.374	7.605	619.552	618.814	609.835
16	3.341	1.391	-1.435	16.768	680.341	679.460	664.463

Photo

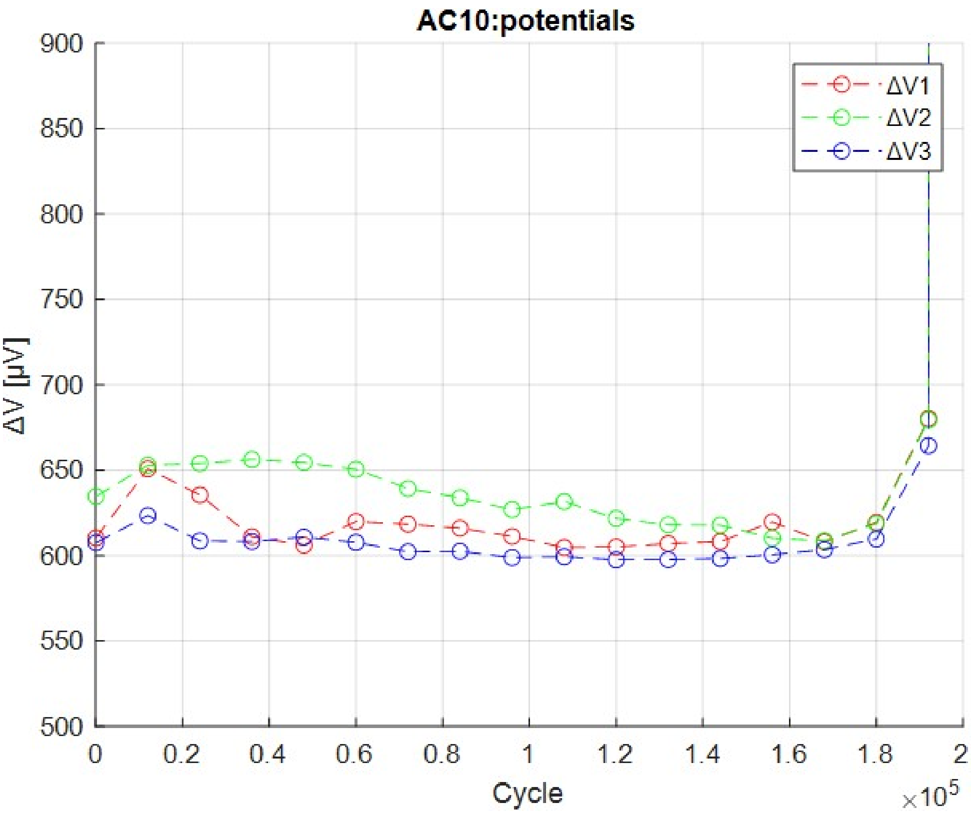

(a) Potential values

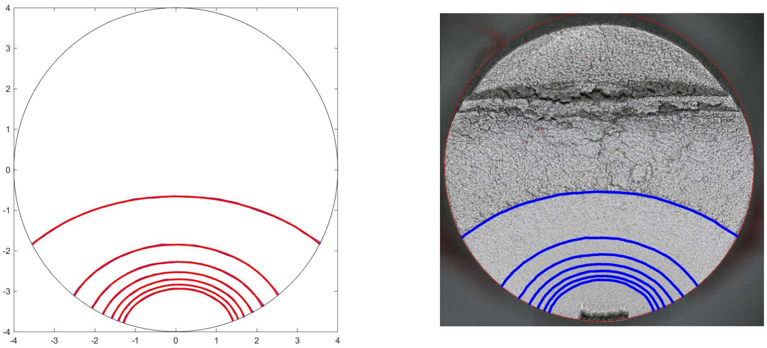

(b) fitted cracks

Figure A.14: AC10 specimen setup

A.4 Probe grips distance: 4 mm

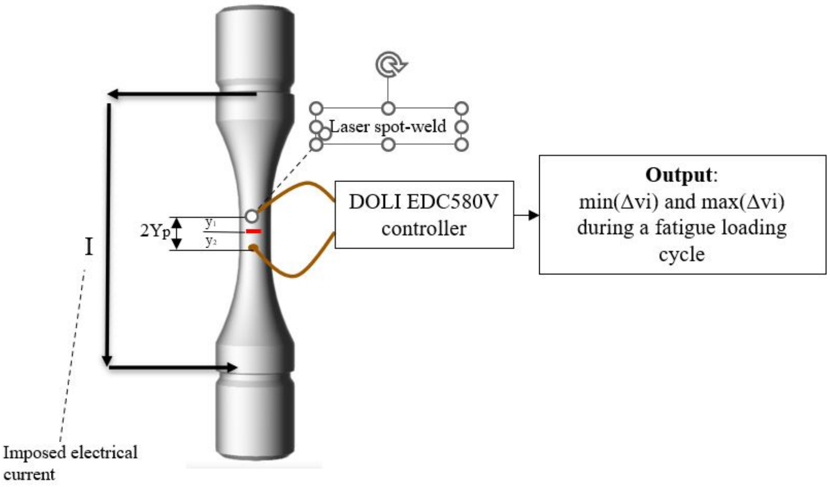

Figure A.15: AC10 specimen configuration

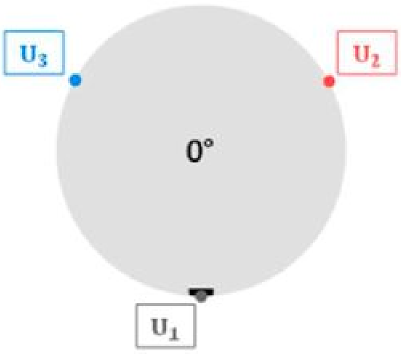

Figure A.16: secondary notch position

A.4.1 AC11

Specimens

Code	AC11	**Type**	Single-edge crack round bar
Test	DCPD	**Material**	AISI 304
Date	14.05.23	**Operator**	Codemo

Geometry

$D_{\mathbf{nett}}$	8 mm	$D_{\mathbf{gross}}$	20 mm
$L_{\mathbf{nett}}$	10 mm	$L_{\mathbf{tot}}$	64 mm
$h_{\mathbf{notch}}$	0.3 mm	$a_{\mathbf{notch}}$	1.3 mm
$2Y_{\mathbf{p}}$	4 mm	$\frac{\boldsymbol{y_1}}{\boldsymbol{y_2}}$	1 -
N° probe	3	θ_s	120°
θ_f	0°	θ_n	0°

Load

Type	Force control	**R**	-1
ΔF_b	12 KN	$\boldsymbol{f}$	20 Hz
ΔF_o	20 KN	$\boldsymbol{f}$	0.5 Hz
$Cycle_b$	11999	$Cycle_o$	1

DCPD

Device	DOLI EDC580V	**Current**	7.6 A
Mode	Free running	**Type**	Local current input
ρ	71.4 e-8 Ωm		

Results

N°	**a**	$\boldsymbol{\frac{c}{a}}$	θ	**Area**	**V1**	**V2**	**V3**
[#]	[mm]	[-]	[grad]	[mm^2]	[μV]	[μV]	[μV]
0	0.294	3.000	0.000	0.351	521.146	514.030	525.919
1	0.487	1.903	0.524	0.642	545.725	536.513	664.309
2	0.681	1.508	0.369	1.007	630.821	541.731	640.372
3	0.911	1.367	0.552	1.620	750.614	544.603	569.799
4	1.236	1.293	0.282	2.767	609.793	548.381	541.469
5	1.841	1.271	0.145	5.717	758.768	560.163	556.639

Photo

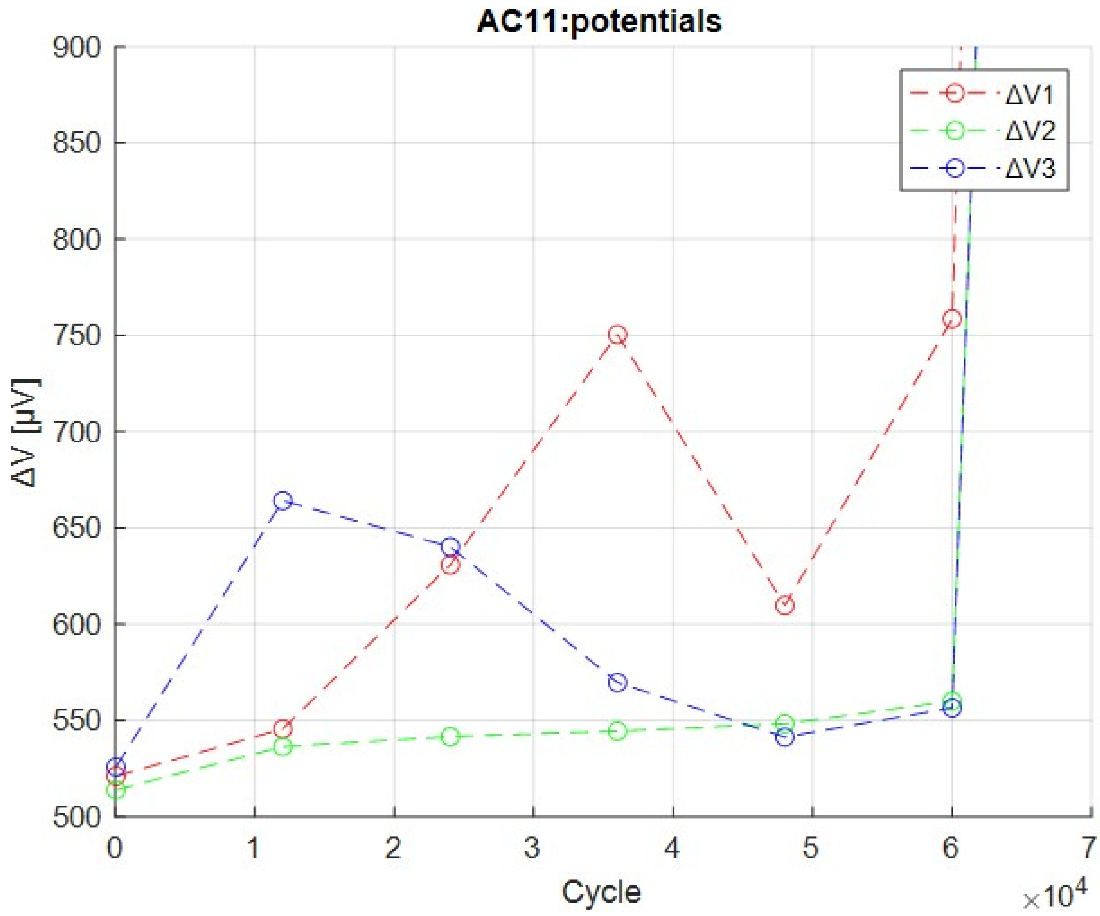

(a) pre-crack position

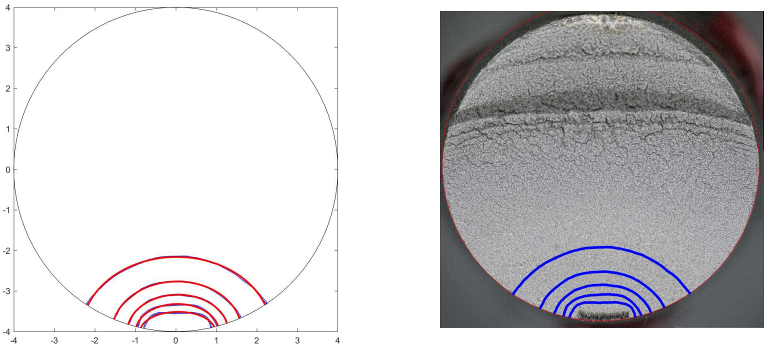

(b) fitted cracks

Figure A.17: AC11 specimen setup

A.4.2 AC12

Specimens

Code	AC12	**Type**	Single-edge crack round bar
Test	DCPD	**Material**	AISI 304
Date	16.05.23	**Operator**	Codemo

Geometry

$D_{\mathbf{nett}}$	8 mm	$D_{\mathbf{gross}}$	20 mm
$L_{\mathbf{nett}}$	10 mm	$L_{\mathbf{tot}}$	64 mm
$h_{\mathbf{notch}}$	0.3 mm	$a_{\mathbf{notch}}$	1.3 mm
$2Y_{\mathbf{p}}$	4 mm	$\frac{\boldsymbol{y_1}}{\boldsymbol{y_2}}$	1 -
N° probe	3	θ_s	120°
θ_f	0°	θ_n	0°

Load

Type	Force control	**R**	-1
ΔF_b	12 KN	$\boldsymbol{f}$	20 Hz
ΔF_o	20 KN	$\boldsymbol{f}$	0.5 Hz
$Cycle_b$	11999	$Cycle_o$	1

DCPD

Device	DOLI EDC580V	**Current**	7.6 A
Mode	Free running	**Type**	Local current input
ρ	71.4 e-8 Ωm		

Results

N°	**a**	$\boldsymbol{\frac{c}{a}}$	θ	**Area**	**V1**	**V2**	**V3**
[#]	[mm]	[-]	[grad]	[mm^2]	[μV]	[μV]	[μV]
0	0.256	3.000	0.000	0.271	476.293	483.719	472.153
11	0.961	1.257	0.042	1.678	495.710	488.297	480.777
12	1.082	1.251	0.076	2.094	499.899	488.878	482.056
13	1.206	1.277	0.048	2.613	507.256	489.848	483.411
14	1.424	1.276	-0.040	3.567	521.140	491.935	484.904
15	1.784	1.263	0.086	5.373	549.602	497.788	490.667
16	2.544	1.265	0.289	10.162	637.620	519.113	511.103

Photo

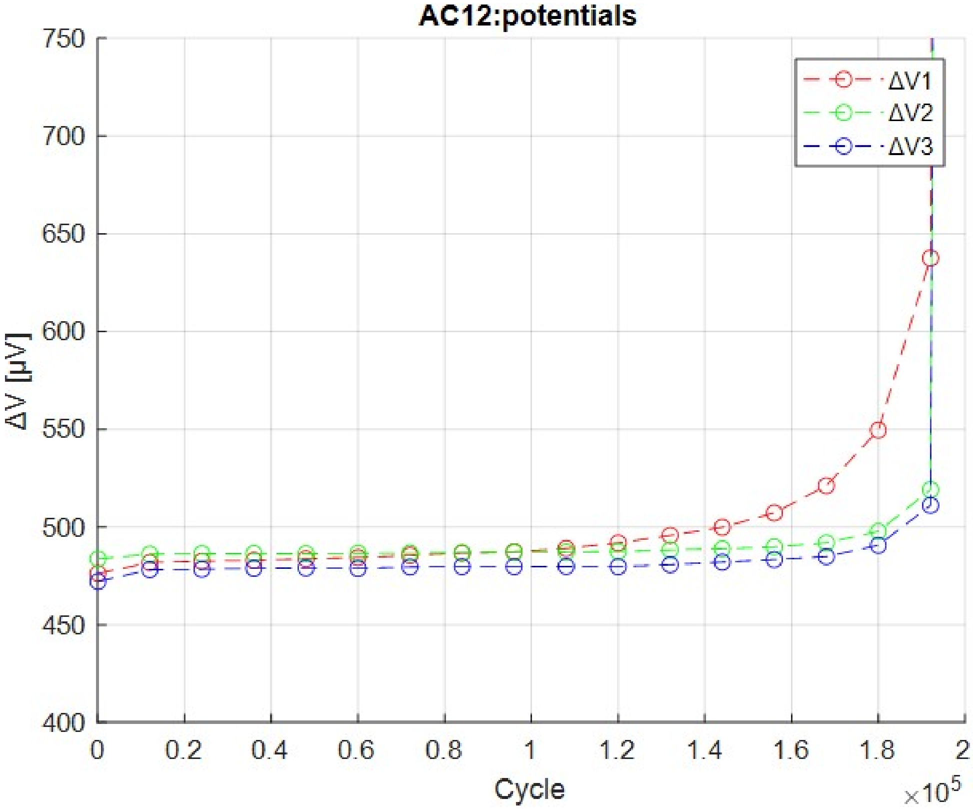

(a) potential values

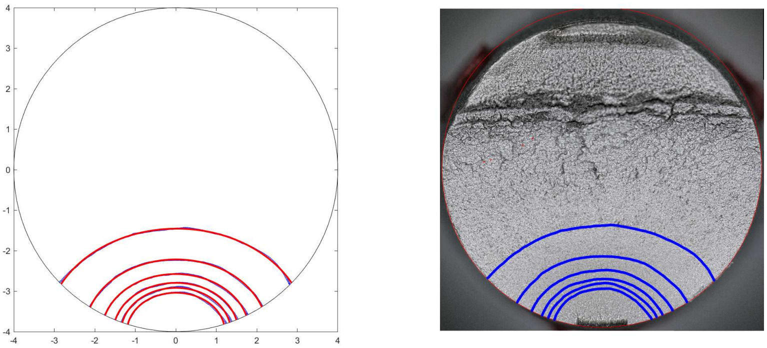

(b) fitted cracks

Figure A.18: AC12 specimen setup

Appendix B

ANSYS code

This APDL code used for electrical finite element analyses was originally devised by Ing. Luca Vecchiato and subsequently adapted for the analyses in this study.

```
/prep7
finish
/clear,all !Resets the ANSYS database to the conditions at the beginning of the problem
/undo,off
/triad,lbot
/config,nres,1000000 !Assign maximum number of results sets (substeps) allowed on the result file

seltol,1e-8
btol,1e-8

!----------------------------------------------------------------------
!PLOT_OPTIONS
!----------------------------------------------------------------------

       /pnum,kp,0
       /pnum,line,0
       /pnum,area,0
       /pnum,volu,0
```

```

!----------------------------------------------------------------------
!USER INPUT
!----------------------------------------------------------------------

!Constants Definition

       pi = 4*atan(1)

!File's Informations

       filename ='DCPD_rev01'


!Material's Properties

       T_amb = 20     !Temperature

       Resistivity_X5CrNi1810 = (71.4e-8)*(1000)  !X5CrNi1810  uguale ad AISI304
       Resistivity_AISI304L = (71.3e-8)*(1000)  ![(Ohm*m)*(mm/m)] I valori sono definiti costanti per la temperatura di riferimento indicata: Il FEM NON prevede di far variare la temperatura
       Resistivity_C45   = (20e-8)*(1000)  ![(Ohm*m)*(mm/m)] I valori sono definiti costanti per la temperatura di riferimento indicata: Il FEM NON prevede di far variare la temperatura

       Material_Name   = 'X5CrNi1810'
       Resistivity    = Resistivity_X5CrNi1810  !Choose one resistivity from "Resistivity Database"


```

```
!Geometry

        Dg   = 20
        Dn   = 8
        Lg   = 64.553
        Ln   = 10
        Ltot  = 80.4
        R1   = 65

!DCPD Surface mapping

        L_1   = 0.5  !Altezza Volume di controllo Intaglio
        dtheta  = 5   !Discretizzazione Tangenziale
        dL   = 0.5  !Discretizzazione Assiale

!Crack Geometry

        x0   = 0  !Do Not Change (x0=0)
        z0   = 0  !Do Not Change (z0=0)
        gamma  = 0  !Do Not Change (gamma=0)

        x_0 = Dn/2 + x0  !Definisco il centro dell'ellisse
        z_0 = 0 + z0

        a_min  = 0.2
        a_max  = 3.4
        da   = 0.2

        c_a_min  = 1.23
        c_a_max  = 3
        dc_a  = 0.5

```

```
!Mesh

       MESH_SIZE_1 = 0.05
       MESH_SIZE_2 = 0.1
       MESH_SIZE_3 = 0.8

!BC

       I   = 7.6      ![A] I/O Current

!Simulation’s Steps

       Debugging = 0    !Skip *Do cycles, Legend: 0=OFF, 1=ON
       Meshing  = 1    !Legend: 0=OFF, 1=ON
       BC   = 1    !Legend: 0=OFF, 1=ON
       Solving  = 1    !Legend: 0=OFF, 1=ON
       Post  = 1    !Legend: 0=OFF, 1=ON
       Print  = 1    !Legend: 0=OFF, 1=ON
       graphic_off = 1    !Legend: 0=OFF, 1=ON


*if,Print,eq,1,then

!---------------------------------------------------------------------
!DEFINE RESULT FILE
!---------------------------------------------------------------------

*cfopen,filename,’csv’,,append
*vwrite,’rho’,’I’,’a’,’a_D’,’c_a’,’NodeNumb’,’x’,’y’,’z’,’Theta’,’V’
(11(a8’,’))
*vwrite,’[Ohm*mm]’,’[A]’,’[mm]’,’[\]’,’[\]’,’[\]’,’[mm]’,’[mm]’,’[mm]’,’[deg]’,’[microV]’
```

```
(11(a8’,’))
*cfclos

*else
*endif

!----------------------------------------------------------------------
!Do cycle
!----------------------------------------------------------------------


*if,Debugging,eq,0,then

*do,c_a,c_a_min,c_a_max,dc_a
        *do,a,a_min,a_max,da


*else
        a = a_min
        c_a = c_a_min
*endif


        *if,graphic_off,eq,1,then

                /window,all,off

        *else
        *endif


        a_d = a/Dn
```

```

!---------------------------------------------------------------------
!ELEMENT TYPE
!---------------------------------------------------------------------

              /prep7

              et,1,plane230   !2D Quad
              et,2,solid231   !3D Brick
              et,3,solid232   !3D Tetra

              finish

!---------------------------------------------------------------------
!MATERIAL
!---------------------------------------------------------------------

              /prep7

              mptemp,1,T_amb
              mpdata,rsvx ,Material_Name ,1 ,Resistivity

              finish

!---------------------------------------------------------------------
!MODELLING
!---------------------------------------------------------------------

              /prep7


              k,1, 0,   0,   0
```

```
        k,2, Dn/2,  0,   0
        k,3, Dn/2,  Ln/2,  0
        k,4, Dg/2,  Lg/2,  0
        k,5, Dg/2,  Ltot/2,  0
        k,6, 0,   Ltot/2,  0
        k,1000, Dn/2+R1, Ln/2,  0

        l,1,2
        l,2,3
        larc,3,4,1000,R1
        l,4,5
        l,5,6
        l,6,1

        al,all

        vrotat,all,,,,,,6,1,180,1

        !__________Creo Volumi per mesh__________
        wpro,,-90.0
        wpave,,2*MESH_SIZE_1,
        rectng,-2*Dg,2*Dg,-2*Dg,2*Dg
        wpave,,L_1,
        rectng,-2*Dg,2*Dg,-2*Dg,2*Dg

        vsba,all,all
        wpcsys,-1,0
        csys,0

!__________Creo Mappatura per misura potenziale__________


```

```
    asel,s,loc,y,L_1,Lg/2
    asel,u,loc,z,0

    n_L = (Lg/2-L_1)/dL + 1 - 2   !Suddivisione Assiale

    wpro,,-90.0

    *do,index,1,n_L
            wpave,,L_1 + dL*index,
            rectng,-2*Dg,2*Dg,-2*Dg,2*Dg
    *enddo

    wpcsys,-1,0
    csys,0

    ainp,all

    n_theta = 180/dtheta + 1 - 2  !Suddivisione angolare

    *do,index,1,n_theta
            wprot,,,-dtheta
            rectng,Dn/2,Dg,L_1,Lg/2
    *enddo

    wpcsys,-1,0
    csys,0

    ainp,all

    asbl,all,all,,delete,delete
    allsel

```

```

            !__________Creo Cricca Ellittica__________

            k,4000, x_0, 0, z_0
            wprot,0,-90,0
            wprot,gamma,0,0
            kwpave,4000
            csys,4

            k,4001,-a,0,0
            k,4002,0,-a,0

            larc,4001,4002,4000,a

            ksel,s,,,4001,4002
            lslk,s,1
            lsscale,all,,,1,c_a,1,,1,1

            wpcsys,-1,0
            csys,0
            asel,s,loc,y,0
            lsel,s,loc,y,0

            asbl,all,all,,delete,delete

            allsel

!-----------------------------------------------------------------
!MESHING
!-----------------------------------------------------------------

            *if,Meshing,eq,1,then
```

```

                   /prep7

                   vsel,s,loc,y,0,2*MESH_SIZE_1
                   mshkey,0   !0=Free Meshing, 1=Mapped
                   type,3    !Assign Element Number
                   esize,MESH_SIZE_1
                   vmesh,all

                   vsel,s,loc,y,2*MESH_SIZE_1,L_1
                   mshkey,0   !0=Free Meshing, 1=Mapped
                   type,3    !Assign Element Number
                   esize,MESH_SIZE_2
                   vmesh,all

                   asel,s,loc,y,L_1,Lg/2
                   asel,u,loc,y,L_1
                   asel,u,loc,z,0
                   aesize,all,MESH_SIZE_2
                   allsel
                   vsel,s,loc,y,L_1,Ltot
                   esize,MESH_SIZE_3
                   mshkey,0   !0=Free Meshing, 1=Mapped
                   type,3    !Assign Element Number
                   vmesh,all

                   finish

            *else
            *endif

!----------------------------------------------------------------
```

```
!BC
!----------------------------------------------------------------

              *if,BC,eq,1,then

                     /prep7

                     !_______BC:immetria 1________******************

                     asel,s,loc,y,0
                     lsla,s
                     ksll,s
                     ksel,u,loc,x,Dn/2
                     lslk,s,1
                     lsel,r,loc,y,0
                     asll,s,1
                     asel,r,loc,y,0

                     da,all,volt,0   !0V on net section

                     allsel


                     !________Coupling_________********************

                     asel,s,loc,y,Ltot/2  !Current Remote I/O equipotential surface
                     nsla,s,1
                     cp,1,volt,all
                     allsel


```

```
                      !_________BC:LOAD________********************

                      fk,6,amps,I/2
                      allsel

                      finish

               *else
               *endif


!-----------------------------------------------------------------
!SOLVE
!-----------------------------------------------------------------

                      *if,Solving,eq,1,then

                      allsel
                      finish
                      /solve
                      eqslv,pcg
                      solve
                      finish

                      *else
                      *endif

!------------------------------------------------------------------
!POSTPROCESSING
!------------------------------------------------------------------

               *if,Post,eq,1,then
```

```

/post1

!Estraggo le misure di potenziale lungo la superficie cilindrica del volume 2

asel,s,loc,y,L_1,Lg/2
asel,u,loc,y,L_1
asel,u,loc,z,0
lsla,s
ksll,s
nslk,s     !Seleziono i nodi attaccati ai KPs selezionati


!Genero il vettore contenente i risulati dell’analisi Elettrica

*get,MeasureTotalNodes,node,,count
*dim, Electrical_RawData ,array ,MeasureTotalNodes ,6 ,1     !%%% ATTENZIONE 6 = (NodeNumb,X,Y,Z,theta,VOLT)

*do,index,1,MeasureTotalNodes

       *get,Electrical_RawData(index,1) ,node ,0 ,num ,min
       *get,Electrical_RawData(index,2) ,node ,Electrical_RawData(index,1) ,LOC ,x
       *get,Electrical_RawData(index,3) ,node ,Electrical_RawData(index,1) ,LOC ,y
```

```
                            *get,Electrical_RawData(index,4) ,node , Electrical_RawData(index,1) ,LOC ,z

                            Electrical_RawData(index,5) = atan2( Electrical_RawData(index,2), Electrical_RawData(index,4))     !Theta = atan2(x,z) [rad]
                            Electrical_RawData(index,5) = Electrical_RawData(index,5)*180/pi     ![rad] to [deg]
                            Electrical_RawData(index,5) = 90 - Electrical_RawData(index,5)         !From range [-90; +90] to range [0; +180]

                            *get,Electrical_RawData(index,6) ,node , Electrical_RawData(index,1) ,volt
                            Electrical_RawData(index,6) = Electrical_RawData(index,6)*(10**6)     ![V] to [microV]

                            nsel,u,,,Electrical_RawData(index,1)

                     *enddo

!---------------------------------------------------------------
!WRITE RESULTS
!---------------------------------------------------------------

*if,Print,eq,1,then

*cfopen,filename,'csv',,append
```

```
*vwrite,Resistivity,I,a,a_d,c_a,Electrical_RaWData(1,1),
   Electrical_RaWData(1,2),Electrical_RaWData(1,3),Electrical_RaWData
   (1,4),Electrical_RaWData(1,5),Electrical_RaWData(1,6)
(11(e15.5’,’))
*cfclos

*else
*endif

!----------------------------------------------------------------
!DELETE MODEL
!----------------------------------------------------------------


                      *if,a_min,eq,a_max,and,c_a_min,eq,c_a_max,then

                             !In this case, no *Do cycles are running =
                                Debugging

                      *else

                             /prep7

                             allsel

                             *del,Electrical_RawData   !Delete Array
                                Parameters that change size to Avoid
                                Errors
                             *del,Electrical_OldOrder  !Delete Array
                                Parameters that change size to Avoid
                                Errors
```

```
parsav,all,parameters,parm  !Save Parameters to keep safe *do cycles indicies

lsclear,all      !Clears loads and load step options

cpdele,all      !Deletes coupled degree of freedom sets

csdele,all      !Deletes local coordinate systems

vclear,all      !Deletes nodes and volume elements associated with selected volumes
aclear,all      !Deletes nodes and area elements associated with selected areas
lclear,all      !Deletes nodes and line elements associated with selected lines
kclear,all      !Deletes nodes and point elements associated with selected KPs

vdele,all      !Deletes unmeshed volumes
adele,all      !Deletes unmeshed areas
ldele,all      !Deletes unmeshed lines
kdele,all      !Deletes unmeshed KPs

finish

/clear

parres,new,parameters,parm

```

```
                                /prep7

                        *endif

                        *else
                        *endif

*if,Debugging,eq,0,then

                *enddo

        *enddo
*else
*endif

finish
allsel

*if,graphic_off,eq,1,then

        /window,all,on

*else
*endif
```

Bibliography

[1] Tec-science. `https://www.tec-science.com/material-science/material-testing/dye-liquid-penetrant-inspection-dpi/`.

[2] Tec-science. `https://www.tec-science.com/material-science/material-testing/magnetic-particle-inspection-mpi/`.

[3] Wermac. `https://www.wermac.org/others/ndt_eddy_current.html`.

[4] Wikipedia-ultrasonic testing. `https://en.wikipedia.org/wiki/Ultrasonic_testing`.

[5] www.puntonetto.it, visual testing. `https://www.puntonetto.it/visual-test.html`.

[6] Uni - ente italiano di normazione, 2014.

[7] Trost A. Ermittlung von rissen and messung der risstiefen in metallischen werkstoffen durch elektrische spannungsmessung. *Metallwirtschaft*, 1944.

[8] F. Berto K. Tanaka A. Campagnolo, G. Meneghetti. Calibration of the potential drop method by means of electric fe analyses and experimental validation for a range of crack shapes. *Fatigue Fract Eng Mater Struct.*, 2018.

[9] The International Atomic Energy Agency. *Guidebook for the Fabrication of Non-Destructive Testing (NDT) Test Specimens.* IAEA, 2001.

[10] Giovanni Meneghetti Alberto Campagnolo, Jürgen Bär. Analysis of crack geometry and location in notched bars by means of a threeprobe potential drop technique. *International Journal of Fatigue*, 2019.

[11] Ritchie R. Aronson G. Optimization of the electrical potential technique for crack growth monitoring in compact test pieces using finite element analysis. *J Test Eval.*, 1979.

[12] Jürgen Bär. Crack detection and crack length measurement with the dc potential drop method–possibilities, challenges and new developments. *applied science*, 2020.

[13] Ivo Cerny. Measurement of subcritical growth of defects in large components of nuclear power plants at elevated temperatures. *International Journal of Pressure Vessels and Piping*, 2001.

[14] Knott JF. Clark G. Measurement of fatigue cracks in notched specimens by means of theoretical electrical potential calibrations. *J Mech Phys Solids.*, 1975.

[15] Tiedemann D. Zweidimensionale ausbreitung kurzer risse unter berücksichtigung bruchmechanischer und kontinuumsmechanischer aspekte – ein beitrag zur optimierung von lebensdauervorhersagen an gekerbten struktuen, 2016.

[16] Claus-Peter Fritzen Daniel Balageas and Alfredo G*üemes. Structural Health Monitoring.* ISTE Ltd, 2006.

[17] Henaff G Mary C Pierret S. Doremus L, Nadot Y. Calibration of the potential drop method for monitoring small crack growth from surface anomalies—crack front marking technique and finite element simulations. *Int J Fatigue.*, 2015.

[18] A. Campagnolo P. Rech M. Cova G. Meneghettia, L. Vecchiato. Numerical calibration of the direct current potential drop (dcpd) method in fracture mechanics fatigue tests. *Procedia Structural Integrity*, 2020.

[19] Johnson H.H. Calibrating the electrical potential method for studying slow crack growth. *Materials Research and Standards 5, No. 9, 442-445.*, 1965.

[20] Dominic Tiedemann Jürgen Bär. Experimental investigation of short crack growth at notches in 7475-t761. *Procedia Structural Integrity*, 2017.

[21] Jürgen Bär Meike Funk. Influence of crack initiation on short crack propagation and cyclic lifetime of aa 7475-t761. *Procedia Structural Integrity*, 2018.

[22] J*ü*rgen B*ä*r Mike Nahbein. Determination of cracks using multiple dc potential drop measurements – experimental verification of an advanced model. *Procedia Structural Integrity*, 2022.

[23] J*ü*rgen B*ä*r Moritz Hartweg. Analysis of the crack location in notched steel bars with a multiple dc potential drop measurement. *Procedia Structural Integrity*, 2019.

[24] Abdulmuttalib Abdulkareem Muhsen. Non-destructive testing methods and their application in technology. *ResearchGate*, 2021.

[25] Lord W Nath S, Rudolphi T. Three dimensional modeling of the dc potential drop method using finite element and boundary element analysis. *Springer*, 1992.

[26] Knott JP. Ritchie RO, Garrett GG. Crack-growth monitoring: optimisation of the electrical potential technique using an analogue method. *Int J Fract Mech.*, 1971.

[27] A. Shibli. *Power Plant Life Management and Performance Improvement.* Woodhead Publishing Series in Energy, 2011.

[28] Thornton W. Thornton B. The measurement of the thickness of metal walls from one surface only, by an electrical method. *Proc Instit Mech Eng*, 1938.

[29] Wilson WK. On the electrical potential analysis of a cracked fracture mechanics test specimen using the finite element method. *Eng Fract Mech.*, 1983.

[30] C.J. Hyde Y. Si, J.P. Rouse. Potential difference methods for measuring crack growth: A review. *International Journal of Fatigue*, 2020.